Investigation of Thermal and Flow Fields above and below the Air-Water Interface during Natural Convection

Syed Junaid Kamran Bukhari

A Thesis

in

The Department

of

Mechanical and Industrial Engineering

Presented in Partial Fulfillment of the Requirements
for the Degree of Doctor of Philosophy at
Concordia University
Montreal, Quebec, Canada

August 2007

Your file Votre référence
ISBN: 978-0-494-31148-6
Our file Notre référence
ISBN: 978-0-494-31148-6

ABSTRACT

Investigation of Thermal and Flow Fields above and below the Air-Water Interface during Natural Convection

Syed Junaid Kamran Bukhari, Ph. D.

Concordia University, 2007

Present dissertation describes the turbulent convection in horizontal layers of air and water separated by an evaporative shear-free water surface during natural convection. A detailed analysis of the hydrodynamic turbulent structure on water and air sides is presented in this study. The major portion of the research comprised of experimental investigation in addition to simulation of simultaneous airside and waterside velocity fields. The experimental measurements were made using non-intrusive state-of-the-art techniques, namely particle image velocimetry (PIV) and laser induced fluorescence (LIF) for instantaneous measurements of velocity and temperature fields, respectively.

The numerical study shows organized bulk vortical motions on air and water sides. The results also show that for unstable thermal stratification the magnitude of the airside velocities is an order of magnitude higher than the waterside velocities. The experimental results show that the water and air flow fields undergo three-dimensional flow interactions which form complex flow patterns. A detailed spectral analysis has been performed to investigate the temporal and spatial scales of turbulent motions

induced during natural convection. The wavenumber and frequency spectra showed the existence of two distinct power law regimes. In low wavenumber (100 rad/m < k < 800 rad/m) and low frequency (0.06 Hz < f < 0.8 Hz) ranges, the spectra exhibit -3 slopes providing the first evidence of the existence of the buoyancy subrange in the waterside flow field during natural convection, where the energy loss is due to the work against buoyancy. At higher wavenumbers and frequencies, the inertial subrange with the classical slope of -5/3 is observed. The results also show that the scaling parameters proposed for wall-bounded natural convection are also suitable for natural convection across evaporative air-water interface.

The average temperature profiles show a characteristic boundary layer distribution in the near surface region with an extensive core of constant temperature in the bulk. The temperature profiles within the conduction layer are found to be in good agreement with previous theoretical and experimental results. The present results show z^{-1} dependency in the thermal source layer and $z^{-1/3}$ dependency in the bulk region away from the interface which are in good agreement with the past theoretical analysis.

This work is dedicated with all my heart to my

beloved parents whose continuous support

made this achievement possible

ACKNOWLEDGMENTS

I would like to extend my sincere gratitude to my advisor Dr. Kamran Siddiqui for his suggestions, ideas and valuable guidance over the past four years. His trust and confidence allowed me to accomplish my goals. He has helped me to improve my research skills and taught me to apply my energies to achieve my ultimate objective of earning the doctoral degree. He has taught me invaluable lessons, which will serve as a guiding light for the rest of my career.

I am very grateful to the members of my research group, Shivani Tara Gajusingh, Nasiruddin Shaikh, Majid Nabavi and Hadi Babaei for the good times and their help in discovering new ways of thinking. The technical assistance provided by the Department's technical staff specially Gilles Huard, Brad Luckhart, Joseph Hulet and William Wong is also appreciated.

My eternal thanks and gratitude to my parents for continuous support and encouragement throughout my educational career. Without their support I would not able to complete my studies. I am thankful to my brothers and sisters for their constant care and prayers. I would also like to thank my elder brother Mazhar Bukhari for continuous support to fulfill my task. Last but not least, I would like to express my deepest gratitude to my wife for her limitless patience, understanding and encouragement during the period of thesis preparation.

THESIS FORMAT

This dissertation is a "Manuscript-Based" dissertation that is in accordance with the specifications, defined by the School of Graduate Studies at Concordia University. Each chapter is presented as a technical paper. The contents of the papers presented in chapters 2 to 6 are published or submitted for publications in refereed journals.

Chapter 2

Bukhari, S. J. K. and Siddiqui, M. H. K. (2007) **Characteristics of Air and Water Velocity Fields during Natural Convection.** *Heat Mass Transfer,* **43**, 5, 415-425.

Chapter 3

Bukhari, S. J. K. and Siddiqui, M. H. K. (2006) **Turbulent Structure beneath Air-Water Interface during Natural Convection.** *Phys. Fluids,* **18**, 035106.

Chapter 4

Bukhari, S. J. K. and Siddiqui, M. H. K. (2007) **The Impact of Air Saturation on the Flow Structure beneath Air-Water Interface during Natural Convection.** *International Journal of Heat and Mass Transfer* (in press).

Chapter 5

Bukhari, S. J. K. and Siddiqui, M. H. K. (2007) **An Experimental Study of the Thermal Field underneath an evaporative water surface using Laser Induced Fluorescence (LIF)** (submitted to *International Journal of Heat and Mass Transfer*).

Chapter 6

Bukhari, S. J. K. and Siddiqui, M. H. K. (2007) **An Experimental Study of the Airside Flow Structure during Natural Convection** (submitted to *Journal of Fluid Mechanics).*

TABLE OF CONTENTS

Page

LIST OF FIGURES

LIST OF TABLES

NOMENCLATURE

g	Gravitational acceleration	(cm/s^2)
L	Water depth	(m)
T_s	Water surface temperature	(^oC)
T_b, T_∞	Water bulk temperature	(^oC)
u_{rms}	Root-Mean-Square (RMS) horizontal turbulent velocity	(cm/s)
w_{rms}	Root-Mean-Square (RMS) vertical turbulent velocity	(cm/s)
u	Horizontal velocity	(cm/s)
v	Vertical velocity	(cm/s)
z	Vertical distance	(cm)
$z*$	Water depth	(cm)
l	Length of the tank	(cm)
b	Breadth of the tank	(cm)
d	Depth of the tank	(cm)
C_∞	Bulk concentration of the fluid	(kg/m^3)
C_w	Concentration at water surface	(kg/m^3)
C_a	Concentration in air	(kg/m^3)
J	Evaporation rate	($kg/hr\text{-}m^2$)
h_{fg}	latent heat of vaporization	(kJ/kg)
q''_L	latent heat	(W/m^2)
q''_{total}	Total heat flux	(W/m^2)
q''_s	Surface heat flux	(W/m^2)
$q''_{sensible}$	Sensible heat flux	(W/m^2)
q''_{wall}	Wall heat flux	(W/m^2)
w_*	Velocity scale in the outer layer	(cm/s)
w_o	Velocity scale in the conduction layer	(cm/s)
$\theta*$	Temperature scale in the outer layer	(^oC)
θ_o	Temperature scale in the conduction layer	(^oC)

Q_o	Kinematic heat flux	(°C mm/s)
c_p	Specific heat of water	(J/kg-K)
k	Wavenumber	(rad/m)
f	Frequency	(Hz)
Φ_u	Energy of wavenumber spectrum of horizontal velocity	
Φw	Energy of wavenumber spectrum of vertical velocity	
G_u	Energy of frequency spectrum of horizontal velocity	
G_w	Energy of frequency spectrum of vertical velocity	
I	Fluorescence energy emitted per unit volume	(W/m^3)
I_o	incident light flux	(W/m^2)
C	Concentration of the dye solution	(kg/m^3)
Pr	Prandtl number $= \frac{\nu}{\alpha}$	dimensionless
Re_*	Reynolds number $= \frac{w_* z_*}{\nu}$	dimensionless
Ra	Rayleigh number $= \frac{g\beta\Delta T L^3}{\nu\alpha}$	dimensionless
Ra^*	Flux-based Rayleigh number $= \frac{g\beta q_s L^4}{\nu\alpha k}$	dimensionless

Greek Symbols

β	Thermal expansion coefficient	(1 / K)
β_C	Concentration expansion coefficient	(1 / K)
ε	The rate of turbulent kinetic energy dissipation	(cm^2/s^3)
ν	Kinematic viscosity of water	(cm^2/s)
α	Thermal diffusivity	(cm^2/s)
ρ_∞	Density of the bulk of the fluid	(kg/m^3)
ρ_a	Density of air	(kg/m^3)
ρ_w	Density of water	(kg/m^3)
μ_a	Dynamic viscosity of air	(kg/m-s)
μ_w	Dynamic viscosity of water	(kg/m-s)

k_a	Thermal conductivity of air	(W/m-K)
k_w	Thermal conductivity of water	(W/m-K)
ω'	Turbulent vorticity	(s^{-1})
δ	Conduction layer thickness	(cm)
ρ	Density	(kg/m^3)
ε	Absorption coefficient	(m^2/kg)
ϕ	Quantum efficiency	
$\eta(\vec{x},t)$	Volume fraction of water	

Chapter 1

Introduction

1.1 Natural Convection Process

Natural convection is induced in fluid by the action of body forces (gravity) due to density variations caused by the temperature difference. This phenomenon, in a horizontal fluid layers occurs in wall bounded flows i.e. the fluid confined between upper and lower solid boundaries or in fluids with shear-free upper surface. The factors that differentiate the natural convection process in wall bounded and free surface fluids are the thermal and hydrodynamic boundary conditions. In wall bounded flows, the thermal boundary conditions for the upper and lower plates are of either the constant temperature or constant heat flux. And the heat transfer across the boundaries is purely sensible heat transfer. The hydrodynamic boundary condition is of no-slip type at both boundaries. However, in free surface flows, the air-water interface is considered to be shear-free or stress-free slip boundary (Flack *et al.* 2001). The heat transfer across the air-water interface is in the forms of sensible and latent, where the latter is due to the evaporation at the water surface which is not present in wall bounded flows. Due to the difference in the boundary conditions, the natural convection process particularly near the boundary is different in both cases. In wall-bounded case, heat is typically supplied to the fluid through the lower surface and cooled from above. When heat is supplied, the fluid layer adjacent to the lower surface gets warmer and consequently less dense than the fluid above this layer. Thus, the lighter fluid begins to rise which is replaced by the heavier fluid from the top, inducing the convective motions within the fluid domain (Benard

1900, 1901). The heat source provides the energy which serves to maintain the motion, while the motion serves as a mechanism for the transport of heat. From an evaporating surface, the natural convection process is significantly influenced by the evaporation at the water surface which results in the development of a cool water layer at the interface. This cooler and denser water layer becomes unstable and falls through the warmer less dense water underneath. Warmer water then rise to replace the falling cold water to satisfy mass conservation. This evaporatively-driven natural convection is turbulent and the resulting temperature and velocity fields are complex. Fig. 1.1 shows the mixing model presented by Katsaros *et al.* (1977) about the boundary layer removal during natural convection from an evaporative water surface. They indicated three regions and the name of these regions were suggestive of the characteristics of the motions in each layer. The first region immediately underneath the water surface is a thin layer where the conductive heat flux is the dominating mode of heat transfer. This layer is called the molecular conduction layer. Below this thin surface layer second region exists which is called the thermal source layer. This layer acts as a source for the cold water to produce the plunging sheets. In the region beneath the thermal source layer, the downward vertical advection of cold water equals the upward advection of warm water and the flow is well mixed. This third region is called the turbulent convective region in which vertical convective currents are dominating and, heat and momentum is transferred predominately by the eddy motion.

Evaporative cooling of the water surface results in the temperature change which in turn alters the thermal transport across the interface. Evaporation from a water surface is governed by three processes, transfer of liquid molecules across the surface into the

vapor phase, removal of newly formed vapor from the interface and supply of heat to the surface (Bejan, 2004, 1993). The rate of each of these processes is determined by a driving force and can be expressed in terms of a process resistance. Evaporation rate generally depends on the sum of these resistances. In particular situations, any one of them may be dominating. Evaporation from a water surface is a function of the vertical moisture gradient and the nature of air movement into which evaporation occurs. The vertical moisture gradient is the difference in water-vapor concentration at the water surface and the moisture content in air at greater height. Transformation of water vapors requires energy that is known as the latent heat of vaporization. Water molecules at the surface acquire this energy from water and overcome the intermolecular forces which results in the transfer of water molecules to the surrounding air as vapors.

The mass concentration of water vapor in near-surface air is generally different from its concentration in the bulk free stream. The air that comes in contact with the water surface becomes saturated with water vapor i.e. its relative humidity becomes 100 percent and the vapor pressure of moisture in this air mixture become equal to the saturation pressure. This humid air mixture then rises above and is being replaced by relatively dry air from above. As this mass of dry air approaches the water surface, it acquires moisture from the water surface becomes humid and ascends. The airside vortices transfer the warm and moist air away from the interface and bring the cold and less humid air from the bulk to the surface. Bejan (2004) argued that if the air column above the water surface is wide enough, the humid air rises by natural convection through the center of the column and the dry air descends along the walls. This maintains the vapor concentration gradients in the near-surface and bulk regions. The concentration

difference has the ability to drive more water vapor out of the water layer. Fig. 1.2 (a) shows a coupled air-water system in a tank enclosed by walls and open from the top to allow evaporation into stationary air. The typical vapor concentration profile in air is plotted in Fig. 1.2 (b), where $C_{w,\infty}$ is the water vapors concentration in the ambient air and $C_{w,o}$ is the vapors concentration at the air-water interface. Evaporation from the water surface is driven by the vapor concentration gradient across the water surface and the bulk air.

1.2 Strength of Convective Currents

The strength of convective currents and flow patterns observed during natural convection depends on the buoyancy and viscous forces. The non-dimensional parameter which is a measure of the relative strength of these effects is the Rayleigh number defined as,

$$Ra = \frac{g\beta(T_b - T_s)L^3}{\nu\alpha} \tag{1.1}$$

where, β is the coefficient of thermal expansion, g is the gravitational acceleration, α is the thermal diffusivity, v is the kinematic viscosity, L is the water depth, T_b is the bulk water temperature and T_s is the water surface temperature (Incropera 2006). When the Rayleigh number is sufficiently small, viscous forces are dominant than the buoyancy forces and thus, no motion is sustained in the fluid layer i.e. any fluctuations induced in the flow are damped out by viscosity. When the Rayleigh number exceeds a critical value, disturbances in the flow are not damped out but rather propagate and develop into a quasi-steady motion. The resulting flow consists of a more or less regular cellular or roll patterns. As the Rayleigh number increases further, these regular patterns begin to

disintegrate until finally the flow becomes turbulent. This transition does not occur at a specific value of the Rayleigh number, but rather appears to be completed when the Rayleigh number exceeds 10^6.

The onset of convective motions in fluid layers can occur by the action of gradients caused by the surface tension or density. For thin convective layers (< 1 mm deep), surface tension dominates whereas, buoyancy is more important for thicker layer. Convective motions that occur due to surface tension gradients are called Benard-Marangoni convection, however density gradients result in the so-called Rayleigh-Benard convection. Benard-Marangoni convection is a free surface configuration of Rayleigh-Benard that occur in a thin layer of fluid that is in contact with air (Schatz and Neitzel 2001). The surface tension gradient at the free surface appears due to temperature difference between the hot bottom and cold surface. In this case, the parameter which determines the threshold is the Marangoni number which has a critical value of 80 to develop the cells. Rayleigh-Benard convection occurs in thin layer of fluid confined between two thermally conducting plates, one is heated from below to produce a fixed temperature difference. For this case, the critical Rayleigh number is 1708 to produce Rayleigh-Benard convective cells (Bodenschatz *et al.* 2000). In the present study, the flow is highly turbulent and confined between thicker layers of fluid therefore, both Benard-Marangoni and Rayleigh-Benard convection are not expected.

1.3 Applications

The air-water transport of heat and mass during natural convection plays an important role in a variety of fields such as oceanography, meteorology, chemical, mechanical and nuclear engineering. Some important applications in HVAC and

chemical engineering are condensers, evaporators, bubbly flows and reactors. Similarly, estimation of sensible and latent heat fluxes from ocean to atmosphere is important in oceanography and atmospheric sciences, particularly, in global climate studies. An understanding of natural convection process in well-controlled laboratory experiments could lead to an insight into more complex processes found in nature.

Due to the larger fractional coverage of earth's surface by water (~ 70%) and due to its substantially higher heat capacity, the bulk of the thermal energy at the earth surface is stored in oceans. The oceans are not only the major heat sink of the planet but also have an immense capacity to absorb dissolved gases such as O_2 and CO_2. Approximately 42% of the solar energy absorbed by the land and sea is transferred back to the atmosphere. The thermal energy transfer from ocean to atmosphere drives atmospheric circulation, while at the same time; ocean acquires energy and momentum from the atmospheric circulation i.e. the wind (Gill, 1982). Sensible and latent heat transfer are two major modes of heat transfer during natural convection processes occurring across the free surface. The sensible heat transfer is caused by the air-water temperature difference, while the latent heat transfer occurs via evaporation. The latent heat transfer is responsible for the bulk of the heat transfer from the surface to air (Volino and Simith 1999). Thus, the rate at which heat and mass are transferred across the air-sea interface greatly affects the weather as well as the long term status of the environment. The major resistance to the air-water heat transfer occurs within the thermal boundary layers above and below the interface, where the sensible and the latent heat transfers occur through molecular conduction and diffusion, respectively. Thicker the boundary layer, larger would be the resistance and hence, lower transfer rate. Due to the higher airside

resistance for water vapor, the airside processes control the latent heat transfer. When turbulence is strong, the turbulent eddies above and below the interface also influence the transport process. They reduce the thickness of the thermal boundary layer or even disrupt it and hence, enhance the air-water heat transfer (Csanady 2001, Kantha 2000). It has been observed that the turbulence on both sides of the interface is the controlling factor for the transport of heat and mass across the air-water interface. The development of climatological models requires an understanding of various parameters and phenomena which mediate the transfer of heat and mass across the interface (Saylor and Handler, 1997). In addition, the global climate models also rely on the parameterization of these small-scale air-water gas and heat exchange processes. Thus, an improved understanding of these processes and the factors that influence them is necessary for accurate global climate estimates.

As mentioned earlier, the heat and mass transfer across the air-water interface is controlled by small-scale physical processes in the near-surface region. Due to the complex nature of flow and unavailability of advanced measurement techniques, the flow and temperature characteristics in this very crucial region are not well understood. The present research is aimed at improving the fundamental understanding of heat and mass transport across the interface and the physical process(es) that influence this transport. A better understanding of transport processes will lead to improve heat and mass transfer models that will provide more accurate estimates of heat and mass transfer rates across the air-water interface during natural convection.

1.4 Literature Review

The natural convection in a coupled air-water system appears to be a simple process. However, the flow and thermal behavior of air and water fields during this process is still not well understood. There are relatively few studies reported in the literature that investigated the natural convection beneath air-water interface and no laboratory experimental investigation has been reported on the airside velocity measurements above the interface. Most of the early work was devoted to determine the amount of heat transfer through the fluid layer and to analyze the flow and thermal fields qualitatively. The present review is focused on the reported measurements of the hydrodynamic and thermal fields during natural convection and some of its applications in the atmospheric sciences.

1.4.1 Visualization Studies

Thomson (1882) was the first scientist who described "tessellated structure" at the surface of warm soapy water cooling evaporatively. He found that the surface of the water was cooled from above by evaporation and plunged into the warm bulk water below. First controlled laboratory experiments on convection were conducted by Benard (1900, 1901) who reported the onset of thermal convection in a thin layer of fluid between the horizontal surfaces. He observed the reticulated and cellular convective cells in the fluid as the temperature of the lower plate increased and later these cells are named after him as Benard cells.

Lord Rayleigh (1916) theoretically investigated the natural convection problem. He found that the fluid instability starts when a non-dimensional parameter (named after him as Rayleigh number), reaches a certain critical value. Linear stability analysis of

Rayleigh-Benard convection leads to the well known result that at a critical Rayleigh number of 1708, the onset of motion starts in the fluid in the form of steady contra-rotative rolls called Rayleigh-Benard cells. For Rayleigh number up to approximately 10^4 basic roll cell patterns lead to Benard hexagons, zig-zag rolls and cross-rolls (Busse 1978). At Rayleigh number of 10^4 cells becomes oscillatory and skewed in shape. Beyond Rayleigh number of approximately 10^5, cell patterns becomes chaotic and there is a transition to turbulence and after 10^6, the convection is fully turbulent.

Spangenberg and Rowland (1961) used Schlieren photography to study the convection currents induced by evaporation at the water surface. They observed that the cool water surface collects along lines, which causes local thickening of the surface layer that becomes unstable and plunges into deeper water in the form of sheets. These plunging regions sometimes appear straight, sometimes curved and branched or terminated with no fixed pattern. They also observed that the form of the plunging regions generated at the surface is time-dependent and changes continuously. They found more sheets per unit area with an increase in the heat flux. For higher temperature difference between water and air, they observed that the surface pattern changed its appearance more rapidly than that at the lower temperature difference, with more vigorous convective circulations. Their estimated critical Rayleigh number was 1193 at which convective currents are established in deep water. Their work was mainly focused on flow visualization and the authors did not measure the temperature field or the heat flux.

Chernous'ko (1971) studied the flow patterns at the water surface during natural convection using the powdered dye sprinkled over the surface. He observed small

vortices 1 to 3 cm in size which extended from the free surface down to depths of 7 to 10 cm. He also observed that these vortices occasionally appeared at the surface and were independent of the surface area. The images showed that the fluid along the surface converges into lines and plunge into the warmer fluid below similar to the observation of Spangenberg and Rowland (1961). He found that the water temperature has an effect only on the life and number of these vortices. That is, at higher water temperature, more vortices were present that stayed longer on the surface. He argued that the evaporative convection results in a cool layer of water at the air-water interface and that the temperature difference between the top layer and the water underneath depends on the evaporation rate and the range of water temperatures. He also observed that the vortices were generated only when there was a relatively large temperature difference across the air-water interface.

Goldstein and Volino (1995) experimentally studied the onset and development of flow in a thick horizontal layer of water in a tank which was heated from below, for flux-based Rayleigh number ranged from 10^8 to 10^{10}. They used a video camera to study the fluid motion. They observed the inception of fluid motion and the flow development to a quasi-steady state 120 seconds after the start of heating. Their flow visualization showed the growth and breakdown of a conduction layer adjacent to the heated surface. They found that the still fluid above a heated horizontal plate transmits heat first only by conduction until buoyancy forces become strong enough to initiate motion and warm less dense water rises through the denser water above while the dense water falls down through the warm fluid. They also found warm slow moving plumes during natural convection.

1.4.2 Velocity Measurements

Garon and Goldstein (1973) conducted measurements of vertical velocity distribution during natural convection, where the water was heated from below. They observed that at high Rayleigh number, the velocities were relatively small which fluctuate with time and usually completely reverses in direction. They observed that the velocity distribution is mainly a function of the vertical coordinate. They found that the rms vertical velocity was proportional to the one-third power of the distance from the wall.

Adrian *et al.* (1986) investigated the turbulence convection in a horizontal layer heated from below and insulted from above during natural convection. Their results showed that the buoyant thermals and plumes moving through relatively quiescent fluid were responsible for the convective flow field. They found the active buoyant fluid consists of thin, hot sheets and sometimes columns of fluid that originate in the hot conduction layer and ascend through cooler, slowly sinking quiescent fluid. They also presented correlations for temperature and velocity scales in the conduction and convection layers.

Volino and Smith (1999) simultaneously measured the water surface temperature and two-dimensional sub-surface velocity fields using infrared imagery and particle image velocimetry (PIV), respectively. They found that the water surface is being cooled by evaporation and the cooler water surface is plunging into the warmer bulk water below, in sheet-like plumes. They observed cool skin layer at the water surface using infrared imagery and found that the cool skin layer was 0.5 – 2 °C cooler than the bulk for bulk water temperatures of 21 °C and 37 °C respectively. The temperature field they

observed was very complex showing different scales of thermal structures that appear to be randomly located on the water surface. Fig. 1.3 shows a typical IR image of the surface temperature field from Volino and Smith (1999). The figure highlights the complex nature of the temperature field at the water surface during natural convection. Examination of this figure reveals a variety of structures in the surface temperature field. The dark lines correspond to the regions where cold sheet like plumes are generated. They argued that the dark scars visible in the IR image were the results of falling plumes of the cold fluid; these dark features also represent the convergence zones on the surface. They further observed that the vortices located below the water surface, pulled the cold water surface deep into the water and simultaneously pushed the warm bulk water towards the surface. However, no strong correlation between the temperature field and the sub-surface velocity fields were observed.

Flack *et al.* (2001) measured the water surface temperature and subsurface turbulence during natural convection using infrared imagery and two-component laser doppler velocimetry, respectively. They conducted the experiments with two different free-surface conditions; one with a clean surface (shear-free condition) and the other in the presence of a surfactant monolayer. They found significant differences in the subsurface hydrodynamics depending on the surface condition. They observed that the near-surface turbulent intensities were higher beneath the clean surface as compared to the contaminated surface and that this difference decreased with the distance from the free surface. They compared the normalized horizontal and vertical turbulent velocity profiles with that above a heated wall. For the clean surface, they observed maximum streamwise turbulent velocity close to the surface, which decreased with depth. They

attributed this trend to the shear-free boundary condition for the evaporative convection and argued that this behavior differentiates the free surface and solid wall flows, where for the latter case, the streamwise turbulent velocity reaches zero at the wall. The magnitudes of both streamwise and vertical turbulent velocities they observed were significantly lower than that observed above the heated wall, at all depths. Their infrared temperature images of clean and surfactant covered surfaces show a dramatic change in the spatial scales of the thermal structures. The clean surface shows a large range of scales, including very fine structures. In contrast, at the surfactant-contaminated surface, much large-scale structures were observed while the small-scale structures were dampened. They observed that the structures found in the clean case images were highly active as the warm fluid rises to the surface, compared to the structures in the surfactant covered case.

Saylor *et al.* (2000) and (2002) measured surface temperature field from an evaporating water surface using infrared imagery and analyzed the effect of surfactant monolayer on the spatial structure of the temperature field. They found that the presence of surfactant monolayer significantly affects the spatial structure of the temperature field and that the characteristic length scales of the temperature field increased under surfactant covered surfaces. They also observed that the fluid parcels travel much more rapidly and reside for a short period on the surface for clean water surfaces. However, for a surfactant covered surface, the fluid parcels travel slowly on the surface and resulted in larger temperature difference between the surface and the bulk water. Saylor *et al.* (2001) measured the surface temperature and subsurface velocity of water undergoing evaporative convection, using infrared imagery and laser Doppler velocimetry,

respectively. They found cold lines on the water surface in the IR images and argued that these lines correspond to the falling sheets which remain coherent for long periods of time and laterally translated across the surface before they disappear. They argued that the rising plumes bring warm water to the surface and can be interpreted as positive velocity and positive temperature fluctuation, while falling sheets thicken the boundary layer and cool the surface and can be interpreted with negative velocity and negative temperature fluctuations.

Akyuzlu *et al.* (2003) conducted experiments using PIV to investigate the circulation patterns of buoyancy driven flow during natural convection in a tank. The wall temperature and heat flux through the walls were kept constant during the experiments. They found larger velocity magnitudes near the tank walls as compared to the middle portion of the tank. The Rayleigh number range for their experiments was 10^6 to 10^7.

Sparrow and Nunez (1988) numerically simulated the airflow above an evaporative water surface in a two-dimensional partially filled open-topped vertical circular tube. They considered two cases, one with the insulation around the tube and the other without insulation. They studied the airflow patterns in the air column above the water surface in the tube and in the ambient air above the tube. For the case without insulation, they found that the air from the ambient entered the tube through the annular region adjacent to the wall and left the tube from the middle. The exiting mass flow exceeds the entering mass flow as a result of the evaporation which occurred at the water surface. For the case with insulation, they found the reverse trend. That is, the air entered the tube through the middle and left from the annular region adjacent to the wall. The

argued that this reversal reflects the rearrangement of the buoyancy field caused by the vertical upward increase in temperature at the tube walls. Their velocity profiles also reflected a decelerating flow in the direction from the tube opening to the water surface. This deceleration was small in the upper portion and substantial in the lower portion of the tube where appreciable turning of the flow occurred. They concluded that the diffusion-driven transport alone is insufficient, and that natural convection in the gas-vapor space must be taken into account.

1.4.3 Temperature Measurements

Investigation of the temperature field in the thermal boundary layer below an evaporative water surface is of considerable interest because it controls the convective motions within the water body in the form of falling cold sheets and rising warm plumes. Immediately below the water surface, a thin layer exists within the boundary layer, through which the heat transfer occurs via molecular condition (Katsaros *et al.* 1977). This thin layer dictates the heat transfer across the air-water interface. Most of the previous studies on the natural convection were performed between parallel plates uniformly heated from below and cooled from above and used point measurement techniques (e.g. Deardorff and Willis 1967, Goldstein and Chu 1969, Thomas and Townsend 1957 and Fitzjarrald 1976). The use of point measurement techniques has limitations due to physical intrusiveness which could alter the velocity and temperature fields, and the volume of the sensing element compared to the flow scale. The main objectives of these studies were to determine the mean temperature distribution and overall heat transfer during natural convection.

The only detailed analysis of the temperature field in the thermal boundary layer beneath the water surface during natural convection is reported by Katsaros *et al.* (1977). They measured the mean and instantaneous temperature profiles using resistance thermometer, traversing parallel and perpendicular to the surface. The experiments were conducted in the Rayleigh number range of 3×10^8 to 4×10^9. They observed that the measured mean temperature profile in the boundary layer was highly nonlinear and away from the surface, the temperature variations were organized showing an almost constant temperature. From the data and visualization of the flow, they deduced that the cold fluctuations were due to cold water plunging down from the boundary layer just under the surface. They argued that the thermal boundary layer acts as a source of the fluid for the cold sheets and warm water enters the boundary layer from below by advection.

Goldstein and Chu (1969) used Mach-Zender interferometer to study the thermal convection in an air layer bounded above and below by rigid constant temperature boundaries for a Rayleigh number range from sub-critical (< 1708) to 10^8. They found that the horizontal air layer becomes unstable at a Rayleigh number of 1783 ± 60 and observed periodic cells. The mean temperature distribution curve showed a steep gradient that exists near the wall and its slope became smaller away from the wall until the mean temperature profile became flat in the mid-plane.

Chu and Goldstein (1973) measured overall heat transfer and mean temperature distribution of turbulent thermal convection in horizontal water layers heated from below using Mach-Zender interferometer for Rayleigh numbers between 10^5 to 10^7. They found that the main heat transfer mechanism is the release of thermals from the boundary layers. They also observed that at low Rayleigh numbers, these thermals reached the

opposite surface and coalesce to form large masses of warm fluid near the cold upper surface. However, at high Rayleigh numbers, the thermals move horizontally near the bounding surfaces and the majority of thermals dissipate without reaching the opposite surface. They found that the mean temperature distribution for the high Rayleigh number follow z^{-2} power law.

Thomas and Townsend (1957) measured temperature field during natural convection above a heated horizontal surface in air, with and without cold upper boundary. They found that for convection between parallel plates, nearly all the temperature drop occurred within the wall layers. They found that at high Rayleigh number, the heat transfer coefficient is proportional to the cube root of the Rayleigh number. They argued that the conditions near each surface dictate the heat transfer and that the temperature gradients are negligible in the central region. They also found close correlation between heat transfer from a single surface and heat transfer between the parallel planes.

Sparrow *et al.* (1970) performed experiments to explore the qualitative and quantitative characteristics of thermals ascend through the water above a heated horizontal surface using an electro chemical technique. They also measured water temperature above an active site of thermal generation. They observed mushroom-like thermals with nearly hemispherical cap. They observed the conduction layer thickness of 0.1 – 0.2 cm which breakups at the critical Rayleigh number and produces thermals. Deardoff and Willis (1967) investigated the thermal convection in air between horizontal plates maintained at constant temperatures for a Rayleigh number range of $10^6 - 10^7$. The vertical profiles of horizontally averaged temperature showed the characteristic boundary

layer behavior near the boundaries and nearly isothermal behavior in the central region. They found that the thermal structures are dominated by the plumes extending between the plates.

Kraichnan (1962) theoretically study the turbulent thermal convection for various Prandtl numbers. He investigated the temperature in a region of fluid where turbulent heat and momentum transfer effects are larger than the viscous effects. For high Rayleigh numbers ($Ra \geq 10^5$), he proposed a relation of the form $T(z) = C\, z^{-n}$ for the fluid mean temperature. He considered three different regions; (i) region adjacent to the wall (i.e. conduction layer) where molecular conduction and viscosity dominates, (ii) intermediate region where eddy conductivity and molecular viscosity dominates and (iii) the bulk region where eddy conductivity and eddy viscosity dominates. From the theoretical analysis he found that for high Prandtl numbers ($Pr > 0.1$), in the third region, where eddies transfer both heat and momentum to the bulk of the fluid, the temperature has $z^{-1/3}$ dependency. In the intermediate region that lies between the conduction layer and bulk region where eddy and viscous momentum transfer are of equal magnitude, the temperature varies as z^{-1}. In the conduction layer, the temperature varies linearly with z.

Sakakibara and Adrian (1999) measured the temperature field in a thermally stratified layer of water over a heated horizontal surface using two-color laser induced fluorescence (LIF). They used Rohdamine B and Rohdamine 110 fluorescent dyes, as temperature indicator. For their experiments, mean heat flux was 27 kW / m^2, the mean temperature drop from the heated surface to the center of the mixed layer was 15 K and the Rayleigh number was 1.3×10^7. They observed that the flow field was dominated by turbulent structures in the form of plumes, ridges and thermals. They argued that the

plumes, which consist of column of buoyant fluid rising from the thermal boundary layer, are results of the instabilities of the thermal boundary layer.

Coolen *et al.* (1999) investigated temperature field between hot and cold walls, during natural convection using laser induced fluorescence (LIF) technique. They used Rhodamine B fluorescent dye as a temperature indicator. They observed temperature stratification in the middle of the test section and large temperature gradients near the hot and cold walls. However, they were more focused on the technique and qualitative behavior of the temperature field, and did not present any quantitative results. Their main focus was to verify the experimentally measured temperature field with the numerically estimated field using finite element package SEPRAN.

Analysis of the thermal and hydrodynamic fields is also important from the perspective of the atmospheric sciences for weather forecasting and energy budget calculations. Energy transfer from the ocean and lands to the atmosphere greatly affects the weather as well as the long term status of the environment. The heat fluxes in the climate models are parameterized in terms of the variables on the airside, such as, wind speed (Csanady 2001) and the Kolmogorov timescale for the surface renewal of the airside thermal boundary layer (Clayson *et al.* 1996). However, not much attention has been paid to investigate the influence of small scale physical processes across the interface on the rate of air-water heat transfer (Zappa 1999). The influence of air and waterside physical processes on the air-water heat transfer could be significant. In the following, a brief literature review from the atmospheric sciences perspective is presented.

1.4.4 Atmospheric Stratification

Global wind measurements provide valuable information for atmospheric stratification and weather forecasting. The geophysical modeling of convective currents, waves and exchange of heat, water vapors, gases and aerosols at the interface between the ocean and atmosphere, is important to understand and predict global climate (Bauer 1997). The wavenumber spectra at large-scales show a power law of -3 (i.e. k^{-3} dependency) in which the energy is fed to the atmospheric system through baroclinic instabilities, which arises from the existence of the meridional temperature gradient in the atmosphere. However, at smaller scales, atmospheric turbulent motions are excited by the convective currents, shear flow and breaking waves (Nastrom *et al.* 1984). The turbulent motions at small scales are considered to be horizontally isotropic and are characterized by the spectral slope of $k^{-5/3}$ (Bauer 1997).

In a stratified atmosphere, the flow dynamics is buoyancy driven and thus, the buoyancy forces play a significant role in atmospheric circulation. Buoyancy introduces a source of kinetic energy removal in addition to the viscous dissipation. Turbulent interacting structures in the atmosphere consist of a wide range of scales and cascade energy from large scales to small scales and eventually dissipate to heat as viscous dissipation. The meteorological approaches for atmospheric circulations have been modeled in the past using different approximations such as, homogeneously stratified atmosphere with a constant potential temperature gradient, which gives qualitative insight into the general effects of stratification. However, the turbulence theories and direct numerical simulations generally use the Boussineq approximation or only model the large scales by assuming that they are completely stratified (i.e. two dimensional and flat).

Majority of the theories consider that all regions are isotropic in which horizontal structures are dominated by energy fluxes, while vertical structures are dominated by buoyancy fluxes.

Nastrom *et al.* (1984) and Nastrom and Gage (1985) used Global Atmospheric Sampling Program to compute horizontal kinetic energy spectra over a wide range of scales. The data used by them was collected from flights of instrumented commercial airlines. They conducted a detailed analysis of the zonal wind (u) and meridional wind (v), over the oceans and in upper troposphere. They observed spectral energy decay as k^{-3} at long wavelengths and $k^{-5/3}$ at smaller wavelengths. These spectra found to be consistent with several predictions of two-dimensional isotropic turbulence models.

Freilich and Chelton (1986) determined the spatial structure of near surface oceanic winds using Seaset-A Satellite Scatterometer (SASS) in four latitudinal bands, over the Pacific Ocean. They found that in each of four geographic regions, the spectra of meridional and zonal wind components and kinetic energy are consistent with a power-law dependence on wavenumber and this dependency is identical to that of the two-dimensional isotropic kinetic energy spectrum. They also found that the spectral dependency on wavenumber is nearly the same for both velocity components and for kinetic energy. Their SASS data also show an approximately k^{-2} slope which lies between k^{-3} and $k^{-5/3}$ represents the transition region due to stronger convective source. Cho *et al.* (1999) examined the horizontal wavenumber spectra of horizontal velocity above the Pacific Ocean to see the effect of atmospheric fluctuations at scales 1-100 km. The data of the longest straight-and-level flight showed that the resulting horizontal velocity

spectrum display a k^{-3} dependency at scales greater than 100 km and approximately $k^{-5/3}$ dependency at shorter scales.

The global meteorological analyses are devoted to determine the energy spectra and power law dependency from large to small wavelength ranges in atmosphere through numerically models and field experiments. The data collection is normally made from flights of instrumented commercial airlines, research aircrafts, satellite and land-based instruments. The researchers argue that in the troposphere, which is the lowest portion of earth's atmosphere, geostrophic turbulence is responsible for the large scales and isotropic three-dimensional (3-D) turbulence is responsible for short scales. But the energy transfer phenomenon at small scales (like convective plumes) are unresolved by the numerical models, introduce additional uncertainty into the forecasts. Aside from the fundamental theoretical interest, this problem has implications in applied areas such as accurate weather forecasting and pollutant transport (Koshyk and Hamilton 2001). Different approaches to analyze atmospheric turbulence break the range of large active scales (planetary scales) to small dissipative scales in which different power law regimes exist. In addition, most of the global climatic models for weather forecasting above oceans and land have wind velocity measurements at heights 10 m and above in the troposphere because troposphere is the most turbulent part of the atmosphere and data collection is cumbersome. Thus, they cannot capture the near-surface dynamics and near-surface small scale physical mechanisms that control the transport of heat and mass. The energy contained by the turbulent structures in the near surface region plays a significant role in atmospheric forcing of the ocean and in air-sea interaction processes (Bauer 1997). Due to the limited work, the flow structure immediately above the air-water

interface is not well understood. A quantitative understanding of the nature of stratification over a wide range of scales and the mechanisms maintaining the kinetic energy spectrum is also not well understood in the atmospheric science. Thus, in order to obtain accurate estimates of the air-water heat and mass exchange during natural convection, a better understanding of the characteristics of airside velocity fields, the energy and buoyancy fluxes, the structure of the turbulent cascade and the power law existence and their impact on the exchange process is necessary, particularly, in the near-surface region.

1.5 Motivations and Objectives

As evident from the preceding literature review, most of the previous laboratory studies were focused on the waterside flow characteristics during natural convection. However no detailed investigation of the waterside and airside turbulent flow field from an evaporative water surface is documented in the literature. Without a deep insight into the turbulent structure of the flow, the better understanding of the heat and mass transfer mechanisms is difficult to achieve. In addition, no laboratory experimental investigation of the airside velocity field and no numerical simulation work describing the simultaneous air and water flow characteristics in a coupled air water system during natural convection have been reported in the literature. The moisture content on the airside controls the evaporation rate and thus, the latent heat transfer, which is the dominant mode of heat transfer through evaporative water surface. Therefore, understanding of the airside flow behavior is vital to improve our understanding of the latent heat transfer in particular and the overall heat transfer in general in coupled air-water systems. The understanding of the role played by the airside and waterside velocity

fields in heat transfer during natural convection is important to comprehend the dynamics of the process. During natural convection, the air and water velocity fields are considered to be stagnant and therefore, the impact of the velocity fields is not considered in the computation of sensible and latent heat transfer. But in reality this is not the case, the magnitudes of the air and water velocity components are dynamic and non-zero, and the convective vortices induced in the flow could have an influence on the heat transfer. Therefore, proper consideration of these effects is important in order to obtain improved parameterization of the air-water heat transfer rate. Understanding of the transport processes in the atmospheric boundary is also important in the fields of meteorology and climate modeling. Therefore, well-controlled laboratory experiments is the best alternate to obtain a better understanding of the transport in the atmospheric boundary layer and to develop better parameterization of heat and mass transport models used in global climate models for more accurate predictions.

The main objective of this research is to study the structure of thermal and hydrodynamic fields within the fluid layers above and below evaporating water surface during natural convection. It is also of considerable interest to determine the spectral distribution of turbulent kinetic energy and its decay and to determine the scales of turbulent motions that influence the natural convection process.

1.6 Thesis Outlines

This dissertation is a "Manuscript-Based" dissertation which consists of a collection of research papers that have a cohesive character of a single research as per rules and requirements defined in the Thesis Preparation and Thesis Examination Regulations booklet of the School of Graduate Studies at the Concordia University. The

results of the present study are self-contained that is, they can be read independent of each other and of any other part of this dissertation.

Chapter 1 introduces the focus of this thesis and motivation of the present work. It also contains the review of the previous work.

Chapter 2 comprised of the article published in the Journal of Heat and Mass Transfer. It describes the simulation results of the air and waterside velocity fields in a coupled air-water system during natural convection. The purpose of this simulation work is to get an understanding of the bulk air and water flow characteristics and behavior under different thermal stratification conditions.

Chapter 3 comprised of the article published in the Journal Physics of Fluids. It presents the experimental results of the waterside turbulent structure beneath an evaporating water surface under neutral and unstable thermal stratification conditions when air field above the water surface was unsaturated.

Chapter 4 comprised of the article submitted to the International Journal of Heat and Mass Transfer. It describes the impact of air saturation on the waterside flow structure during natural convection. This chapter presents a detailed comparison of the experimental results of the horizontal and vertical turbulent velocity fluctuation, turbulent kinetic energy and spectral analysis of the length and time scales under saturated and unsaturated air conditions.

Chapter 5 comprised of the article submitted to Physics of Fluids. It presents the results of the waterside temperature fields during natural convection under unstable conditions. It provides the characteristics of temperature field in the near-surface region, in particular within the conduction layer at the water surface.

Chapter 6 comprised of the article submitted to the Journal of Fluid Mechanics. It presents the detailed analysis of the airside turbulent velocity fields above the evaporative water surface during natural convection. The detailed spectral analysis and similarities with the field observations are also presented in this chapter.

Chapter 7 summarizes main findings and conclusions of the present study and recommendations for the future work.

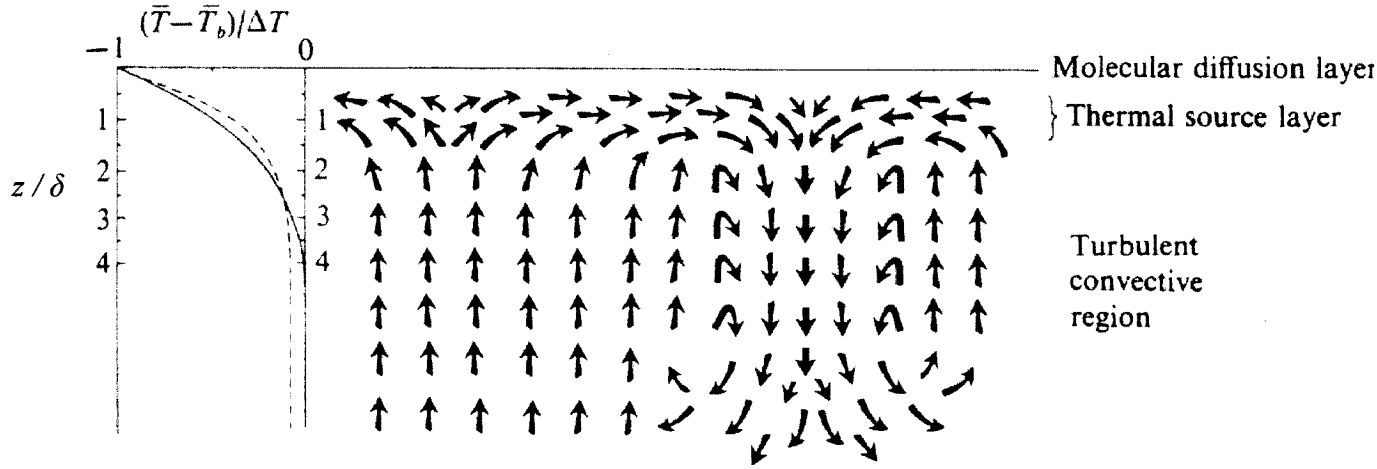

Fig. 1.1. Conceptual mixing model proposed by Katsaros *et al.* (1977).

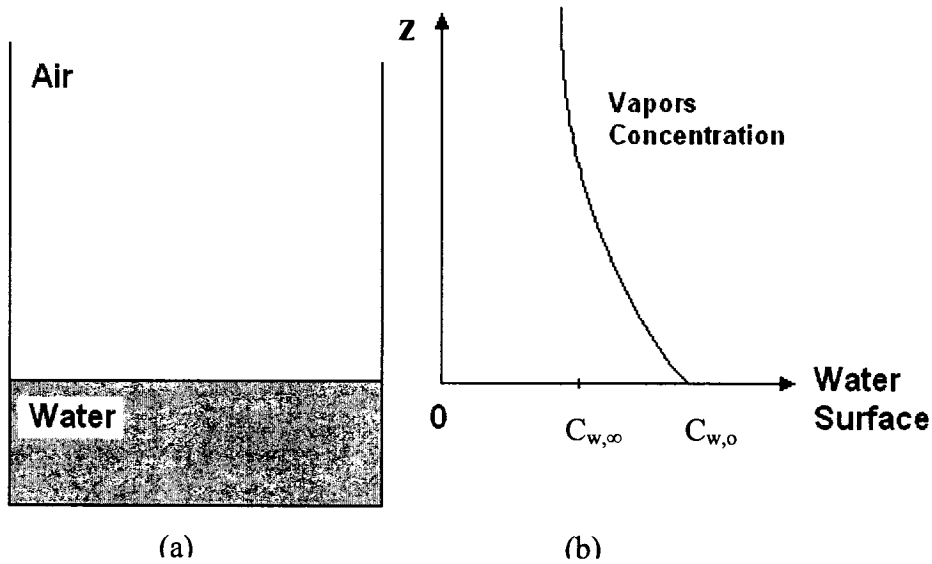

Fig. 1.2. Concentration profile of water vapors in air above air-water interface during natural convection.

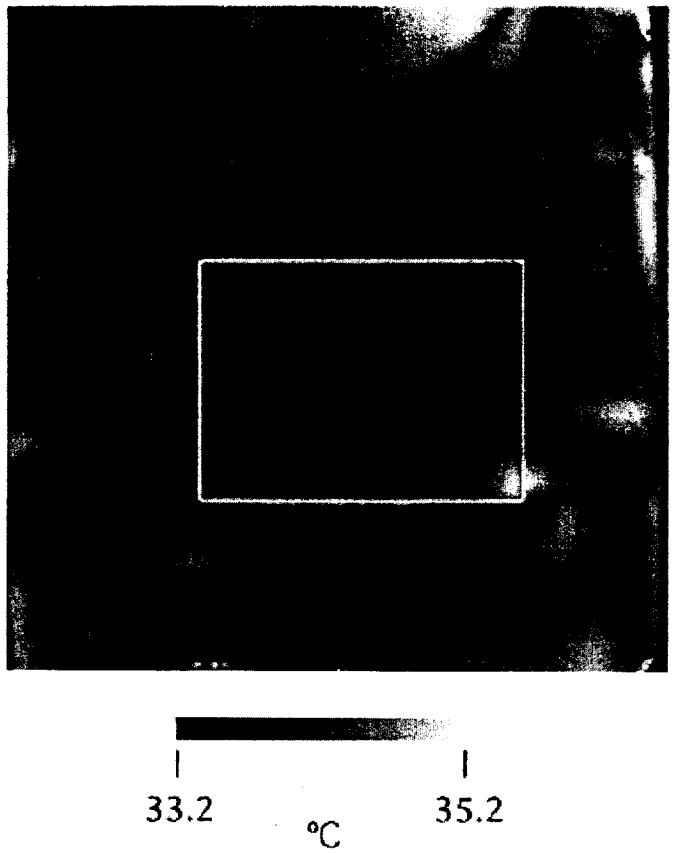

Fig. 1.3. Infrared image of water surface temperature field during natural (Volino and Smith 1999).

Chapter 2

Characteristics of Air and Water Velocity Fields during Natural Convection

2.1 Abstract

Air and water velocity fields have been simulated during natural convection, using a Volume of Fluid (VOF) model. The results have shown that during unstable thermal stratification, the root-mean-square (RMS) airside velocities are an order of magnitude higher than the RMS waterside velocities. The magnitude of the air velocity changed more rapidly with the change in the bulk air-water temperature difference than the water velocity, indicating that the air velocities are more sensitive to the bulk air and water temperature difference than the water velocities. A physical model of the heat and mass transfer across the air-water interface is defined. According to this model, the vortices on the air and water sides play an important role in enhancing the heat and mass transfer. It has been proposed that the correlations for the heat and mass transfer during natural convection should be improved by incorporating the flow velocity as a parameter.

2.2 Introduction

The exchange of mass and heat across air-water interfaces are important in a wide range of applications from environmental to industrial. For example, the heat and mass exchange between the ocean and atmosphere has a significant impact on the global

climate. From the industrial aspect, it is important in the HVAC and chemical process applications such as condensers, evaporators, bubbly flows and reactors.

One of the important phenomena of the coupled air-water system is the natural convection during which, the mass and heat exchange between air and water takes place without any external influence. The air and water temperatures control the evaporation rate and the sensible heat transfer across the interface. In addition, they also influence the air and water velocity fields, which in turn alter the heat transfer rate. Thus, in order to obtain accurate estimates of the air-water heat and mass exchange during natural convection, a better understanding of the characteristics of air and water velocity fields and their impact on the exchange process is necessary. However, not much attention has been paid to investigate the air and water velocity fields during natural convection. Only few studies have reported the velocity measurements on the waterside and no experimental study has been reported on the airside velocity measurements. In addition, as far as the authors know, no numerical simulation work describing the simultaneous air and water flow characteristics in a coupled air and water system undergoing natural convection has been reported.

Volino and Smith (1999) simultaneously measured the surface temperature and two-dimensional sub-surface velocity fields using infrared imagery and digital particle image velocimetry (DPIV), respectively, during natural convection. They found that the water surface is being cooled by the evaporation and the cold water surface is plunging into the warmer bulk water below in sheet-like plumes. They further observed that the vortices located below the water surface, pulled the cold water surface deep in to the water and simultaneously pushed hot bulk water towards the surface. They also found

that the magnitude of root-mean-square (RMS) horizontal and vertical velocities increased for the higher heat flux. However, no strong correlation between the temperature field and the sub-surface velocity fields were observed.

Flack *et al.* (2001) measured the surface temperature of water undergoing evaporative convection using infrared imagery. The subsurface turbulence was measured using two-component laser doppler velocimetry. They conducted the experiments with two different free-surface conditions; one with a clean surface (shear free condition) and the other in the presence of a surfactant monolayer. They observed that the near-surface turbulent intensities were higher beneath the clean surface as compared to the contaminated surface and that this difference decreased with the distance from the free surface. They further observed that the difference in turbulent intensity was largest in the horizontal component of velocity in the near-surface region. They also found that the water surface temperature field was altered in the presence of surfactant, with the disappearance of the fine-scale structures.

Akyuzlu *et al.* (2003) conducted experiments using DPIV to investigate the circulation patterns of buoyancy driven flow during natural convection in a tank. The wall temperature and heat flux through the walls were kept constant during the experiments. They found larger velocity magnitudes near the tank walls as compared to the middle portion of the tank.

Garon and Goldstein (1973) conducted measurements of heat transfer and vertical velocity distribution during natural convection, where the water was heated from below. They observed that at high Rayleigh number, the velocities were relatively very small

which fluctuate with time and usually completely reverses in direction. They also observed that the velocity distribution is mainly a function of the vertical coordinate.

Goldstein and Volino (1995) studied the flow patterns of water in a tank which was heated from below using a video camera. They observed the inception of fluid motion and the flow development to a quasi-steady state. They found that the still fluid above a heated horizontal plate transmits heat first only by conduction until buoyancy forces become strong enough to initiate motion and warm less dense water rises through the denser water above while the dense water falls down through the warm fluid. They also found warm slow moving plumes during natural convection.

Chernous'ko (1971) observed micro-convection at the air-water interface during natural convection. He observed small vortices 1 to 3 cm in size occasionally appeared at the surface and were independent of the surface area. He found that the water temperature has an effect only on the life and number of these vortices. That is, at higher water temperature, he observed more vortices that stayed longer on the surface. He argued that the evaporative convection resulted in a cool layer of water at the air-water interface and that the temperature difference between the top layer and the water underneath depends on the evaporation rate and the range of water temperatures. He observed that the vortices were generated only when there is a relatively large temperature difference across the air-water interface. He further noticed that the vortices were first generated near the water surface, which then moved towards the center.

Sparrow and Nunez (1988) numerically simulated the airflow above an evaporative water surface in a two-dimensional partially filled open-topped vertical circular tube. They considered two cases, one with the insulation around the tube and the

other without insulation. They studied the airflow patterns in the air column above the water surface and in the ambient air above the tube. For the case without insulation, they found that the air from the ambient entered the tube in an annular region adjacent to the wall and left the from the middle. While for the case with insulation, they found the reverse trend. That is, the air entered the tube in the middle and left from the annular region adjacent to the wall.

The heat exchange across the air-water interface could occur under the following three circumstances. When the bulk water temperature is higher than the bulk air temperature, the water is cooled from above and the air is heated from below. This result in the formation of unstable density layers on the air and water sides and it is termed as unstable thermal stratification. When the bulk water temperature is lower than the bulk air temperature, the water is heated from above and the air is cooled from below, resulting in the formation of stable density layers and the process is called stable thermal stratification. The third case, when the bulk air and water temperatures are equal is considered as the neutral case when no strong density variations are observed in both fluids. Most of the previous studies were focused on the investigation of waterside flow characteristics during unstable thermal stratification and no attention has been paid to investigate the flow characteristics during stable thermal stratification. It is true that one does not expect to observe strong activities during this case; however, an investigation of such phenomenon would further improve our understanding of the flow behavior and the heat transfer mechanism under different modes of natural convection.

The present study is motivated by the fact that the understanding of the flow characteristics on both air and water sides is necessary in order to comprehend the heat

exchange processes during the natural convection. To accomplish the task, we simulated the air and water flow fields in a two-dimensional domain. The simulations were conducted for a wide range of conditions that cover the cases for unstable and stable thermal stratifications and neutral conditions.

2.3 Mathematical Model

The buoyancy-driven transport processes are induced by the density difference due to the variations in the temperature and/or concentration fields. In these flows the gravitational field produces an upward buoyancy force and this force induces a motion in the fluid. For buoyancy-driven convection, the fundamental governing equations in a two-dimensional domain are given below (Bejan 1993).

Continuity equation

$$\frac{\partial u}{\partial x}+\frac{\partial \upsilon}{\partial y}=0 \tag{2.1}$$

Momentum equations

$$\rho\left(\frac{\partial u}{\partial t}+u\frac{\partial u}{\partial x}+\upsilon\frac{\partial u}{\partial y}\right)=-\frac{\partial P}{\partial x}+\mu\nabla^2 u \tag{2.2}$$

$$\rho\left(\frac{\partial \upsilon}{\partial t}+u\frac{\partial \upsilon}{\partial x}+\upsilon\frac{\partial \upsilon}{\partial y}\right)=\mu\nabla^2\upsilon+(\rho_\infty-\rho)g \tag{2.3}$$

Energy equation

$$\frac{\partial T}{\partial t}+u\frac{\partial T}{\partial x}+\upsilon\frac{\partial T}{\partial y}=\alpha\nabla^2 T \tag{2.4}$$

Specie concentration equation

$$u\frac{\partial C}{\partial x}+\upsilon\frac{\partial C}{\partial y}=D\nabla^2 C \tag{2.5}$$

where, ρ_∞ is the density of the bulk fluid. In accordance with the Boussinesq approximation, the density difference term in the y-momentum equation is proportional to the temperature difference $(T - T_\infty)$ (for heat transfer) and specie concentration difference $(C - C_\infty)$ (for mass transfer), where T_∞ and C_∞ are bulk temperature and concentration, respectively (Bejan 2004). Thus, the y-momentum equation will become,

$$\left(\frac{\partial \upsilon}{\partial t} + u\frac{\partial \upsilon}{\partial x} + \upsilon\frac{\partial \upsilon}{\partial y}\right) = \nu\nabla^2\upsilon + g\beta(T - T_\infty) + g\beta_c(C - C_\infty) \tag{2.6}$$

where β is the thermal expansion coefficient i.e.,

$$\beta = -\frac{1}{\rho}\left(\frac{\partial \rho}{\partial T}\right)_P \tag{2.7}$$

β_C is the concentration expansion coefficient i.e.,

$$\beta_C = -\frac{1}{\rho}\left(\frac{\partial \rho}{\partial C}\right)_P \tag{2.8}$$

In the present study, we considered a coupled air-water system undergoing evaporative cooling at the water surface. The domain was bounded on the sides and bottom by the walls and open from the top to allow air interactions with the ambient air. Due to the evaporation from the water surface into the air, the convective motion in the air is induced by the combined effect of temperature and vapor concentration gradients. However, due to the limitations in the CFD software (FLUENT) used in the present study, the concentration difference cannot be incorporated into the Boussinesq term in the y-momentum equation (Fluent 6.1 user's guide). Thus, it was assumed that the water vapors added to the air due to evaporation were transferred to the ambient air such that, the vapors concentration in the air inside the tank remained unchanged. Thus, the

temperature difference was considered to be the sole mechanism to induce flow on both air and water sides.

The evaporation from the water surface causes a decrease in the water surface layer temperature due to the latent heat loss. This cool surface layer plays a vital role in the natural convection process underneath. The mass transfer from the water surface was incorporated into the model based on the concentration gradient. Thus, the impact of mass transfer on the waterside flow field was fully considered in the present model. The mass transfer or the evaporation rate from the water surface was computed using the correlation developed by Hinchley and Himus (1924) i.e.,

$$J = 38.3(C_w - C_a)^{1.25} \tag{2.9}$$

where, J is the evaporation rate, C_w and C_a are the water vapor concentrations at the water surface and in the air, respectively. The latent heat was computed by,

$$q''_L = Jh_{fg} \tag{2.10}$$

where, h_{fg} is the latent heat of vaporization. To account for the cooling in the water surface layer due to evaporation, this heat must be added as a sink term in the energy equation (2.4) that is applied in the water surface layer.

2.4 Numerical Model

The coupled air and water velocity fields were simulated in a two-dimensional glass tank. The width and height of the tank were set equal to 20 cm and 25 cm, respectively. The water depth was set equal to 17 cm (see Fig. 2.1). The air temperature was kept constant at 22 °C and water temperature was varied from 7 °C to 37 °C with an increment of 5 °C. The tank top was left open to allow the airflow. The Volume of Fluid

(VOF) model in the FLUENT 6.1 commercial software was used to simulate this two-phase flow. The pressure-velocity coupling was obtained by using the Pressure-Implicit with Splitting of Operators (PISO) scheme, which is based on the higher degree of the approximate relation between the corrections for the pressure and velocity. The PISO scheme is highly recommended for the transient flow calculations with large time steps (Fluent 6.1 user's guide). The PISO algorithm takes relatively more CPU time per solver iteration, but it significantly decrease the number of iterations required for the convergence of the transient flow problems. The convergence criterion was set equal to 1 x 10^{-6} for the energy and 1 x 10^{-3} for other parameters such as velocity and pressure.

2.4.1 VOF Model

The time-dependent Volume of Fluid (VOF) model is appropriate for free-surface flows in which the two fluids are immiscible. It simulates the fluid flows by solving a single set of momentum equations and tracking the volume fraction of each of the two fluids in each computational cell, throughout the domain. The VOF formulation relies on the fact that the two fluids (phases) are not interpenetrating, and that the volume fraction of both phases is equal to unity in each computational cell. The fields for all variables and properties are shared by the phases and represent the volume-averaged values, as long as the volume fraction of each of the phases is known at each location. In any given cell, the variables and properties are either purely representative of a single phase, or a mixture of phases, depending upon the volume fraction values. If $\eta(\vec{x},t)$ is defined as the volume fraction of water in this air-water system, then there are following three possible values for $\eta(\vec{x},t)$ in a particular computational cell:

$\eta(\vec{x},t)=0$, the cell is completely occupied by air.

$\eta(\vec{x},t)=1$, the cell is completely occupied by water.

$0 < \eta(\vec{x},t) < 1$ the cell contains both fluids, that is, the air-water interface is present in the cell.

Depending upon the value of the volume fraction, $\eta(\vec{x},t)$, the properties are calculated and assigned to each control volume. For an air-water two phase system, the density, viscosity and thermal conductivity in a computational cell are given by,

$$\rho(\vec{x},t)=\eta(\vec{x},t)\rho_w+[1-\eta(\vec{x},t)]\rho_a \tag{2.11}$$

$$\mu(\vec{x},t)=\eta(\vec{x},t)\mu_w+[1-\eta(\vec{x},t)]\mu_a \tag{2.12}$$

$$k(\vec{x},t)=\eta(\vec{x},t)k_w+[1-\eta(\vec{x},t)]k_a \tag{2.13}$$

where, ρ_a and ρ_w are the densities, μ_a and μ_w are the viscosities, and k_a and k_w are the thermal conductivities of air and water, respectively. In the VOF model for this study, the air is defined as the primary phase and water as the secondary phase. The choice of the phase affects the solution stability and ease of the problem setup. It is recommended for this model to select the incompressible fluid or the less dense fluid as the primary phase. The volume fraction and properties of the secondary phase are then patched to that of the primary phase. The water volume fraction and its temperature have been patched in this numerical study.

The properties at the air-water interface are determined from the solution of the continuity equation for the volume fraction of water. For the water phase, the continuity equation will become,

$$\frac{\partial \eta(\vec{x},t)}{\partial t} + \vec{\upsilon}.\nabla \eta(\vec{x},t) = S_m \tag{2.14}$$

where S_m is the user defined mass source. At the interface, only single equation of instantaneous motion is solved and the value of the resulting velocity is the same for both air and water. The momentum equation that represents the movement of air and water is,

$$\rho\frac{\partial u_i}{\partial t} + \frac{\partial u_i u_j}{\partial x_j} = -\frac{\partial p}{\partial x_i} + \mu\frac{\partial^2 u_i}{\partial x_j \partial x_j} + \rho g_i \tag{2.15}$$

The single energy equation is also solved for both phases, that is,

$$\rho\frac{\partial E}{\partial t} + \rho\frac{\partial u_i E}{x_i} = \frac{\partial}{\partial x_i}k(\frac{\partial T}{\partial x_i}) + S_h \tag{2.16}$$

where, S_h is the user defined energy source, E is the energy, T is the temperature, i =1,2 and j =1,2. The values of ρ, μ and k are obtained from Eqs. (2.11), (2.12) and (2.13). The Boussinesq approximation was incorporated to account for the convective currents, which is given as,

$$(\rho - \rho_\infty)g \approx -\rho_\infty \beta(\mathrm{T} - \mathrm{T}_\infty)g \tag{2.17}$$

The Spalart-Allmaras turbulent model was incorporated in the present numerical scheme. This model is effective for low Reynolds number flows, where the viscous affected region of the boundary layer has to be properly resolved. In this model, a transport variable $\tilde{\nu}$, is used to form the eddy viscosity and a single transport equation is solved for this variable. The transport equation for the working variable $\tilde{\nu}$ is,

$$\frac{\partial(\rho\tilde{\nu})}{\partial t} + \frac{\partial(\rho\tilde{\nu}u_i)}{\partial x_i} = G_\nu + \frac{1}{\sigma_{\tilde{\nu}}}\left[\frac{\partial}{\partial x_j}\left\{(\mu + \rho\tilde{\nu})\frac{\partial \tilde{\nu}}{\partial x_j}\right\} + C_{b2}\rho\left(\frac{\partial \tilde{\nu}}{\partial x_j}\right)^2\right] - Y_\nu \tag{2.18}$$

where, G_v is the production of turbulent viscosity, Y_v is the destruction of turbulent viscosity that occurs in the near-wall region due to viscous damping, and σ_v=0.667 and C_{b2}=0.662 are constants (Fluent 6.1 user's guide).

As discussed in section 2.3, the mass transfer and latent heat loss from the water surface layer is considered in the numerical model. There is no universal model available in the FLUENT software for the mass transfer. The mass and latent heat transfer given in equations (2.9) and (2.10), respectively, were incorporated into the numerical model via user defined functions (UDF). The UDF for the mass transfer was applied to the continuity equation (eq. 2.14) as a sink term for the water and the UDF for the latent heat transfer was applied as a sink term in the energy equation (eq. 2.16). In the UDF for mass transfer, the vapor concentration on the airside was computed based on the fixed relative humidity at 50% and the vapor concentration at the water surface was computed based on the instantaneous water temperature at the surface.

Katsaros *et al.* (1977) argued that the water surface layer where the molecular diffusion dominates is very thin. Based on the temperature profiles from their experiments, they suggested that the thickness of this layer could be up to 0.25 mm. Adrian *et al.* (1986) proposed scaling parameters to define the thickness of this layer. By applying the Adrian *et al.* (1986) scaling to the data of Volino and Smith (1999), the thickness of the surface layer was found to vary from approximately 0.3 - 0.5 mm. In the present numerical model, we defined an interface layer with depth equal to 0.5 mm. Both UDF's were applied to the waterside in this layer. For each case, initially, this layer was completely occupied with water. As the time progressed, the water depth in this layer

decreased due to evaporation. However, for the total simulation time, it was observed that the change in the water depth was less than 4% for all cases.

The hydrodynamic boundary condition applied on all the walls was no slip condition. The thermal boundary condition on the walls in the air domain was convective boundary condition and the thermal boundary condition on the walls in the water domain was constant heat flux condition. The heat transfer coefficients at the vertical and horizontal walls in the respective domains were computed using the standard correlations (Incropera 2001). To compute the heat flux through the walls on the waterside, the heat transfer coefficient of the outside air was also computed.

2.4.2 Methodology

The simulations were conducted for a range of bulk air-water temperature differences under stable and unstable thermal stratification and neutral conditions. The initial water-air temperature difference is defined as, $\Delta T = T_w - T_a$, where, T_w and T_a are initial water and air temperatures, respectively. For these simulations, the initial air temperature was set constant at 22 °C and the initial water temperature was varied from 7 °C to 37 °C with an increment of 5 °C, for different cases. That is, ΔT was varied from -15 °C to 15 °C. The natural convection is stably stratified for $\Delta T < 0$ and unstably stratified for $\Delta T > 0$.

The grid independence was investigated by conducting simulations for different mesh sizes ranging from 0.35 cm to 0.2 cm at an air-water temperature difference of 15 °C (water at 37 °C and air at 22 °C) under the same boundary conditions. The structured quadrilateral mesh was considered. The RMS velocities were used as the criterion for the grid independence. It was found that for mesh size less than 0.27 cm, the variations in the

RMS horizontal and vertical velocities were less than 0.8% and 1.7%, respectively. This indicates that for mesh smaller than 0.27 cm, the numerical solution does not depend on the mesh size. Thus, in the present study, the structured quadrilateral mesh of size 0.25 cm was used. The time step was set equal to 0.02 s. For time dependent solution formulations, we have selected first order implicit scheme. The advantage of this implicit scheme is that it is unconditionally stable with respect to time step. A good way to judge the choice of Δt is to observe the number of iterations the FLUENT needs to converge at each time step. The ideal number of iterations per time step is 5 - 10 (Fluent 6.1 user's guide). Our selected time step takes 5 - 12 iterations to converge the solution. Therefore, it can be argued that the selected simulation scheme and the numerical results are independent of time step as well as the mesh size. For each case, the simulation was conducted until the air and water velocities reached a quasi steady state and when no large variations were found in the instantaneous velocity fields.

2.4.3 Validation

There are not many experimental results available in the literature for the two-dimensional instantaneous waterside velocity fields under natural convection. The results of this numerical model have been validated with the experimental results of Volino and Smith (1999). The tank domain and the water depth used in the present study were the same as that of Volino and Smith (1999). They used a glass tank of 40 cm long, 20 cm wide and 25 cm high. The water depth was maintained at 17 cm. The tank was open from the top to allow evaporation. They measured the two-dimensional velocity fields in a vertical plane over a 11 cm x 8 cm region. For the experimental measurements conducted at an air-water temperature difference of 15 °C (water at 37 °C and air at 22 °C), they

found the RMS horizontal and vertical velocity magnitudes equal to 0.13 and 0.21 cm/s, respectively. The RMS values obtained from the present simulation under the same set of conditions for horizontal and vertical velocity components are 0.161 and 0.195 cm/s, respectively. There is a 13% difference in the numerical and experimental data. This showed that the results obtained from the simulation are in good agreement with the experimental data. In addition, the magnitudes of the large velocity vectors from the experimental data of Volino and Smith (1999) were comparable with the magnitudes of large velocity vectors obtained from the simulation.

The numerical scheme could not be validated for the airside simulations because there is no experimental airside velocity data available in the literature for the natural convection. As mentioned in section 2, the impact of the concentration gradient was not considered in the given model due to the FLUENT limitations. This would affect the magnitude of the simulated airside velocities. We have estimated the error in the airside velocity magnitude due to this issue by comparing the magnitudes of the body forces due to temperature and concentration differences in the momentum equation. The same approach was used by Gebhart and Pera (1971) to estimate the relative impact of the temperature and concentration differences on the convective motion. It was found that ignoring the effect of concentration gradient could induce an error of 25 – 30 % in the air velocity except for the neutral case where this error would be even larger.

2.5 Results

The air and water velocity fields were simulated simultaneously under natural convection in the presence of stable and unstable thermal stratifications. The transient state of the waterside velocity field for the case of unstable thermal stratification is shown in Fig. 2.2 for $\Delta T = 15\ ^{\circ}C$. The plot in Fig. 2.2 (a) shows that at 20 seconds after the start of the process, the bulk motion on the waterside is very small. However, thermal plumes are visible along the sides of the tank. These plumes are generated due to the heat transfer from the sidewalls, which causes a decrease in the water temperature along the side, thus, increasing its density. As the water slides down along the wall, its temperature further decreases, resulting in an increment in the magnitude of vertical convective current. A similar trend was observed by Akyuzlu *et al.* (2003). As the time increases, two counter-rotating vortices are induced in the flow (see Fig. 2.2 (b)). The velocity field after 100 and 140 s are shown in Figs. 2.2 (c) and 2.2 (d), respectively. The two counter-rotating vortices are still prominent in the plots. The results have shown that this vortex pair persists as long as the convective motion exists in the fluid. By tracking the axes of rotation of both vortices in Fig. 2.2, it is found that initially the axis of rotation of both vortices was close to the interface. That is, these vortices were formed very close to the interface where, the temperature gradients were high and the convective motion was initiated across the interface (Goldstein and Volino 1995). As the time passes, both vortices moved deeper into the water (Figs. 2.2 (b) and 2.2 (c)) and then they ascend over a small distance and stay there for the rest of the time (see Fig. 2.2 (d)). This trend is similar to Chernous'ko (1971) who observed that the vortices were first generated near the water surface and then moved towards the center. The two-dimensional velocity plots

of Volino and Smith (1999) have also shown a similar downward bulk motion near the middle of the tank. Their field of view was smaller than the tank dimensions, therefore, the bulk convective motion present in their tank was not captured. They also observed some small-scale local vortical motions, which could be associated with the convection-driven turbulence. In the present study, we did not simulate the turbulence produced by the convective motions, as a result, we were not able to resolve any flow characteristics related to the turbulence. The focus of the present study is to investigate the bulk mean motion of the fluids.

The transient state of the airside velocity fields for ΔT = 15 °C are shown in Fig. 2.3. The plots in Fig. 2.3 show that at the beginning of the simulations, two weak vortices are observed near the corners of the tank, which initiates the convective motion on the airside. As the time passed, the convective motion on the airside became stronger and both vortices shifted towards the center of the tank, as shown in Fig. 2.3 (d). The results in Fig. 2.3 also indicate the transient phase of the airside vortices is relatively very short. The vortices were stabilized within 20 s. Whereas, on the waterside, the vortices were stabilize after approximately 120 s. No organized motion was observed in the water at t = 20 s (see Fig. 2.2 (a)). The comparison of the air and water velocity fields show that the magnitude of the strong airside convective motion is more a factor of five larger than that on the waterside. It can also be noted that the horizontal locations of the center of airside vortices are approximately coincides with the horizontal locations of the center of waterside vortices. Since the airside vortices were formed earlier and they are stronger, it is likely that the airside vortices control the location of the waterside vortices. The analysis of the air and water velocity fields during stable thermal stratification has shown

no organized bulk vortical motions on the air and watersides. Instead, localized weak bursts of fluid parcels were observed mostly near the air-water interface.

The plots in Fig. 2.3 also show that the ambient air enters the tank along the walls and leaves from the center. Sparrow and Nunez (1988) simulated the air flow above the water in open-topped tube. They observed that the air entered the tube along the wall and left through the middle, which is consistent with our results. Bejan (1993) also argued that if the air column above the water surface is wide enough, the humid air rises by natural convection through the center of the column and the dry air descends along the walls.

The waterside instantaneous vertical velocity at a depth of 5.5 mm from the interface and a distance of 9 cm from the right wall, is shown in Fig. 2.4 (a) as a time function, for different values of ΔT. The plot shows that for stable thermal stratification, the magnitude and variations in the velocity data are relatively small as compared to the unstable case. For the unstable case (i.e. $\Delta T > 0$), the plot shows that initially there are relatively large variations in the velocity data, and after approximately 300 s the velocity reaches a quasi-steady state. Garon and Goldstein (1973) also observed large variations in the vertical velocity of water during unstable convective motion, which then reached the quasi-steady state. The airside instantaneous vertical velocity component at a location 5 mm above the interface and at 9 cm from the right wall, is shown in Fig. 2.4 (b) as a time function, for different values of ΔT. For unstable thermal stratification, the initial variations in the airside velocities are relatively small and it reaches the quasi-steady state in shorter time. For stable case, however, some variations were observed in the velocity

data during the time interval from 200 to 300 s and then the velocity reached the quasi-steady state.

The horizontal component of water and air velocities at the locations same as in Fig. 2.4 are plotted in Fig. 2.5 (a) and 2.5 (b), as a time function, respectively. The plots show the trend similar to the vertical velocity. However, the magnitude of the horizontal velocity component was approximately a factor of three to five greater than the vertical component for both air and water, which is expected close to the interface (Flack *et al.* 2001).

The magnitude of the airside and waterside velocity fields are quantified in terms of the Root-Mean-Square (RMS) velocities. Since the mean components of the horizontal and vertical velocities are zero for both flow fields, the RMS velocity represents the magnitude of the velocity fluctuations. That is,

$$(u_i)_{RMS} = \sqrt{\overline{u_i^2}} \tag{2.19}$$

where, i = 1,2. Several studies (e.g. Flack *et al.* 2001, Garon and Goldstein 1973) have used RMS velocities to express the velocity magnitude in their natural convection study. The RMS horizontal and vertical velocities for water and air are plotted in Figs. 2.6 (a) and 2.6 (b), respectively, as a function of ΔT. These values were computed 100s after the quasi-steady state was reached in each case. The results show that the magnitude of both velocity components increases as the temperature difference between air and water increases.

Comparison of the RMS velocities for stable and unstable cases shows that for both air and water, the magnitudes of horizontal and vertical velocity components are larger during unstable thermal stratification, which is most likely due to the generation of

strong convective currents. The plots also show that for any given condition, the magnitude of RMS vertical velocity is higher than the RMS horizontal velocity. The results also show that the magnitudes of the waterside RMS velocities for stable thermal stratification are approximately 40-50% lower than that for the unstable case for the same air-water temperature difference, i.e. same $|\Delta T|$. However, for the airside, the magnitude of RMS velocities for the stable case is one to two orders of magnitude smaller than that for the unstable case. This indicates that the flow field on the airside is very sensitive to the values of ΔT. The comparison of Figs. 2.6 (a) and 2.6 (b) shows that the magnitude of airside velocities is more than an order of magnitude larger than the waterside velocities for $\Delta T > 0$. However, for $\Delta T < 0$, the velocity magnitude is comparable for air and water. This indicates that stronger buoyancy-driven convective currents are induced on the airside during unstable thermal stratification.

2.6 Discussion

The plots in Figs. 2.2 and 2.3 have shown that counter-rotating vortices are generated in air and water flow fields during unstable thermal stratification. The waterside vortices bring the parcels of bulk warm water to the surface and take the parcels of cold water from the surface to greater depths. Similarly, the airside vortices bring the parcels of bulk cold air from above to the surface and take away the parcels of warm air from the surface. However, no such organized motions were observed during stable thermal stratification.

There are two modes of heat transfer across the air-water interface, i.e. sensible and latent heat transfer. The sensible heat transfer is due to the air-water temperature difference, while the latent heat transfer is due to the evaporation of water molecules

from the water surface. The mechanism of heat and mass transfer across the interface in a coupled air-water system during unstable stratification can be explained by a physical model, as follows. The waterside vortices bring the parcels of warm water from the bulk to the surface. The heat is transferred across the air-water interface in the form of sensible and latent heat, to the air parcels adjacent to the interface. The airside vortices then transport these parcels of warm and moist air away from the interface. Thus, the surface renewal process tends to maintain the maximum possible temperature difference in the layers adjacent to the interface, resulting in the enhancement of the sensible heat transfer. From the perspective of latent heat, the airside boundary layer adjacent to the interface tends to become saturated in a relatively short time, causing a reduction in the latent heat transfer. However, the vortices on the airside remove this layer of higher moisture content and replace it with the low vapor concentration layer. This will cause an increase in the evaporation rate and thus, an increase in the latent heat transfer. Therefore, it can be argued that the airside and waterside vortices play an important role in enhancing the heat and mass transfer across the air-water interface.

The role played by the airside and waterside vortices in the heat and mass transfer could not be the same. The latent heat transfer constitutes the bulk of the total heat transfer from water to air during the unstable and neutral cases. The waterside vortices do not contribute significantly to the evaporation rate. The transfer of water vapor into the air is controlled by the airside processes (Liss 1973). That is, the resistance to the mass transfer lies on the airside. The water surface temperature also affects the evaporation rate but its influence is very small. Thus, the vertical transport of air masses by the airside

vortices would be the dominant factor in controlling the evaporation rate and thus, the latent heat transfer.

During the natural convection, the impact of the air and water velocity fields is not considered in the computation of sensible and latent heat transfer. That is, the correlations developed to estimate the sensible and latent heat fluxes are based on the thermodynamic and physical properties of the fluid and do not consider the flow characteristics. For example, velocity is not considered as a parameter in the correlations that are used to compute the evaporation rate during natural convection (Al-Shammiri 2002). This could be due to the reason that the velocity was not considered to have an impact on the heat and mass transfer during natural convection. The results in the present study provide an improved understanding of the heat and mass transfer process across the air-water interface. These results suggest that the flow velocities play a crucial role in this heat and mass transport process. Therefore, it can be concluded that the correlations to estimate the heat and mass transfer during natural convection should be improved by incorporating the air and water velocities.

2.7 Conclusions

Simultaneous air and water velocity fields have been simulated using a two-dimensional VOF model. The simulations were conducted for the neutral, stable and unstable conditions. The first detailed characteristics of the coupled air-water system during natural convection are presented. The results have shown that the organized vortical motions are induced in the air and water during unstable and neutral cases, whereas, no organized motions were observed during stable case. The magnitude of air and water velocities increases as the temperature difference between air and water

increases. However, the magnitude of velocities is larger during unstable thermal stratification. During unstable thermal stratification, the RMS airside velocities are an order of magnitude higher than the RMS waterside velocities, whereas, during the stable thermal stratification, the velocity magnitudes are comparable for air and water sides. The magnitude of the air velocity changed more rapidly with the change in the bulk air-water temperature difference than the water velocity, indicating that the air velocities are more sensitive to the bulk air and water temperature difference than the water velocities. Based on the velocity data, the physical model of the heat and mass transfer across the air-water interface is defined. According to this model, the vortices on the air and water sides play an important role in enhancing the heat and mass transfer. Due to the significance of the flow velocities in the transport process, it has been proposed that the correlations for the heat and mass transfer during natural convection should be improved by incorporating the flow velocity as a parameter.

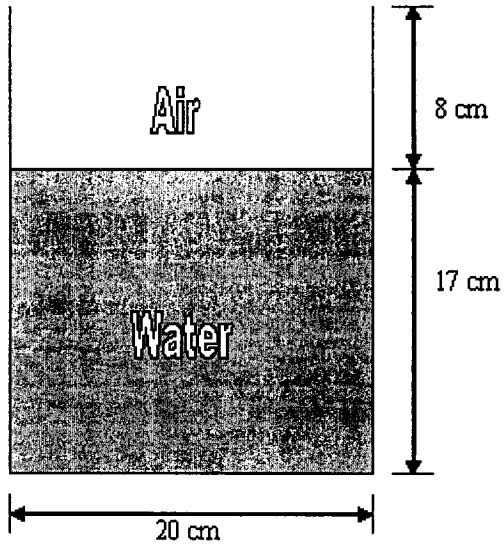

Fig. 2.1: Schematic of the Two-dimensional domain used to simulate the air and water velocity fields.

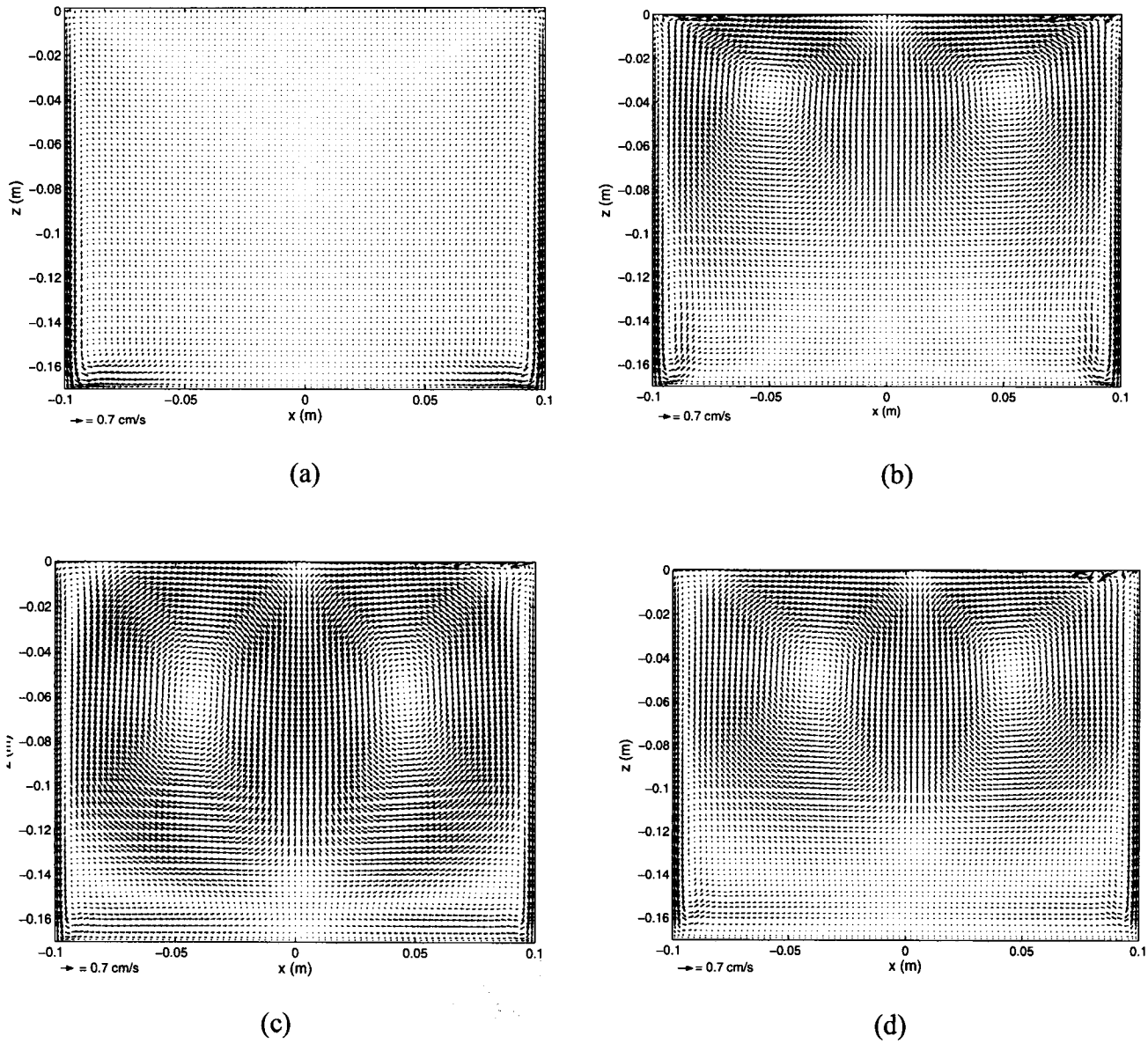

Fig. 2.2: A sequence showing the transient state of the waterside velocity fields at ΔT = 15 °C; z = distance from the air-water interface; x = distance from the mid-tank. (a) t = 20 s, (b) t = 60 s, (c) t = 100 s, (d) t = 140 s.

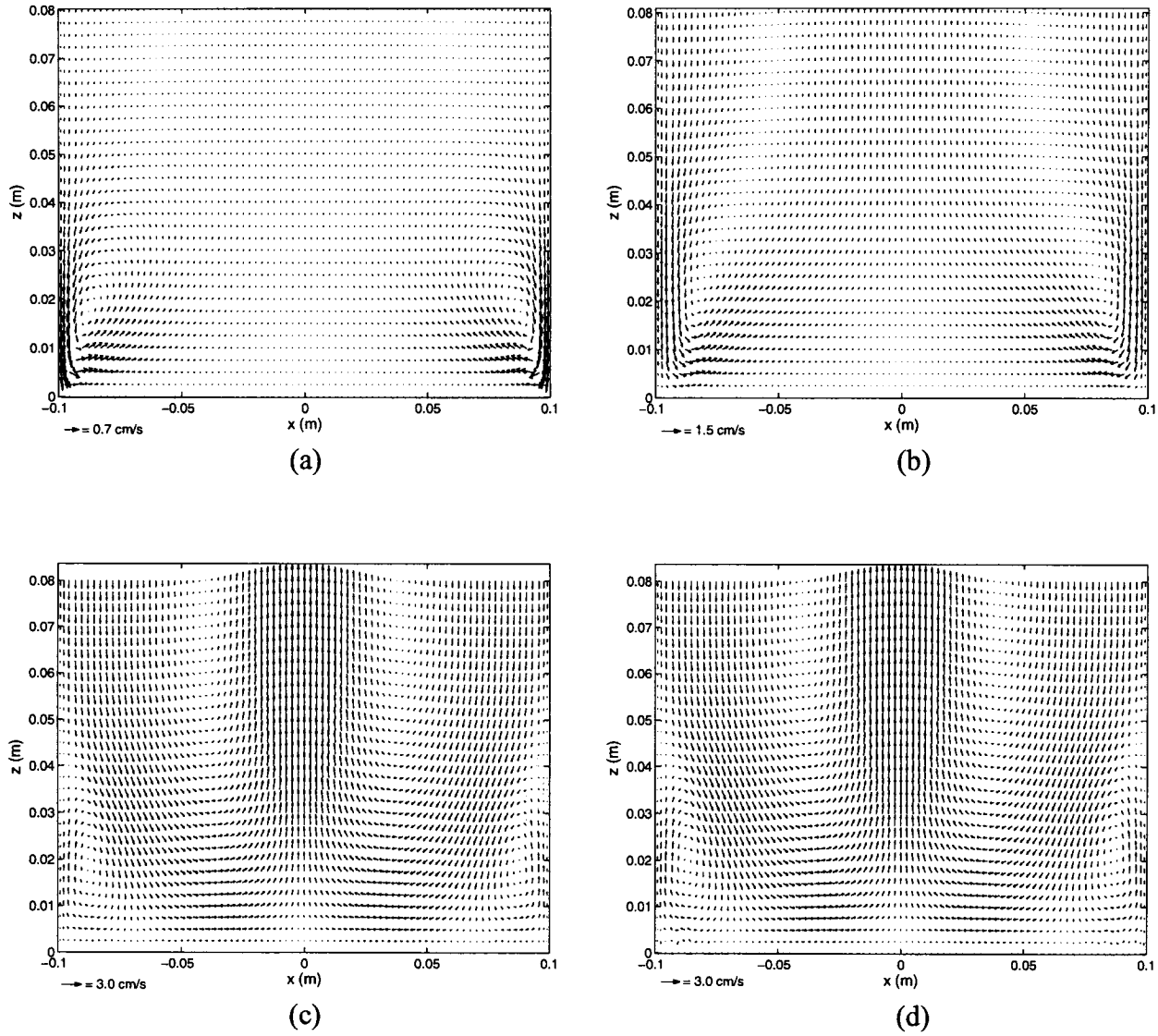

Fig. 2.3: A sequence showing the transient state of the airside velocity fields at ΔT = 15 °C; z = distance from the air-water interface; x = distance from the mid-tank. (a) t = 0.2 s, (b) t = 1.5 s , (c) t = 10 s, (d) t = 20 s.

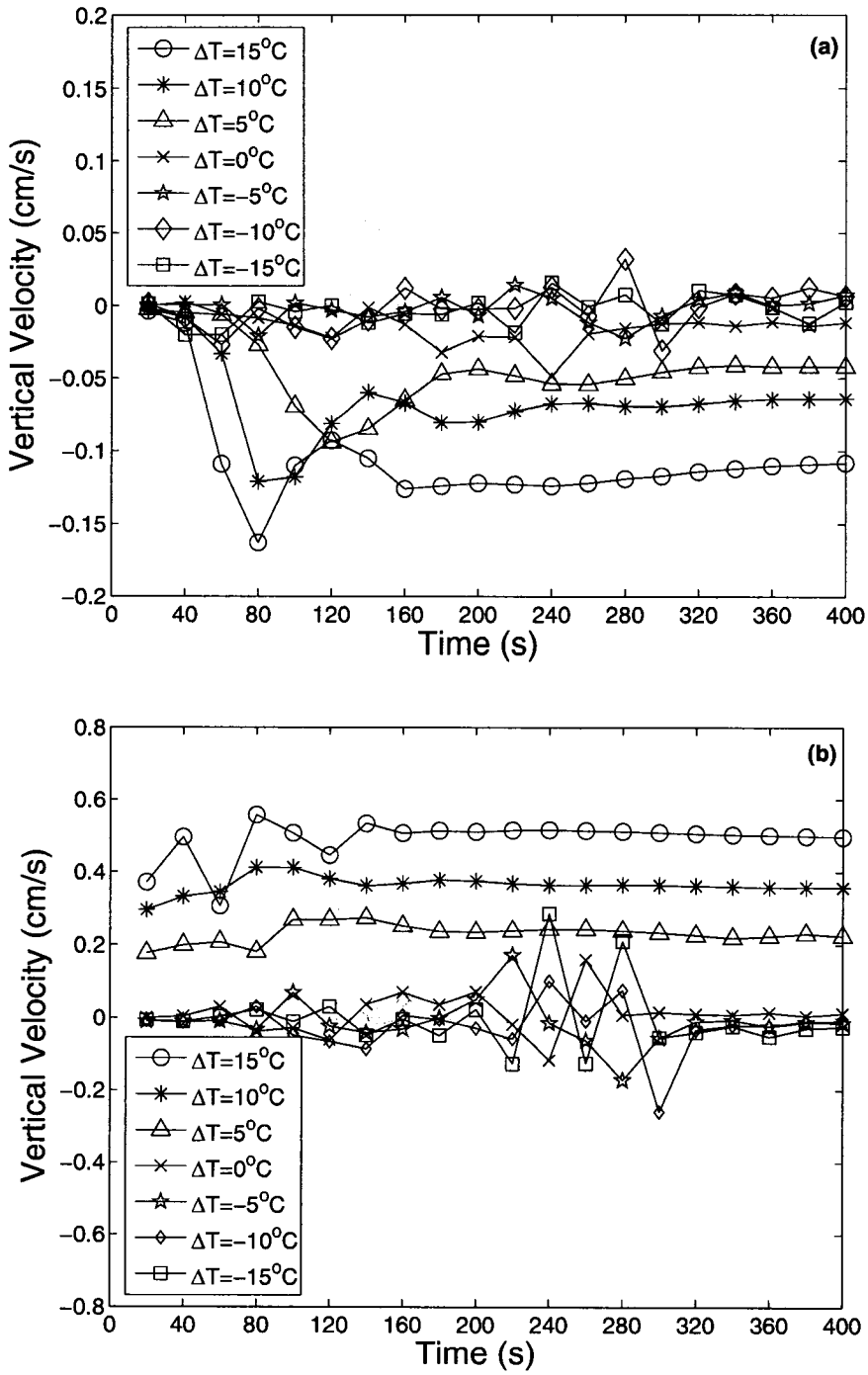

Fig. 2.4: The instantaneous vertical velocity 9 cm from the right wall as a time function. (a) Waterside, 5.5 mm below the air-water interface, (b) Airside, 5 mm above the interface.

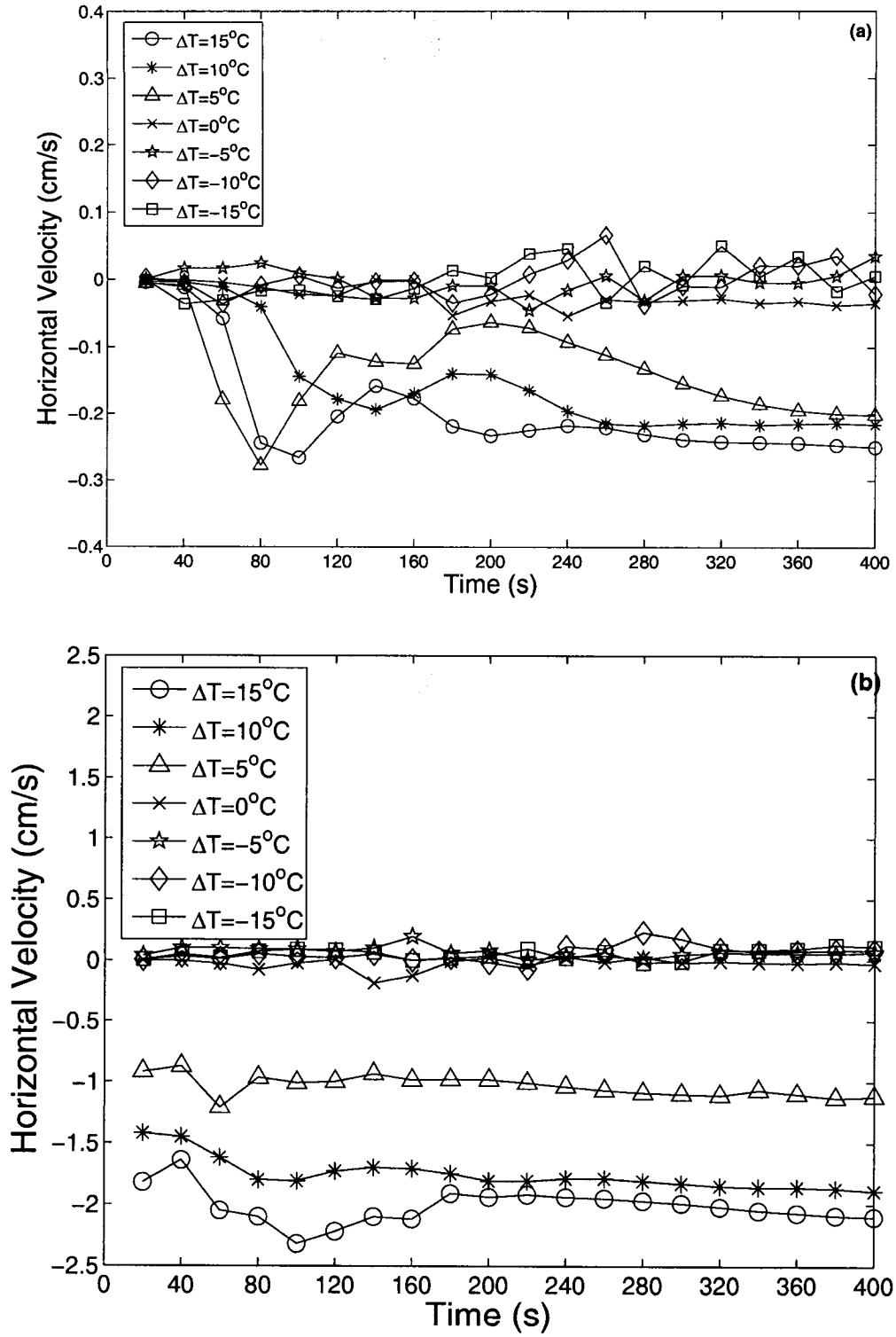

Fig. 2.5: The instantaneous horizontal velocity 9 cm from the right wall as a time function. (a) Waterside, 5.5 mm below the air-water interface, (b) Airside, 5 mm above the interface.

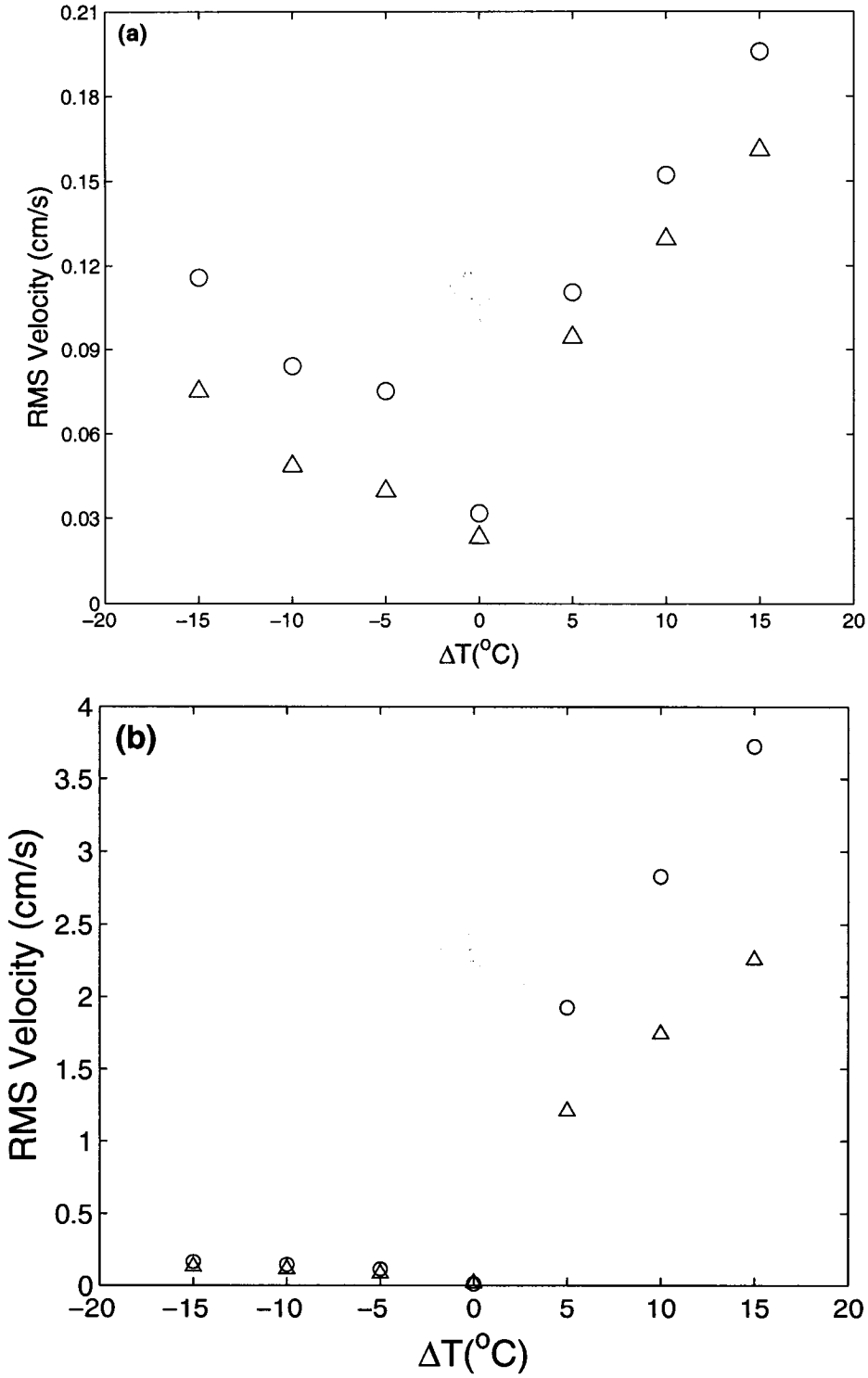

Fig. 2.6: The RMS velocities versus ΔT. (a) Water, Δ Horizontal velocity; o Vertical velocity, (b) Air, Δ Horizontal velocity; o Vertical velocity.

Chapter 3

Turbulent Structure beneath Air-Water Interface during Natural Convection

3.1 Abstract

Results from an experimental study investigating the turbulent structure beneath the air-water interface during natural convection are reported. The two-dimensional velocity field beneath the surface in a plane perpendicular to the surface was measured using digital particle image velocimetry. The results show that the waterside flow field undergoes three-dimensional flow interactions forming complex flow patterns, which appear to be random. The magnitude of the turbulent velocities and turbulent kinetic energy increases with the heat flux. The profiles of the turbulent velocities are self-similar and appropriately scaled by the parameters proposed for the natural convection above a heated wall. The wavenumber and frequency spectra exhibit -3 slopes providing the evidence that during natural convection the buoyancy subrange exists within the inertial subrange where the energy loss is due to the work against buoyancy.

3.2 Introduction

Natural convection is an important phenomenon in the coupled air-water system during which, the water surface undergoes evaporative cooling. The air and water temperatures control the evaporation rate and the sensible heat transfer across the interface. In addition, they also influence the air and water velocity fields, which in turn

alter the heat transfer rate. Thus, a better knowledge of the flow structure is important in order to improve our understanding of the physical mechanisms that control the air-water heat exchange. The heat and mass transfer across the air-water interface during natural convection is important in a wide range of applications from environmental to industrial. For example, heat and mass exchange between the ocean and atmosphere has a significant impact on the global climate. From the industrial aspect, it is important in the HVAC and chemical process applications.

The other form of the natural convection process is the one in which the fluid is bounded by a solid wall at the bottom and heated from below via this wall. The prominent examples of such type of flows are atmospheric flows in which the earth's surface acts like a rigid wall. The main difference between the two forms is the boundary condition. In the latter case, no-slip boundary condition is applied at the wall, whereas, in the former case, the air-water interface is a stress-free boundary (Flack *et al.* 2001). Due to the difference in the boundary conditions, the natural convection process particularly near the boundary could be different in both cases.

There are very few studies reported in the literature on the natural convection beneath the air-water interface. As far as we know, the only available velocity measurements beneath the water surface are by Flack *et al.* (2001) and Volino and Smith (1999). Volino and Smith (1999) simultaneously measured the surface temperature and two-dimensional sub-surface velocity fields using infrared imagery and digital particle image velocimetry (DPIV), respectively. They found that the water surface is being cooled by evaporation and the cooler water surface is plunging into the warmer bulk water below, in sheet-like plumes. The temperature field they observed was very complex

showing different scales of the thermal structures that appear to be randomly located on the water surface. They further observed that the vortices located below the water surface, pulled the cold water surface deep in to the water and simultaneously pushed the warm bulk water towards the surface. However, no strong correlation between the temperature field and the sub-surface velocity fields were observed.

Flack *et al.* (2001) measured the surface temperature of water undergoing evaporative convection using infrared imagery. The subsurface turbulence was measured using two-component laser doppler velocimetry. They conducted the experiments with two different free-surface conditions; one with a clean surface (shear free condition) and the other in the presence of a surfactant monolayer. They observed that the near-surface turbulent intensities were higher beneath the clean surface as compared to the contaminated surface and that this difference decreased with the distance from the free surface. They compared the normalized horizontal and vertical turbulent velocity profiles with the ones above a heated wall. For the clean surface, they observed maximum streamwise turbulent velocity close to the surface, which decreased with depth. They attributed this trend to the shear-free boundary condition for the evaporative convection and argued that this behavior differentiates the free surface and solid wall flows, where for the latter case, the streamwise turbulent velocity reaches zero at the wall. The magnitudes of both streamwise and vertical turbulent velocities they observed were significantly lower than that observed above the heated wall, at all depths.

Spangenberg and Rowland (1961) used Schlieren photography to study the convection currents induced by evaporation at the water surface. They observed that the cool water surface collects along lines, which causes local thickening of the surface layer

that becomes unstable and plunges into deeper water in the form of sheets. They also observed that the form of the plunging regions generated at the surface is time-dependent and changes continuously and have no fixed pattern. They found more sheets per unit area with an increase in the heat flux.

Chernous'ko (1971) studied the flow patterns at the water surface during natural convection using the powdered dye sprinkled over the surface. He observed small vortices from 1 to 3 cm in size occasionally appeared at the surface and were independent of the surface area. He found that the water temperature has an effect only on the life and number of these vortices. That is, at higher water temperature, he observed more vortices that stayed longer on the surface. He argued that the evaporative convection resulted in a cool layer of water at the air-water interface and that the temperature difference between the top layer and the water underneath depends on the evaporation rate and the range of water temperatures. He observed that the vortices were generated only when there is a relatively large temperature difference across the air-water interface.

There are many studies on the natural convection process above a heated solid wall. One of the classic papers is the review by Adrian *et al.* (1986). They proposed scaling parameters for the velocity, temperature and heat flux during natural convection based on the arguments of Townsend (1959) and Deardorff (1970). They conducted velocity and temperature measurements in a chamber in which the fluid is bounded above and below by solid walls and showed that these scaling parameters are appropriate.

The results in Flack *et al.* (2001), Volino and Smith (1999) and Spangenberg and Rowland (1961) show the complex structure at the water surface undergoing evaporative cooling. The surface temperature field is directly related to the subsurface flow. Thus,

their results indicate the existence of a complex flow structure beneath the surface. However, due to the limited work, the flow structure beneath the air-water interface is not well understood. During natural convection, the turbulence is produced mainly by the buoyancy effects. Detailed study of the turbulent flow field and its interactions is necessary in order to understand the mechanisms that control the natural convection process particularly, in the near-surface region. Similarly, the issue of the similarities and dissimilarities between the natural convection above a heated wall and that beneath a shear-free evaporative surface is not resolved. In order to address these issues, we conducted an experimental study focused on the detailed investigation of the turbulent flow structure in the near-surface region beneath the air-water interface during natural convection.

3.3 Experimental Setup

The experiments were conducted in a water tank at the Environmental Thermofluids Laboratory, in the Department of Mechanical and Industrial Engineering, Concordia University. The tank is 60 cm long, 30 cm wide and 50 cm deep. The tank was filled with clean tap water, and the water depth was maintained at 26 cm during the experiments. The bulk air temperature was maintained at 23 °C for all experiments, while the bulk water temperature was changed for each case. Three experimental cases were considered that correspond to the bulk water temperatures of 36, 30 and 23 °C. Hereinafter, these cases are referred to as case I, II and III, respectively. Cases I and II correspond to the situation when the bulk water is warmer than the air and the air and water flow fields are unstable. The heat transfer from water to air occurs via two modes; sensible heat transfer due to the bulk air-water temperature difference and latent heat

transfer due to evaporation. Thus, the cool and dense water parcels at the interface plunges into the deep water and the warm and light air parcels at the interface rise and penetrate into the cool and dense air above. Case III corresponds to the condition when bulk air and water temperatures are almost the same and the state is considered to be neutral, that is, no sensible heat transfer. The only mode of heat transfer in this case is the latent heat transfer.

The waterside two-dimensional velocity fields were measured using digital particle image velocimetry (DPIV). The measurements were made in a plane perpendicular to the water surface at the mid-tank location along the longer tank dimension (i.e. 30 cm from the end) as shown in Fig. 3.1. A Continuum Minilite 25 mJ Nd:YAG laser was used as a light source for the DPIV measurements. A CCD camera (JAI CV-M2) with the resolution of 1600 × 1200 pixels was used to image the flow. The camera was mounted in the vertical position to allow measurements to a greater depth. That is, the images were acquired with the dimensions of 1200 pixels in horizontal and 1600 pixels in vertical, with respect to the flow field. The field of view of the camera was set equal to 6.2 cm horizontal and 8.3 cm vertical. The vertical position of the camera was set in a way that the upper edge of the image coincides with the water surface. The camera was connected to a PC equipped with a frame grabber (DVR Express, IO Industries, London, ON, Canada) that acquired 8-bit images at a rate of 30 Hz. The water was seeded with silver-coated glass spheres, with the mean diameter of 15 μm (Potter Industries, Paoli, PA). These glass spheres were used as tracer particles for DPIV measurements (Appendix B). A four-channel digital delay generator (555-4C, Berkeley

Nucleonics Corporation, San Rafael CA) was used to control the timing of the laser light pulses. For each experimental run, the data was acquired for 5 minutes.

For cases I and II, the water was heated to a temperature 3 to 4 °C above the set temperature, the tracer particles were added, the water was stirred thoroughly, and then it allowed to settle down to a quasi-steady state. The data acquisition was started as soon as the bulk water temperature reached the set temperature, which typically took 45 minutes to one hour. For case III, the water at the room temperature was left in the tank for three hours. The tracer particles were then added and mixed, and the water was left undisturbed for 30 minutes to reach the quasi-steady state before the data acquisition. In all cases, the tank was remained open from the top to allow evaporation.

The total heat loss per unit area (q''_{total}) from the tank was computed by measuring the rate of decrease of the bulk water temperature that is $d\overline{T_b}/dt$ in the mid plane depth in a separate set of experiments under the conditions identical to the cases I, II and III. The data were acquired for 15 minutes for each case. The q''_{total} was computed using the relation,

$$q''_{total} = \rho \times c_p \times d \times \left(d\overline{T_b}/dt\right) \tag{3.1}$$

where, d is the depth of water in the tank and ρ is the density of water. The heat loss by conduction through the sidewalls and bottom was determined in another set of experiments under the identical conditions using the approach described in Katsaros *et al.* (1977). For these experiments, the tank was filled with water up to the top and the top was covered with the lid of the same thickness of the glass as used on the sidewalls and bottom. The rate of decrease of the bulk water temperature was recorded and the heat loss

per unit area through the sidewalls, lid and bottom of the tank was computed using the following relation.

$$q''_w = \rho \times c_p \left[\frac{lbd}{2(lb + bd + ld)} \right] \frac{d\overline{T_b}}{dt} \tag{3.2}$$

where *l*, *b*, and *d* are the length, breadth and depth of the tank (Katsaros *et al.* 1977). The rate of heat loss through the sidewalls and bottom was 13%, 16% and 4% of the total heat flux for case I, II and III, respectively. The difference between the total heat loss and the heat loss through the walls was equal to the heat flux from the free surface (q''_s). The values of the total and surface heat fluxes for all cases are given in the Table 3.1.

The temperature during experiments was measured with the thermistors (TJ 72-44033, Omega Engineering, Inc.) with an accuracy of 0.1 °C. The thermistors were calibrated using Traceable Digital Thermometer (Control Company USA) which has resolution of 0.001 °C with ± 0.05 °C accuracy. The temperature data was acquired via a 16-channel data acquisition card (PCI-6036E, National Instruments) using the LabView data acquisition software.

The DPIV technique computes the velocity vectors by cross-correlating the interrogation region in the first image with the corresponding search region in the second image of an image pair. In the present study, the size of the interrogation region was set equal to 32 × 32 pixels and the size of the search region was set equal to 64 × 64 pixels. A 50% window overlap was used in order to increase the nominal resolution of the velocity field to 16 × 16 pixels. This resulted in the spatial resolution of 0.83 × 0.83 mm of the velocity field. For all cases, the velocity vectors nearest to the surface were located 1.65 mm below the air-water interface. Due to the difference in the velocity magnitudes

for all cases, a constant time separation between the two images of an image pair will give different particle shifts for different cases. That is, for small velocity magnitude the particle shift is also small. Very small particle shift increases the uncertainty in the velocity measurements (Keane and Adrian 1992). Thus, the time separation between the two images of an image pair was varied in each case, in order to obtain reasonable particle shifts (Appendix C). A scheme was used to identify the spurious velocity vectors and then correct them using a local median test (Siddiqui *et al.* 2001). Typically, 1% of the velocity vectors were spurious. The uncertainty in the velocity measurements was estimated to be less than 6% (Appendix A).

3.4 Results and Discussion

The velocity field in the plane perpendicular to the surface plays a dominant role in the natural convection process. The structure of the flow in this plane is influenced by the motion of the rising plumes of warm water and the falling parcels of the cold water. The near-surface velocity field in this plane controls the thermal boundary layer thickness at the surface and thus, the surface temperature field and the air-water heat transfer. A better knowledge about this flow field is important in order to improve our understanding of the natural convection phenomenon. To obtain a better understanding of flow structure, the two-dimensional instantaneous velocity fields obtained from the DPIV measurements were decomposed into the mean and turbulent velocity components. The mean velocity field was obtained by time-averaging the data at each grid point. The turbulent velocity field was obtained by subtracting the mean velocity from each instantaneous velocity field. The results have shown that the turbulent velocity field varies temporally and spatially, which creates a complex pattern of the velocity field in

the vertical plane. Some sample turbulent velocity fields of case I (i.e. highest heat flux case) are presented in Fig. 3.2 that provide a good perception of the complexity of the flow field.

A rising plume is visible in the right section of Fig. 3.2 (a). The plot shows that the plume rises vertically and disperses horizontally in both directions as it reaches the interface. This behavior of the plume is similar to the conceptual model of Katsaros *et al.* (1977). However, this typical behavior of the plume was rarely observed in the entire dataset. The middle and left sections of the plot show that small pockets of fluid with negligible velocity in the measurement plane obstruct the flow and force it to move around the pocket. One such pocket is located in the middle of the plot which forced the rising fluid from underneath to go around it. Another pocket is located near the interface which forced the fluid to change its direction. As the flow field inside the tank is three-dimensional, it is likely that these pockets are the flow streams in the direction perpendicular to the measurements plane. Thus, the interaction of the three-dimensional flow forms very complex flow patterns. The detailed analysis of the velocity field revealed that these flow patterns persist for relatively long durations before they get distorted. It was also observed that these flow interactions create local vortices. These vortices are observed at all depths and their shape varied from circular to stretched depending on the flow interaction. These vortices enhance local mixing. The schlieren images of the flow in the vertical plane (Fig. 3, Spangenberg and Rowland 1961) also showed the spatial variations of the falling sheets. The pattern they observed was quite similar to the flow patterns observed in the upper left portion of Fig. 3.2 (a). Their results also show that the falling sheets are not necessarily vertical even in the close vicinity of

the free surface. Adrian *et al.* (1986) also observed through visualization of the flow above a heated wall that the thermal plumes originated from the bottom wall were not always vertical. They found a deviation as large as 60 degree from the vertical. This indicates that the dynamics of the falling sheets and the rising plumes is controlled by the three-dimensional flow interactions.

Another interesting feature observed in the flow field is the source, which is visible in the middle of Fig. 3.2 (b). Volino and Smith (1999) also observed a source in the horizontal plane at a depth of 11 cm. They suggest that this source could be created by the falling fluid spreading in the horizontal plane. One possible explanation for the formation of the source is the interaction of the two fluid streams opposite in direction. Thus, the formation of a source in the horizontal plane could be due to the interaction of the falling sheet and the rising plume. The source that is observed in the vertical plane in Fig. 3.2 (b) could not be due to the interaction of the falling sheet and the rising plume. It is likely due to the interaction of the horizontal flow streams. Fig. 3.2 (b) also indicates that the generation of a source significantly alters the flow structure. The sources were observed in the vertical plane at all depths in the given dataset.

The plots in Fig. 3.2 show that during natural convection, the waterside flow field undergoes different flow interactions locally, which result in the formation of complex flow patterns. These flow patterns in the near-surface region form complex thermal structure at the interface which was observed by Volino and Smith (1999), Flack *et al.* (2001) and Spangenberg and Rowland (1961). Due to the local interactions which appear to be random at any particular instant, these flow patterns vary significantly in both horizontal and vertical directions. This is possibly being the reason why Volino and

Smith (1999) could not find a good correlation between the thermal structure at the surface and the subsurface flow. Due to the varying nature of these interactions, it is difficult to predict the flow behavior in one region based on the flow behavior in a neighboring region, making this problem more complicated.

Analysis of the turbulent velocity fields for case II and III show that the complexity of the flow structure reduces with the decrease in the heat flux. For example, in case III (i.e. neutral case), the occurrence of the complex flow patterns was relatively low and the flow was more aligned in the horizontal and vertical directions. This indicates that the interactions of the three-dimensional flow decrease with the heat flux. It was also observed that the number of vortices in the near-surface region reduced with the decrease in the heat flux.

The average and bulk flow characteristics, however, can still provide a good insight into the overall flow behavior. The profiles of the horizontal and vertical root-mean-square (RMS) turbulent velocities as a function of depth are plotted in Fig. 3.3 (a) and 3.3 (b), respectively. Fig. 3.3 (a) shows that the horizontal turbulent velocity increased up to a depth approximately equal to 4 mm for all cases and then decreased relatively rapid to a certain depth and varied slowly afterward. Relatively large variations were observed for cases II and III. However, the variations in the horizontal turbulent velocities with depth were within 30% of their respective mean values. The profiles of the RMS vertical turbulent velocity (Fig. 3.3 (b)) show that the vertical fluctuations are very small near the surface, which increased rapidly up to a depth 2 to 3 cm from the surface and then increased slowly except for the high heat flux (case I) where it remained almost constant below a depth of 4 cm. From the surface to a depth of 3 cm, the vertical

turbulent velocity increased by factors of 3, 4 and 5.5 for cases I, II and III, respectively. At greater depths, the magnitude of the vertical turbulent fluctuations is significantly large as compared to the horizontal turbulent fluctuations due to the motion of the plumes and falling sheets.

Adrian *et al.* (1986) also observed similar trends in the turbulent velocity data above a heated solid wall. They observed a sharp increase in the RMS horizontal turbulent velocity in the layer adjacent to the wall, which followed by a slight decrease and then the velocity magnitude remained almost constant in the middle region between the two walls. The vertical turbulent velocity profile was approximately symmetric about the mid-plane, increased monotonically with distance from the wall to a certain height and then remained constant up to the mid-plane. They argued that the symmetry observed in the velocity profile is due to the symmetrical nature of the boundary conditions at the upper and lower walls. In the present case, the symmetry is expected in the vertical velocity profiles as the vertical velocity fluctuations reach zero at both upper and lower boundaries.

The vertical profiles of the turbulent kinetic energy (TKE) are plotted in Fig. 3.4 for all cases. The plot shows that as expected, the magnitude of the TKE increased with heat flux. The TKE increased by approximately a factor of two from case III to case II and by a factor of four from case III to case I. The plots also indicate that the magnitude of TKE is smallest near the surface, which increased with depth. A sharp increase in the TKE was observed in the near-surface region, which became almost constant at greater depths. The plots also show that the depth over which the TKE increased sharply, increases with the heat flux. This depth is approximately equal to 0.5, 1 and 4 cm for

cases III, II and I, respectively. The physical explanation for this behavior can be described as follows. At the water surface, the cold fluid due to evaporation accumulates in different regions (Volino and Smith 1999, Spangenberg and Rowland 1961). These cold fluid masses become unstable and form the falling sheets. These falling sheets accelerate as they plunge into deeper water due to buoyancy resulting in a sharp increase in TKE. At greater depths, the falling sheets reach an equilibrium state and the variations in TKE are small. Townsend (1976) argued that in natural convection, most of the energy transfer to the turbulent motion takes place in the region away from the wall layer, where the buoyancy forces generate energy at a uniform local rate.

The profiles in Figs. 3.3 (a) and 3.3 (b) show self-similarity. This implies that the data at different conditions could be presented by the appropriate scaling parameters. Based on the arguments of Townsend (1959) and Deardorff (1970), Adrian *et al.* (1986) proposed scaling parameters for the fluid bounded by the solid walls undergoing thermal convection when heated from below. They defined the length scale as water depth denoted by z_*, and the velocity scale is defined as,

$$w_* = (\beta g Q_o z_*)^{1/3} \tag{3.3}$$

where, β is the thermal coefficient of expansion, g is the acceleration due to gravity and Q_o is the kinematic heat flux defined as,

$$Q_o = \frac{q_s''}{\rho c_p} \tag{3.4}$$

where, q_s'' is the surface heat flux, ρ is the density and c_p is the specific heat. They argued that this scaling is applicable in the regions where the flow is dominated by convection, which covers almost the entire fluid domain except a very thin layer adjacent to the solid

wall where conduction is the primary mode of heat transfer. The values of w_* and Q_o for the three cases are presented in Table 3.1. The RMS horizontal and vertical turbulent velocities normalized by w_* are plotted in Fig. 3.5 (a) and 3.5 (b), respectively, versus the normalized depth. The data in both plots collapse into a relatively narrow band indicating that this scaling is also applicable to the flow fields undergoing evaporative cooling at the surface. Flack *et al.* (2001) compared the turbulent velocities with the solid wall cases of Adrian *et al.* (1986) and Prasad and Gonuguntla (1996). For the clean surface, they observed the maximum streamwise turbulent velocity close to the surface, which decreased with depth. They attributed this trend to the shear-free boundary condition for the evaporative convection and argued that this behavior differentiates the free surface and solid wall flows, where for the latter case, the streamwise turbulent velocity reaches zero at the wall. The magnitudes of both streamwise and vertical turbulent velocities they observed were significantly lower than that observed by Adrian *et al.* (1986) and Prasad and Gonuguntla (1996) at all depths. However, they were not able to identify the exact cause of this difference.

The data from Flack *et al.* (2001) for the clean surface (Q_o = 0.06 - 0.12 °C mm/s) and Adrian *et al.* (1986) for (Q_o = 0.153 °C mm/s) are also plotted in Fig. 3.5 for comparison. Fig. 3.5 (a) shows that the profiles of the streamwise turbulent velocity of the present study behaves similar to that for the solid wall case of Adrian *et al.* (1986). However, in the present case, the peak is observed at $z/z_* \approx 0.025$, whereas, for the solid wall, the peak is observed at $z/z_* \approx 0.05$. Furthermore, the velocity magnitude in the present study was approximately 60% lower than that for the solid wall. The plot also

shows that the present data is in reasonable agreement with that observed by Flack *et al.* (2001) in the region $z/z_* < 0.1$.

Comparison of the vertical turbulent velocity profiles (Fig. 3.5 (b)) shows that the present data and the data from Adrian *et al.* (1986) have similar trend. A detailed comparison of the data shows a good agreement in the region $z/z_* < 0.05$. In the region $z/z_* > 0.05$, the velocity magnitude of the present dataset was on average 20% lower than that of Adrian *et al.* (1986), which can be considered as within reasonable agreement based on the experimental uncertainties. The data from Flack *et al.* (2001) agreed within the region $z/z_* < 0.02$. At greater depths, their values were significantly lower then the present data. However, their trend has shown some similarities. Sorbjan (1990) proposed similarity equation for the turbulent vertical velocity component which is given by,

$$\frac{w'_{rms}}{w_*} = c_{wb}\left(\frac{z}{z_*}\right)^{1/3}\left(1-\frac{z}{z_*}\right)^{1/3} \tag{3.5}$$

where, c_{wb} is a constant. Sorbjan (1990) analyzed the data of Adrian *et al.* (1986) using the proposed scalings and set $c_{wb} = 1.05$. The data of Adrian *et al.* (1986) agreed well with the similarity predictions in the lower and middle regions and deviate in the upper region. The similarity equation is plotted in Fig. 3.5 (b) for $c_{wb} = 0.85$. The plot shows a good agreement between the similarity equation and the present data, however, the constant c_{wb} is lower than that for the solid wall case.

The analysis of Figs. 3.5 (a) and 3.5 (b) show that the turbulent velocity field beneath the shear-free interface undergoing evaporative cooling has a trend similar to that observed above a heated wall. The magnitudes of the vertical turbulent velocity in both cases were comparable but the magnitude of the horizontal turbulent velocity above a heated wall is larger than that below a shear-free surface. The boundary condition for the

vertical turbulent velocity is the same for both cases, that is, the vertical fluctuations reach zero at the boundary. But the boundary condition for the horizontal turbulent velocity is different for both cases that is, horizontal fluctuations reach zero only at the solid wall. Thus, one possible explanation for the difference in magnitude of the horizontal turbulent velocity is the difference in the boundary condition as pointed out by Flack *et al.* (2001). How the boundary condition alters the turbulent velocity magnitude needs detailed investigation of the turbulent kinetic energy budget, which is beyond the scope of the present paper. Nonetheless, the results in Fig. 3.5 indicate that the turbulent structure of the flow beneath the water surface undergoing evaporative convection is similar to that observed in the near-surface region above a heated wall.

In order to obtain a detailed structure of the turbulent flow beneath the water surface during natural convection, it is important to investigate the turbulent scales responsible for the transport of heat. The spectral analysis provides information about the time and spatial scales of the turbulent motions. The wavenumber spectra of the horizontal and vertical turbulent velocities were computed for all cases. The one-dimensional wavenumber spectrum was computed in the horizontal direction at all depths in each velocity field and then averaged at each depth. The normalized wavenumber spectra of the horizontal and vertical turbulent velocities for case I at three different depths (0.25, 3.6 and 6.9 cm) are plotted in Fig. 3.6 (a) and 3.6 (b), respectively. The spectra of both velocities show that the scales of the energetic turbulent motions are smaller than 120 rad/m. This correspond to the size greater than 5 cm. Due to relatively small field of view (6.2 cm in horizontal), we were not able to resolve larger scales of turbulent eddies. However, the peaks in the vertical velocity spectra (Fig. 3.6 (b)) appear

at $k \approx 120$ rad/m, which indicate that the range of larger eddies is fairly well resolved in the present case. In conventional turbulent flows, the energy-containing eddies extract energy from the mean flow. This energy is then transferred via energy cascade and dissipated to heat at Kolmogorov scales. At wavenumbers higher than that of the energy containing eddies, the inertial subrange exists where the energy transfer depends only on the energy dissipation rate and the wavenumber spectrum exhibits a slope of –5/3 (Hinze 1975). Turner (1973) argued that in a stratified fluid over a certain range of wavenumbers, the turbulent kinetic energy can be removed by working against the buoyancy forces. Based on this argument, he proposed a range of wavenumbers within the inertial subrange termed as "buoyancy subrange" where the energy loss is due to the work against buoyancy. Based on the dimensional arguments he suggested that in the buoyancy subrange, the energy transfer depends only on the buoyancy frequency (which is a function of the vertical density gradient) and the wavenumber, and is independent of the energy dissipation rate. He further argued that due to the additional source of energy removal, the energy transfer rate in the buoyancy subrange is larger than the energy dissipation rate and is proportional to k^{-3}. That is, the wavenumber spectrum exhibits a slope of -3 in the buoyancy subrange. The spectra in Fig. 3.6 show the existence of the inertial subrange at higher wavenumbers ($k > 900$ rad/m). The spectra also show the existence of the buoyancy subrange at wavenumbers $200 < k < 800$ rad/m except for the wavenumber spectrum of the vertical turbulent velocity at a depth of 2 mm. Fig. 3.6 (a) shows that the wavenumber spectra of the horizontal turbulent velocity exhibit similar behavior at different depths and have comparable magnitude. However, Fig. 3.6 (b) shows that near the surface, the buoyancy subrange does not exist in the wavenumber

spectra of the vertical turbulent velocity and the turbulent motions are relatively weaker than the ones at greater depths. The plot also shows that as the depth increases, the turbulent motions become stronger and the buoyancy subrange is manifested. Thus, it can be argued that the vertical turbulent motions near the surface are weak and therefore, could not work against the buoyancy forces. Turner (1973) argued that the removal of energy by work against buoyancy could occur only in the regions where the fluid is fully turbulent.

The wavenumber spectra of the horizontal turbulent velocity for cases I, II and III are plotted in Fig. 3.7 (a) and 3. 7 (b) at 0.25 and 6.9 cm depths, respectively. The plots show that the horizontal turbulent motions exhibit similar behavior at different air-water heat fluxes. That is, from neutral condition where the bulk air and water temperatures are approximately equal (case III), to larger unstable stratification where the bulk water temperature is higher than the bulk air temperature (case I), the scales of horizontal motion that are responsible for energy extraction and interaction with the buoyancy forces, are almost identical. In other words, it could be argued that the change in heat flux across the air-water interface changes the magnitude of the horizontal turbulent motions but the scales involved in different interactions are within the same range.

The wavenumber spectra of the vertical turbulent velocity for cases I, II and III at depths of 0.25 and 6.9 cm are plotted in Fig. 3.8 (a) and 3.8 (b), respectively. The spectra in Fig. 3.8 (b) show a trend similar to Fig. 3.7, that is, the scales of vertical turbulent motions involved in different interactions are similar at different heat fluxes. However, in the near-surface region (Fig. 3.8 (a)), the shape of the spectrum changes with heat flux. For the lower heat fluxes (cases II and III), the buoyancy subrange exists in the spectra,

that is, the vertical turbulent motions interact with the buoyancy forces. However, as the heat flux increases, the buoyancy subrange disappears. This behavior can be described as follows. Due to the boundary condition, the vertical velocity fluctuations must be zero at the air-water interface and their magnitude increases with depth. A significant difference in the velocity magnitude is observed at greater depths for different heat fluxes. For example, at a depth of 3 cm, the RMS vertical velocity increased by 0.12 cm/s from case III to case I. However, in the near-surface region, the relative difference in the velocity magnitudes for different heat fluxes is not large. For example, at a depth of 0.25 cm, the RMS vertical velocity increased by only 0.04 cm/s from case III to case I (see Fig. 3.3 (b)). For the low heat flux case, the buoyancy forces are relatively small and the vertical turbulent motions in the near-surface region are strong enough to work against the buoyancy forces. However, as the heat flux increases, the magnitude of the buoyancy force increases significantly, but the magnitude of the vertical turbulent motions does not increase accordingly. As a result, they become relatively weaker with respect to the buoyancy force. Therefore, at the high heat flux (case I), the vertical turbulent motions in the near-surface region are not strong enough to work against the buoyancy forces. The plot also shows that in the near-surface region, the scale of the energetic vertical turbulent motions decreases with the heat flux.

The frequency spectra were computed from the time series of the turbulent velocities extracted at every spatial grid point. The spectra were then averaged at each depth. The normalized frequency spectra of the horizontal and vertical turbulent velocities for case I at three different depths (0.25, 3.6 and 6.9 cm) are plotted in Fig. 3.9 (a) and 3.9 (b), respectively. The spectra in both figures show similar behavior

(except for the vertical velocity spectrum at 0.25 cm depth). That is, the timescales of the energetic turbulent motions are greater than 17 sec. The buoyancy subrange exists in the spectra at all depths. Near the surface, the buoyancy subrange exists in the frequency range $0.06 < f < 0.3$ Hz, which corresponds to the timescales of approximately 17 sec to 3.3 sec. At greater depths, the buoyancy subrange is relatively larger and covers the frequency range $0.06 < f < 0.6$ Hz, which corresponds to the timescales of approximately 17 sec to 1.7 sec. The vertical velocity spectrum in Fig. 3.9 (b) at a depth of 0.25 cm shows the inertial subrange but no buoyancy subrange. The argument similar to that for the corresponding wavenumber spectra can be used here. That is, vertical turbulent motions in the near-surface region are not strong enough to work against the buoyancy. The plots in Fig. 3.9 show that unlike the wavenumber spectra, the frequency spectra exhibit a slope of approximately -1/2 following the buoyancy subrange. One possible explanation for this trend could be that the buoyancy subrange covered the entire inertial subrange. The frequency range that exhibits $-1/2$ slope implies that the energy transfer at these timescales is relatively slow. This indicates that at these timescales, the viscosity and dissipation rate are not the controlling parameters for the energy transfer. Furthermore, the turbulent motions do not interact with the buoyancy forces. A plausible explanation for this trend is that at these timescales, the turbulent motions are too weak to interact and work against the buoyancy forces and are simply convected by the buoyancy forces. The horizontal velocity spectra at all depths also show a prominent peak at 3.5 Hz. No such peak is manifested in the vertical velocity spectra. This indicates that the energy is transferred to the horizontal turbulent motions at very small timescales. The physical explanation for this peak is not known and the issue is currently under investigation.

The frequency spectra of the horizontal turbulent velocity at depths of 0.25 and 6.9 cm for cases I, II and III are plotted in Fig. 3.10 (a) and 3.10 (b), respectively. The spectra at different heat fluxes show similar trend. However, the buoyancy subrange is relatively short at the low heat flux. The frequency spectra of the vertical turbulent velocity at depths of 0.25 and 6.9 cm for cases I, II and III are plotted in Fig. 3.11 (a) and 3.11 (b), respectively. The plot shows that at greater depth, similar timescales of the vertical turbulent motions are observed at different heat fluxes. However, in the near-surface region, at high heat flux, the buoyancy subrange does not exist in the spectrum. The plausible explanation for this trend is the same as described for the corresponding wavenumber spectrum.

Based on the results in Figs. 3.6 to 3.11, the physical mechanism of the energy interactions beneath an air-water interface during natural convection can be described as follows. The large-scale motions greater than 5 cm extract energy for the turbulence. These large-scale motions are relatively slow with the timescales greater than about 17 sec. The size of the large-scale thermal signatures observed in the water surface temperature field by Volino and Smith (1999) are comparable to the size of these large-scale turbulent motions, which further support our results and indicate that the large-scale thermal signatures at the surface are produced by large-scale horizontal turbulent motions. At intermediate scales (3 - 0.75 cm) the turbulent motions interact with the buoyancy forces resulted in a rapid loss of the turbulent kinetic energy that is exhibited by the slope of -3. The timescale of these turbulent motions is in the range 1.7 to 11 sec. The comparable scales are also evident in the temperature field of Volino and Smith (1999). At smaller scales (< 0.7 cm), the inertial subrange exists and the energy transfer

exhibits the conventional trend. The velocity field in Fig. 3.2 (a) shows large-scale turbulent motion in the lower half and intermediate-scale turbulent motion in the upper middle and left sections.

The frequency spectra show different trend in the frequency range higher than the buoyancy subrange. The frequency spectra show that in this range, that correspond to the timescale range of 0.3 to 1.7 sec, the energy transfer is very slow (the slope is -1/2), which suggests that at these timescales, the turbulent motions are convected by the buoyancy forces. However, no such trend is observed in the wavenumber spectra. A possible explanation is that in the frequency spectra, the buoyancy subrange covers the entire inertial subrange (compare frequency spectra of the vertical velocity at different depths in Fig. 3.9 (b), which is followed by the $-1/2$ slope range. The wavenumber spectra in the plots do not extend beyond the inertial subrange thus, $-1/2$ slope may exist at higher wavenumbers, which cannot be resolved with the given dataset. The results from the spectral analysis also indicate that the turbulent motions must be strong to interact with the buoyancy forces otherwise, the turbulent energy transfer follows the convectional mechanism as evident in the near-surface vertical velocity spectra at high heat flux (Fig. 3.6 (b) and 3.9 (b)).

3.5 Conclusions

Results from an experimental study investigating the turbulent structure beneath the air-water interface during natural convection are reported. The results show that the waterside flow field undergoes three-dimensional flow interactions forming complex flow patterns, which appear to be random and typically persist for long durations. These complex flow patterns in the near-surface region form the complex thermal structure at

the interface observed in the previous studies. The magnitude of the turbulent velocities and turbulent kinetic energy increases with the heat flux. The variations in the horizontal turbulent velocity with depth are relatively small, but the vertical turbulent velocity increased with depth in the near-surface region. The profiles of the turbulent velocities are self-similar and appropriately scaled by the parameters proposed for the natural convection above a heated wall, indicating that this scaling is also applicable to the natural convection beneath evaporative water surface. The wavenumber and frequency spectra exhibit -3 slopes providing the evidence that during natural convection the buoyancy subrange exists within the inertial subrange where the energy loss is due to the work against buoyancy. It was also observed that the range of the length scales of the turbulent motions involved in the interactions with the buoyancy forces does not vary with the heat flux. However, the range of timescales of the turbulent motion reduces with a decrease in the heat flux. The spectral analysis also indicates that the turbulent motions must be strong to interact with the buoyancy forces otherwise, the turbulent energy transfer follows the convectional energy transfer mechanism.

Case	I	II	III
q''_{total} (W/m^2)	678	367	88
q''_s (W/m^2)	591	309	85
Q_o (°C mm/s)	0.146	0.08	0.02
w_* (mm/s)	5.1	4.0	2.3
Ra^*	1.17×10^{12}	5.16×10^{11}	7.17×10^{10}

Table 3.1: q''_{total}, total heat flux; q''_s, heat flux through the water surface; Q_o, kinematic heat flux; w_*, velocity scale; Ra^*, flux-based Rayleigh number.

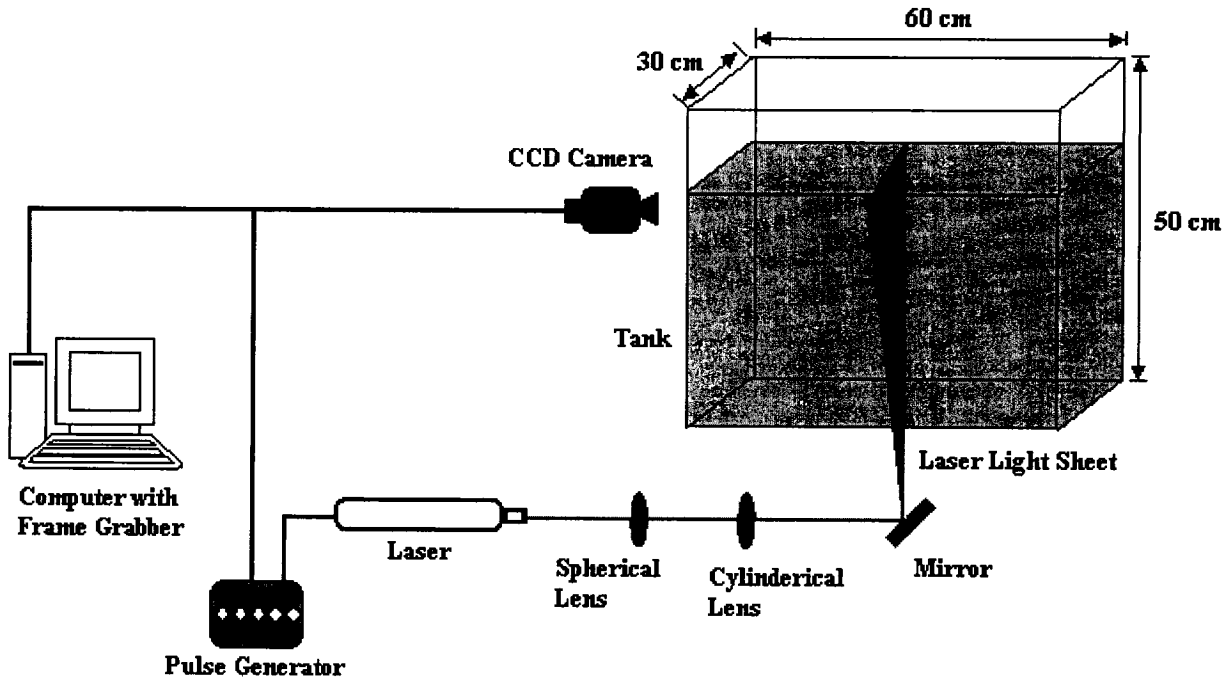

Fig. 3.1: Schematic of the experimental setup.

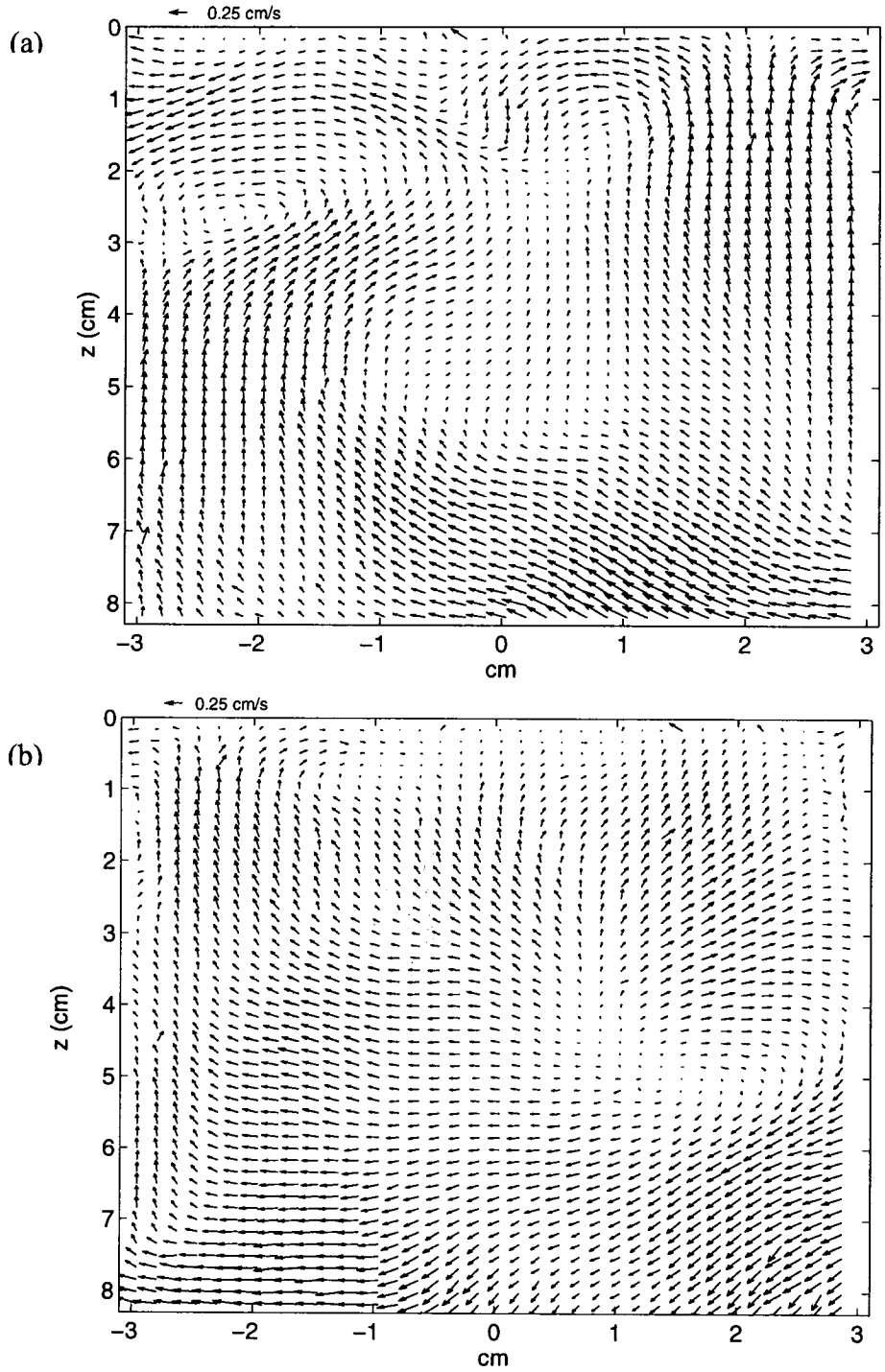

Fig. 3.2: Turbulent velocity fields at different instants of time for the high heat flux case (Case I). The depth (z) is measured from the water surface. The abscissa is the horizontal dimension and zero represents the mid-tank location.

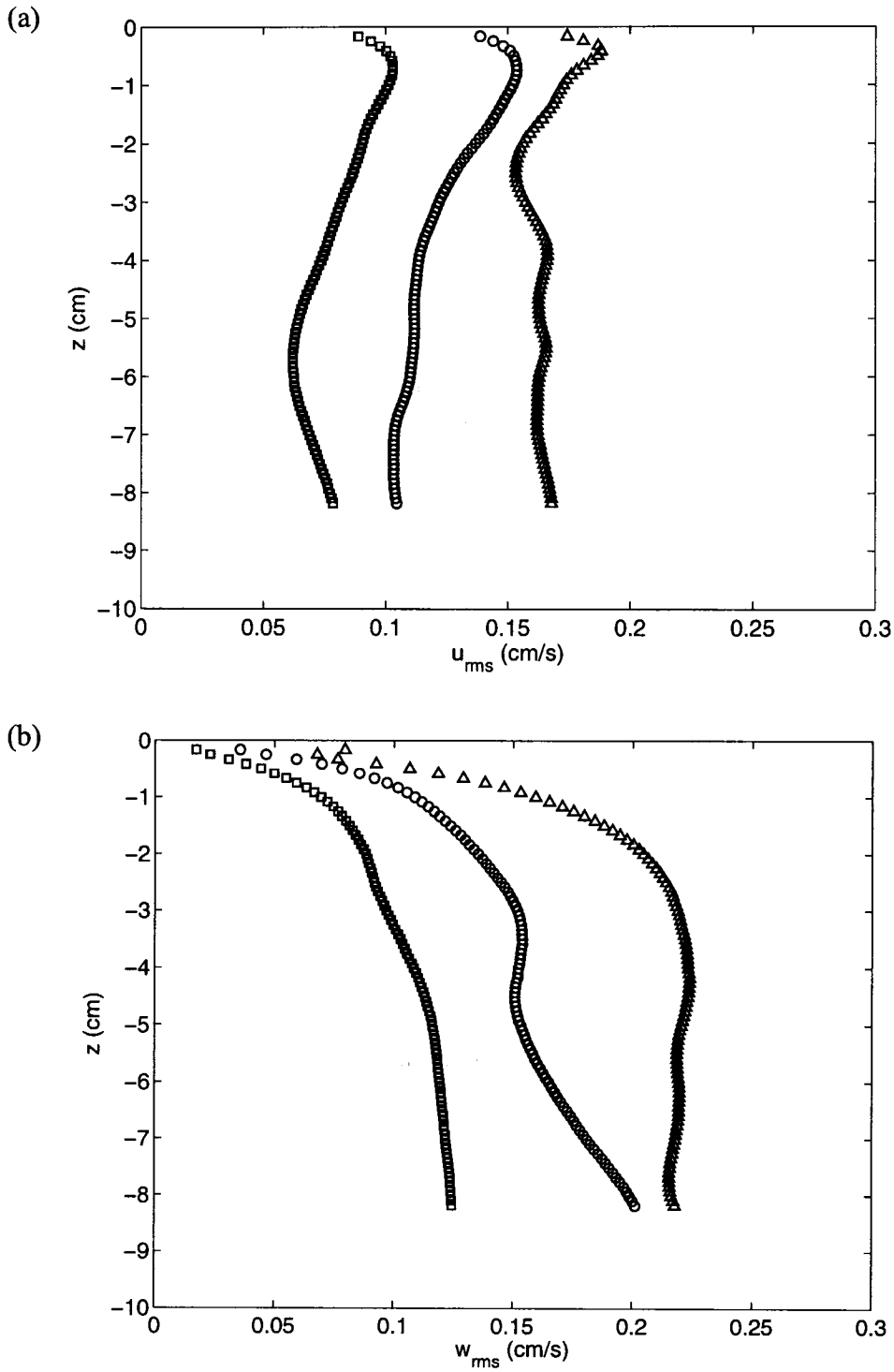

Fig. 3.3: Vertical profiles of the RMS turbulent velocities, (a) horizontal, (b) vertical. Δ, = case I; ○, = case II; □, = case III.

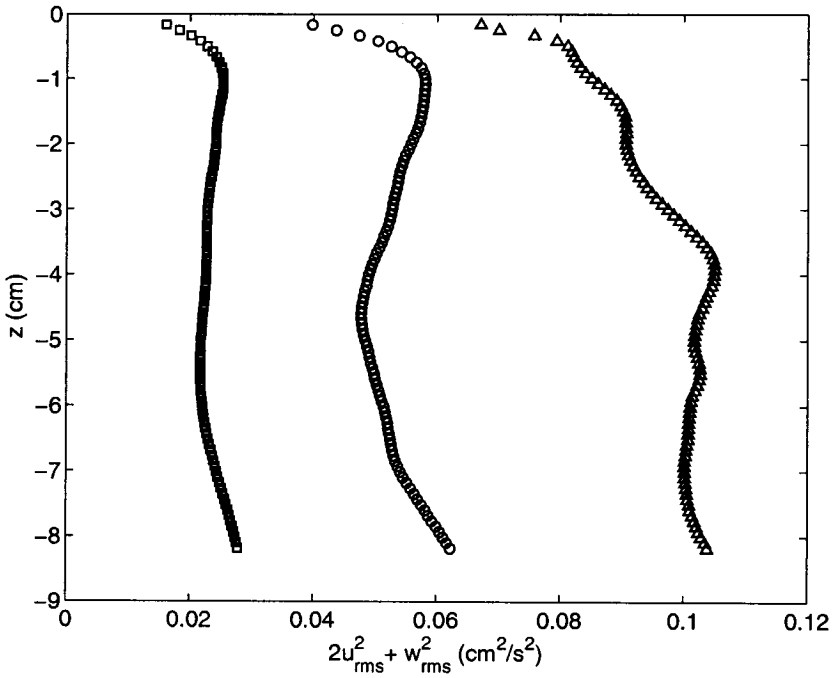

Fig. 3.4: Vertical profiles of the turbulent kinetic energy. Δ, = case I; ○, = case II; □, = case III.

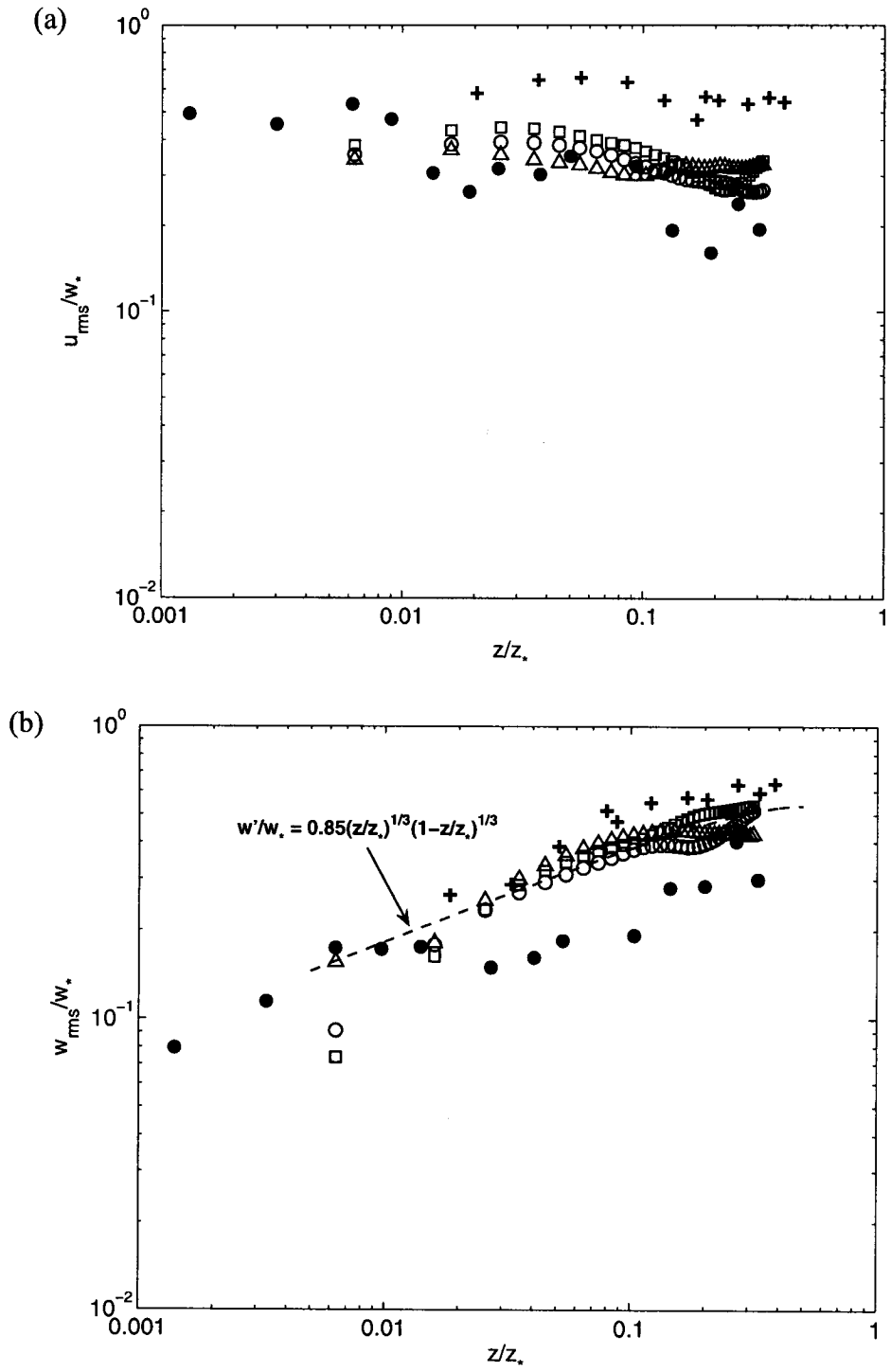

Fig. 3.5: Vertical profiles of the RMS turbulent velocities normalized by w_*. (a) horizontal, (b) vertical. Δ, = case I; ○, = case II; □, = case III; + = , Adrian *et al.* (1986); ●, = Flack *et al.* (2001).

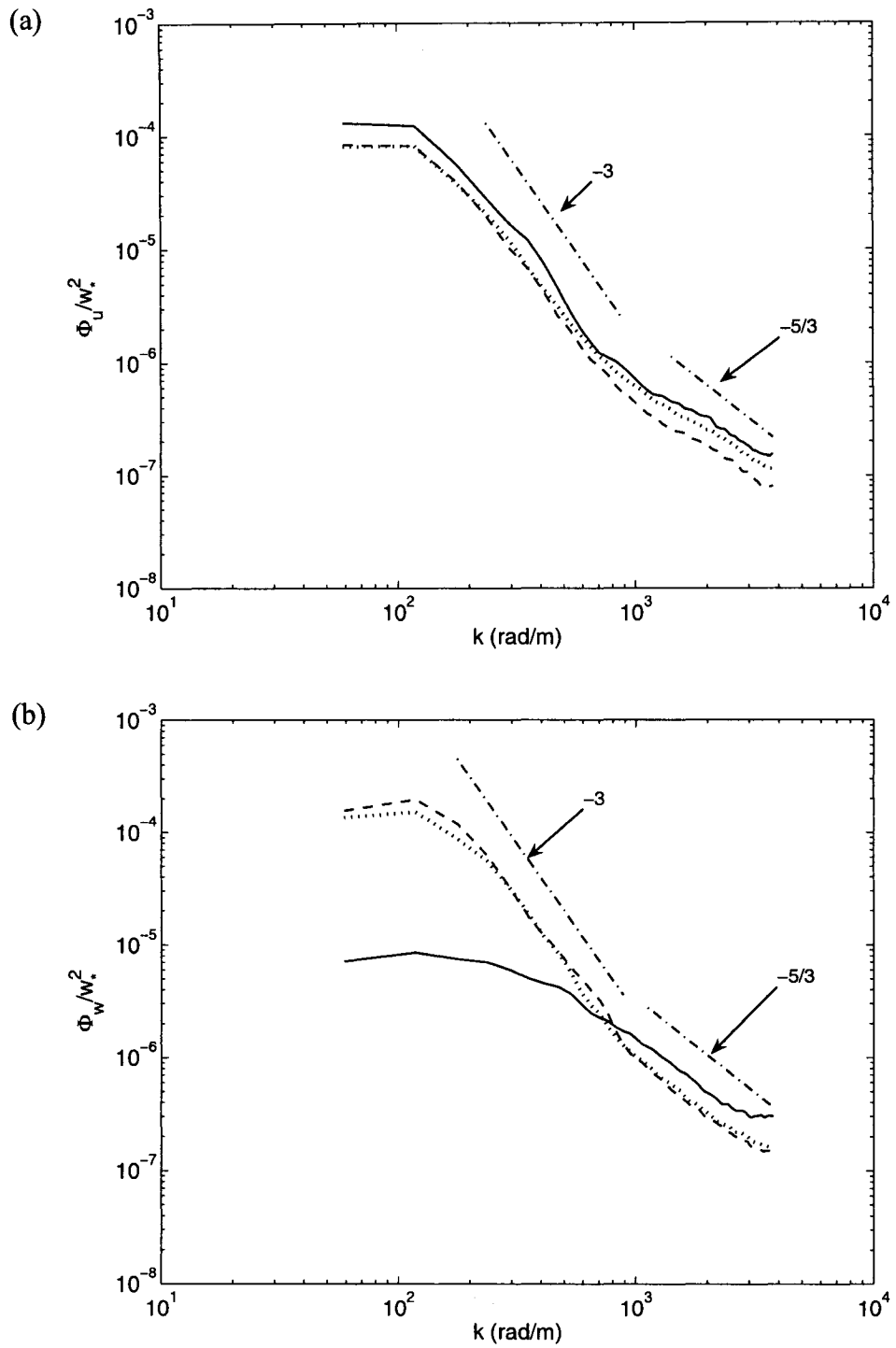

Fig. 3.6: Normalized wavenumber spectra of the turbulent velocities, (a) horizontal, (b) vertical, at high heat flux (case I) at different depths. z = 0.25 cm (solid); z = 3.6 cm (dashed); z = 6.9 cm (dotted). Dashed-dotted lines represent slopes.

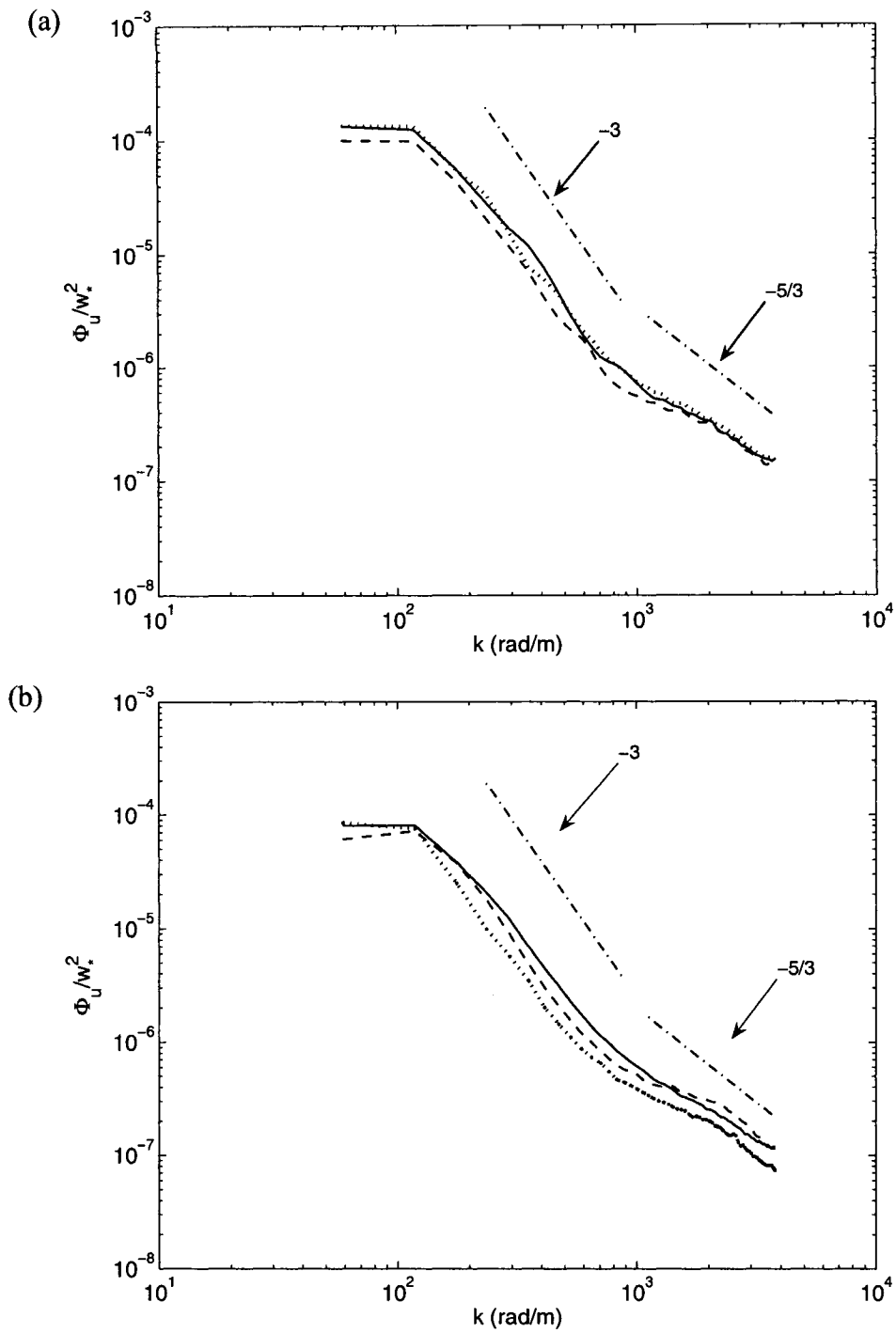

Fig. 3.7: Normalized wavenumber spectra of the turbulent horizontal velocity for different cases at depths of, (a) 0.25 cm, (b) 6.9 cm. Case I (solid); case II (dashed); case III (dotted). Dashed-dotted lines represent slopes.

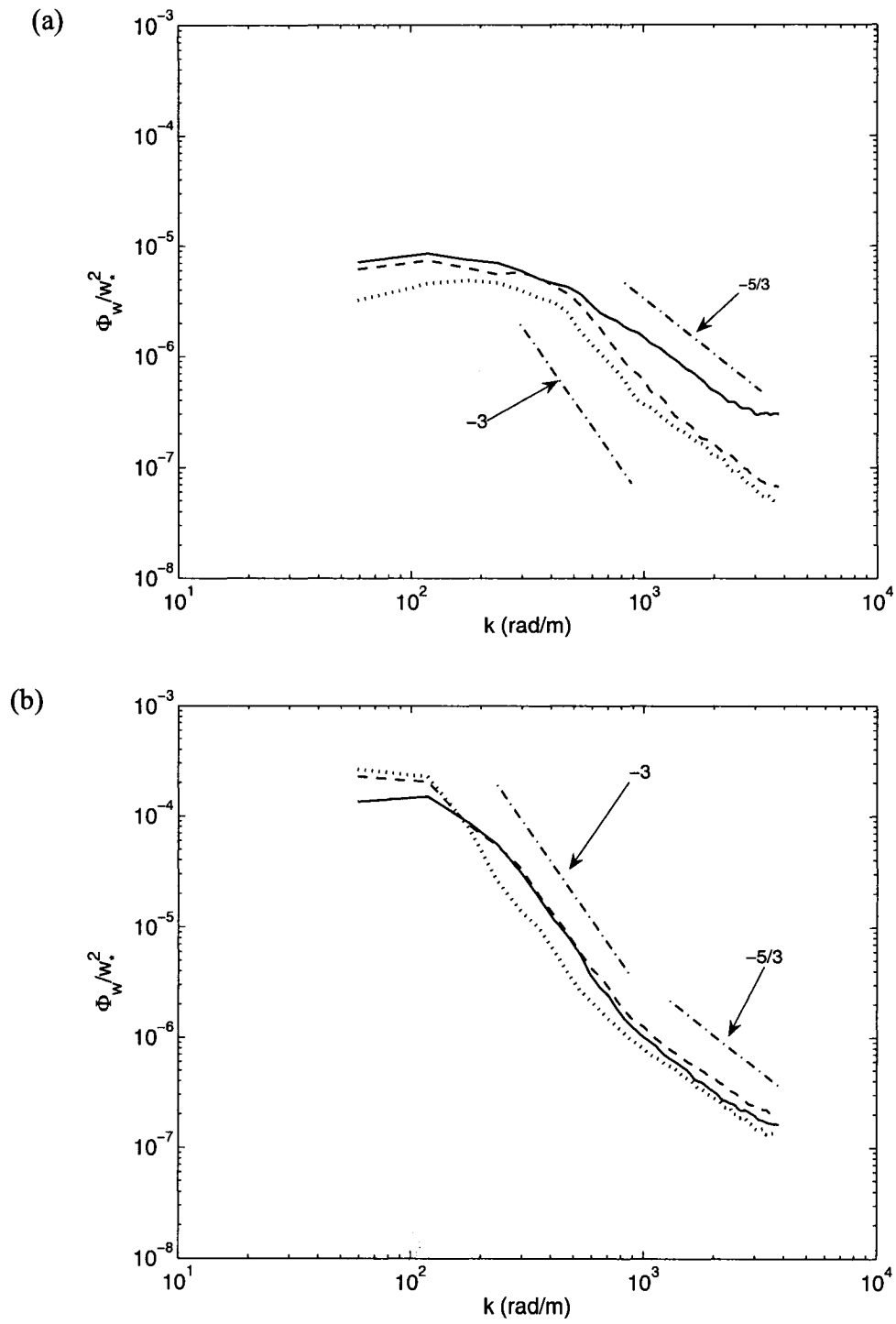

Fig. 3.8: Normalized wavenumber spectra of the turbulent vertical velocity for different cases at depths of, (a) 0.25 cm, (b) 6.9 cm. Case I (solid); case II (dashed); case III (dotted). Dashed-dotted lines represent slopes.

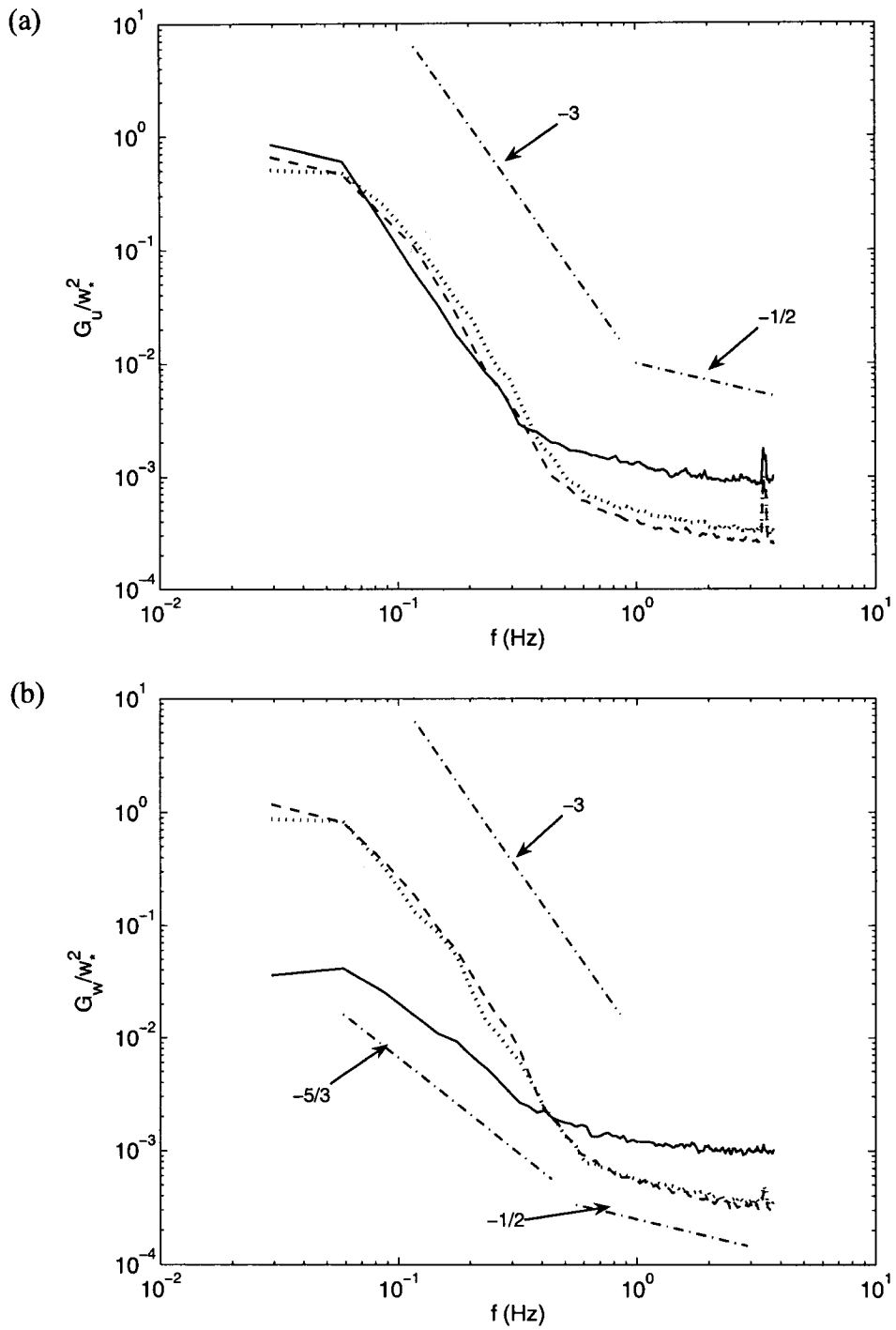

Fig. 3.9: Normalized frequency spectra of the turbulent velocities, (a) horizontal, (b) vertical, at high heat flux (case I) at different depths. z = 0.25 cm (solid); z = 3.6 cm (dashed); z = 6.9 cm (dotted). Dashed-dotted lines represent slopes.

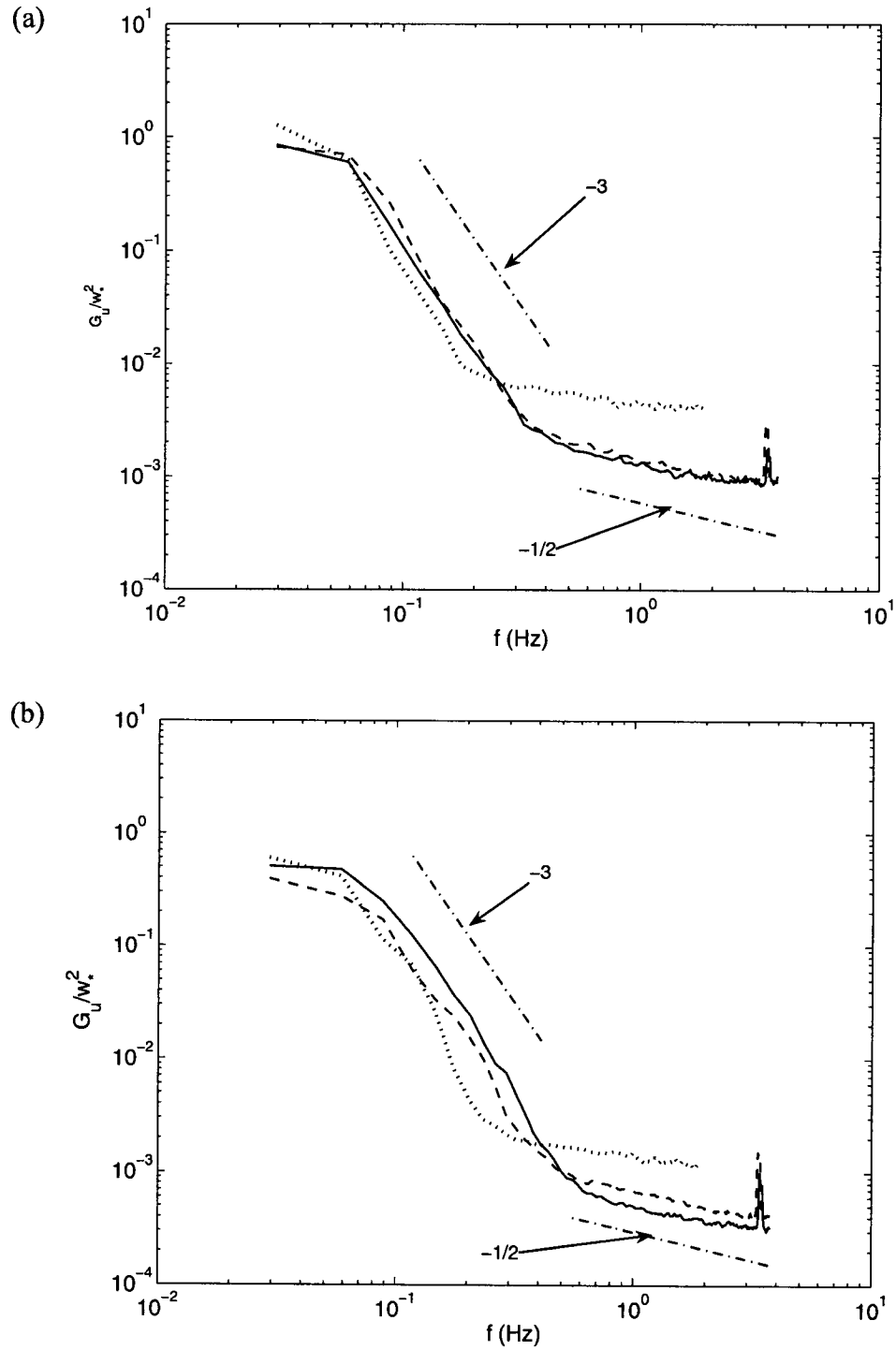

Fig. 3.10: Normalized frequency spectra of the turbulent horizontal velocity for different cases at depths of, (a) 0.25 cm, (b) 6.9 cm. Case I (solid); case II (dashed); case III (dotted). Dashed-dotted lines represent slopes.

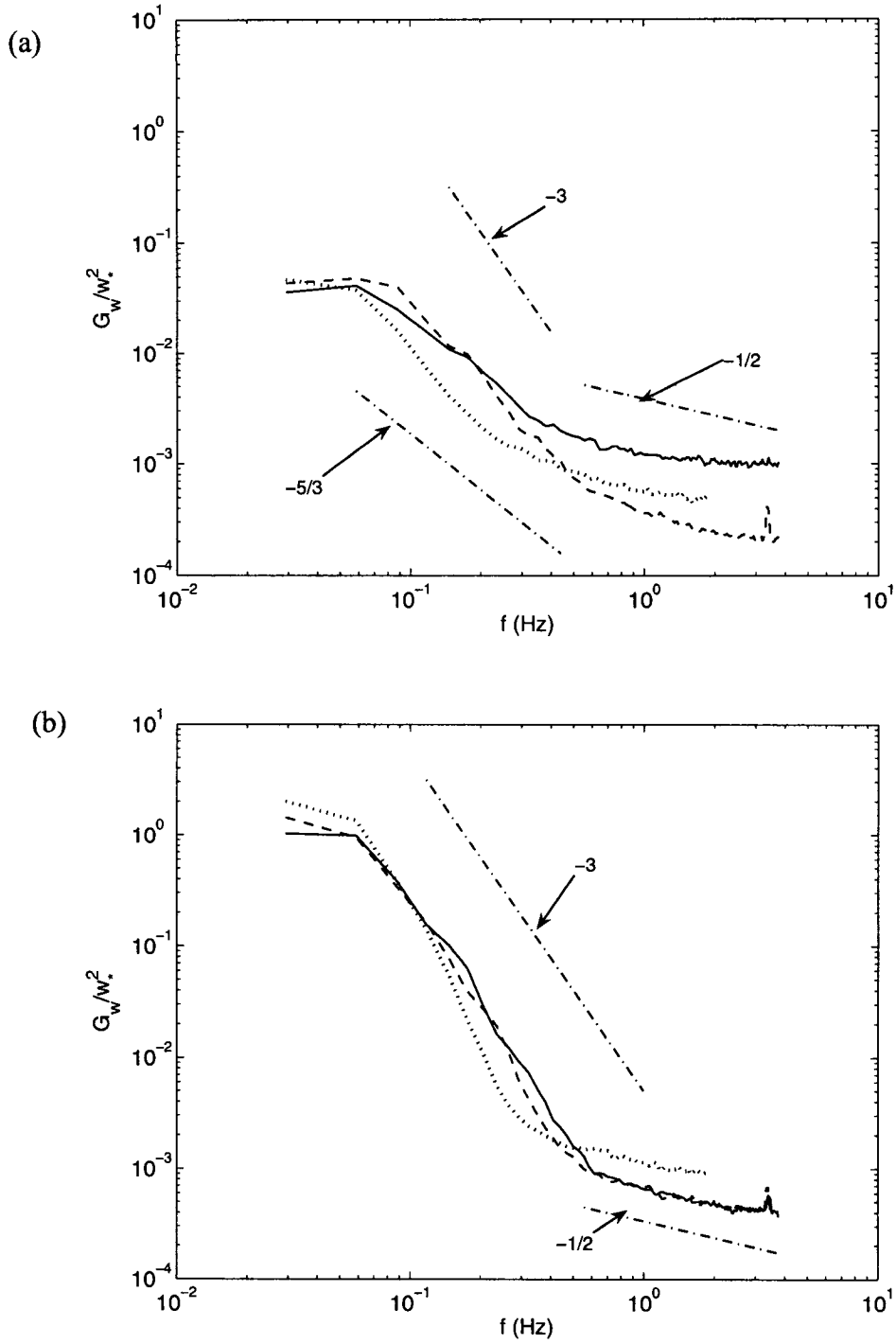

Fig. 3.11: Normalized frequency spectra of the turbulent vertical velocity for different cases at depths of, (a) 0.25 cm, (b) 6.9 cm. Case I (solid); case II (dashed); case III (dotted). Dashed-dotted lines represent slopes.

Chapter 4

The Impact of Air Saturation on the Flow Structure beneath Air-Water Interface during Natural Convection

4.1 Abstract

We report on results from an experimental study conducted to investigate the impact of air saturation on the turbulent structure beneath air-water interface. Particle image velocimetry (PIV) was used to measure the two dimensional velocity fields beneath the water surface. The results show that air saturation has a significant impact on the waterside turbulent structure. As the air becomes saturated, the magnitudes of the horizontal and vertical turbulent velocities are decreased by factors of 5 and 2.5, respectively. It was argued that in addition to the surface heat flux, the waterside flow field is also influenced by the airside velocity via the air-water interface. The latent heat flux at the saturation state is not equal to zero. The film condensation on the tank walls at the saturation state is found to be responsible for the latent heat flux. The spectral analysis shows that both the horizontal and vertical turbulent motions are much weaker than that for the unsaturated case. For the saturated case, the range of the turbulent motions responsible for working against buoyancy forces is smaller than that for the unsaturated case. It was concluded that during natural convection, when the turbulence is relatively weak, in addition to the buoyancy subrange, another subrange exists within the inertial subrange, where the turbulent motions are simply convected by the buoyancy

forces and that the energy interaction is highly dependent on the energy of the turbulent motions and the magnitude of the buoyancy forces.

4.2 Introduction

Natural convection plays an important role in many engineering and environmental applications. It is a process during which the mass and heat exchange between air and water takes place without any external influence. The natural convection process in an air-water system is significantly influenced by the evaporation at the interface. The evaporation causes the latent heat transfer from the water surface which results in the formation of a cool water layer at the interface. This cool and dense water layer becomes unstable and falls through the warm less dense water underneath. The warmer water rises to replace the falling cold water to satisfy the mass conservation. When the bulk water is warmer than the bulk air, heat also transfers across the interface in the form of sensible heat. The natural convection process beneath the air-water interface is turbulent and the resulting velocity fields are complex (Volino and Smith 1999). Under normal conditions during natural convection when the air is not saturated, the latent heat transfer constitutes up to 90% of the heat transfer across the air-water interface (Volino and Smith 1999, Katsaros *et al.* 1977). Thus, the relative humidity on the airside plays a crucial role in controlling the bulk of the heat transfer across the air-water interface.

There are only few studies reported in the literature which investigated the flow behavior beneath the air water interface during natural convection. Bukhari and Siddiqui (2007) numerically investigated the airside and waterside flow behavior in a coupled air-water system undergoing natural convection. They simulated the flow fields for unstable

and stable thermal stratifications, and neutral condition. They found that during unstable thermal stratification, the magnitude of the root-mean-square (RMS) airside velocity is an order of magnitude higher than the RMS waterside velocity. However, for neutral and stable cases, the velocity magnitudes are comparable for air and water. They concluded that the bulk air and water temperature difference play an important role in controlling the flow fields.

Volino and Smith (1999) used infrared imagery and digital particle image velocimetry (DPIV) to measure surface temperature and sub-surface velocity field during natural convection for neutral and unstable cases. Their flux estimates showed that approximately 15% of the heat flux across the air-water interface was driven by the temperature gradient from water to air while 85% was due to evaporation from the water surface. They found that the cool water surface layer plunges into the warm bulk water in sheet like plumes. They also found that the magnitude of RMS horizontal and vertical velocities increased with the heat flux. Flack *et al.* (2001) measured surface temperature and sub-surface turbulence during evaporative convection using infrared imagery and two component laser Doppler velocimetry, respectively. They conducted experiments with water temperature 14 - 16 °C above the bulk air temperature for two different surface conditions; one with a clean surface (shear free condition) and the other in the presence of a surfactant monolayer. They observed that the near-surface turbulent intensities were higher beneath the clean surface as compared to the contaminated surface and that this difference decreased with the distance from the free surface.

Bukhari and Siddiqui (2006) experimentally investigated the turbulent structure beneath the air-water interface during natural convection using DPIV. The experiments

were conducted for three cases. Two cases correspond to the unstable thermal stratification with bulk water temperature 13 °C and 7 °C warmer than the bulk air and the third case correspond to the neutral case. Based on the analysis of the two-dimensional turbulent velocity fields they argued that during natural convection, the waterside flow field is three-dimensional that undergoes different flow interactions locally, which result in the formation of complex flow patterns. They also observed self similar behavior in the turbulent velocities for different cases and showed that the scaling parameters used for the flow above a heated solid wall are also suitable for the flow field beneath the evaporative interface. From the spectral analysis they showed that the buoyancy subrange exists within the inertial subrange when the turbulent motions are strong enough to work against the buoyancy forces. They also observed that the range of the length scales of the turbulent motions involved in the interactions with the buoyancy forces does not vary with the heat flux. However, the range of timescales of the turbulent motion reduces with a decrease in the heat flux.

All these studies were focused on the investigation of the flow characteristics when the air above the water surface is unsaturated. The typical relative humidity range in these studies was 30 to 45 %. Thus, the latent heat transfer was the dominant heat transfer mode in these studies. In some engineering and environmental applications, the air above the water surface is saturated or could reach saturation state under certain circumstances. For example, in natural-draft cooling towers used in process, HVAC or other related industries, the air above the water pool is saturated. Similarly, in nuclear power plants, any interruption in the water cooling system of the spent fuel storage bays would result in the rise of the water temperature due to decay heat of the fuel, creating

saturation condition in the air above the water pool. From environmental aspect, mixing of warmer air from the land with the relatively cool air above the water bodies such as oceans and lakes, results in an increased relative humidity which could create foggy conditions above the water surface.

In applications where the air above the water is saturated or in cases where temporary air saturation occurs, it is important to understand the impact of air-saturation on the waterside flow behavior, as the waterside turbulent velocity field has a significant impact on the flow structure and the air-water heat and mass exchange. For example, the upper ocean circulation has a significant impact on the air-sea heat exchange and the uptake of environmental gases such as CO_2 and oxygen. However, as far as the authors know, no study has reported the impact of air saturation on the flow behavior underneath the air-water interface. The present study is directed towards understanding the behavior of the waterside velocity fields when the air becomes saturated. The data for the saturated air case were acquired during the same set of experiments reported in Bukhari and Siddiqui (2006). However, Bukhari and Siddiqui (2006) reported the results for the unsaturated case only.

4.3 Experimental Setup

The experiments were conducted in a glass tank, 60 cm long, 30 cm wide and 50 cm deep. The tank was filled with clean tap water. For all experimental runs the water depth was maintained at 26 cm and the bulk air temperature was 23 ^{o}C. During the experimental runs for unsaturated air cases, the tank top was left open to allow evaporation into the room air (Bukhari and Siddiqui 2006). For the measurements under saturated conditions, the tank top was covered with a lid to reach 100% saturation inside

the tank. The present study is focused on investigating the impact of air saturation when air and water fields are unstably stratified. Therefore, for saturation study two experimental cases are considered that corresponds to the bulk water temperatures of 36 °C and 30 °C. For each case, water was heated to a temperature 3 to 4 °C above the set bulk water temperature, the tracer particles were added, the water was stirred thoroughly, and then it allowed to settle down to a quasi-steady state. The data acquisition for the unsaturated case was started as soon as the bulk water temperature reached the set temperature. Immediately after the completion of the data acquisition for the unsaturated case, the top of the tank was covered with a lid to reach the saturation state. The saturation condition inside the tank reached within one minute for the bulk water temperature of 36 °C, while it took approximately 3 minutes when the bulk water temperature was 30 °C. Measurements for the saturated cases were started five minutes after reaching the saturation state. The bulk water temperature was dropped by 0.3 and 0.2 °C between successive measurements for unsaturated and saturated cases, for the initial bulk water temperature of 36 and 30 °C, respectively. The bulk water temperatures for all cases are presented in Table 4.1. As the decrease in the bulk water temperature was small, the bulk water temperatures correspond to the unsaturated cases (i.e. 30 °C and 36 °C) are used as the reference for both saturated and unsaturated cases in the subsequent sections. Relative humidity in the tank was also measured at two different heights from the water surface using the humidity probes (HX92AV-D, Omega Engineering, Inc.) with an accuracy of ±2.5%. For both unsaturated cases, the relative humidity was varied from approximately 50% to 33% from a height of 4 cm to 15 cm above the water surface. The relative humidity of the room air was 30%.

The waterside two-dimensional velocity fields were measured using digital particle image velocimetry (DPIV). The measurements were made in a plane perpendicular to the water surface at the mid-tank location along the longer tank dimension (i.e. 30 cm from the end) as shown in Fig. 4.1. A Continuum Minilite 25 mJ Nd:YAG laser was used as a light source for the DPIV measurements. A CCD camera (JAI CV-M2) with the resolution of 1600 × 1200 pixels was used to image the flow. The camera was mounted in the vertical position to allow measurements to a greater depth. That is, the images were acquired with the dimensions of 1200 pixels in horizontal and 1600 pixels in vertical, with respect to the flow field. The field of view of the camera was set equal to 6.2 cm horizontal and 8.3 cm vertical. The vertical position of the camera was set in a way that the upper edge of the image coincides with the water surface. The camera was connected to a PC equipped with a frame grabber (DVR Express, IO Industries, London, ON, Canada) that acquired 8-bit images at a rate of 30 Hz. The water was seeded with silver-coated glass spheres, with the mean diameter of 15 μm (Potter Industries, Paoli, PA). These glass spheres were used as tracer particles for DPIV measurements (Appendix C). A four-channel digital delay generator (555-4C, Berkeley Nucleonics Corporation, San Rafael CA) was used to control the timing of the laser light pulses. For each experimental run, the data was acquired for 5 minutes.

Total heat loss per unit area (q''_{total}) from the tank was computed for both saturated and unsaturated cases in a separate set of experiments. For unsaturated case, heat loss was measured by measuring the rate of decrease of the bulk water temperature that is, $\frac{dT_b}{dt}$ in the mid plane depth for same bulk water temperatures (Bukhari and Siddiqui 2006). For saturated conditions, same procedure was adopted except that the tank top was covered

with a lid and the rate of decrease of the bulk water temperature was measured once 100% humidity level was reached inside the tank. The data were acquired for 15 minutes for each case. The q''_{total} was computed using the relation,

$$q''_{total} = \rho \times c_p \times d \times \left(\frac{dT_b}{dt} \right) \tag{4.1}$$

where, d is the depth of water in the tank and ρ is the density of water. During these experiments, the air temperature was also measured at five different heights that varied from 4 mm to 18 cm above the water surface. The heat loss by conduction through the sidewalls and bottom was determined in another set of experiments under the identical conditions using the approach described in Katsaros *et al.* (1977). For these experiments, the tank was filled with water up to the rim and the top was covered with the lid of the same thickness of the glass as used on the sidewalls and bottom. The rate of decrease of the bulk water temperature was recorded and the heat loss per unit area through the sidewalls, lid and bottom of the tank was computed using the following relation.

$$q''_w = \rho \times c_p \left[\frac{lbd}{2(lb + bd + ld)} \right] \frac{dT_b}{dt} \tag{4.2}$$

where l, b, and d are the length, breadth and depth of the tank (Katsaros *et al.* 1977). The difference between the total heat loss and the heat loss through the walls was equal to the heat flux from the free surface (q''_s).The values of the total and surface heat fluxes for both experimental conditions are given in Table 4.1. The flux based Rayleigh number was computed using the surface heat flux estimates. The values of Rayleigh number for all cases are also given in Table 4.1.

The temperature during experiments was measured with the thermistors (TJ 72-44033, Omega Engineering, Inc.) with an accuracy of 0.1 °C. The thermistors were calibrated using Traceable Digital Thermometer (Control Company USA) which has resolution of 0.001 °C with ± 0.05 °C accuracy. The temperature data was acquired via a 16-channel data acquisition card (PCI-6036E, National Instruments) using the LabView data acquisition software.

The DPIV technique computes the velocity vectors by cross-correlating the interrogation region in the first image with the corresponding search region in the second image of an image pair. In the present study, the size of the interrogation region was set equal to 32 × 32 pixels and the size of the search region was set equal to 64 × 64 pixels. A 50% window overlap was used in order to increase the nominal resolution of the velocity field to 16 × 16 pixels. This resulted in the spatial resolution of 0.83 × 0.83 mm of the velocity field. For all cases, the velocity vectors nearest to the surface were located 1.65 mm below the air-water interface. A scheme was used to identify the spurious velocity vectors and then correct them using a local median test (Siddiqui *et al.* 2001). Typically, 1% of the velocity vectors were spurious. The uncertainty in the velocity measurements was estimated to be less than 6% for the unsaturated case (Bukhari and Siddiqui 2006) and less than 9% for the saturated case (Appendix A). For each unsaturated case, 2250 velocity fields were obtained at 7.5 Hz (Bukhari and Siddiqui 2006) and for each saturated case, 1125 velocity fields were obtained at 3.75 Hz (i.e. the total sampling time of each case was five minutes).

4.4 Results and Discussion

The values of surface heat flux for saturated and unsaturated cases are tabulated in Table 4.1 for both bulk water temperatures. The results show that for the given bulk water temperature, the surface heat flux for the unsaturated case was larger than the saturated one. When the air became saturated, the surface heat flux was decreased by 43% and 50% for the bulk water temperatures of 36 °C and 30 °C, respectively. The surface heat flux constitutes both the sensible and latent fluxes. The surface sensible heat flux depends on the airside heat transfer coefficient and the surface to bulk air temperature difference. The heat transfer coefficient for air during natural convection was computed using standard correlation for the free convection from the horizontal surface (Incropera and Dewitt 2001). The air temperatures at 4 mm and 18 cm heights from the water surface were used as the reference temperatures with the assumption that the air temperature at 4 mm is approximately the same as the surface temperature. The values of the surface sensible heat flux for all cases are presented in Table 4.1. The sensible heat fluxes found to be approximately 8% to 10 % of the total surface heat flux, which is in the same range as in the previous studies (Volino and Smith 1999, Katsaros *et al.* 1977). The estimate of the latent heat flux was obtained by subtracting the surface sensible heat flux from the total surface heat flux.

Comparison of the estimated latent heat flux for saturated and unsaturated cases shows that the latent heat flux for the saturated case is approximately 40% and 50% lower than that for the unsaturated case at the bulk water temperatures of 36 °C and 30 °C, respectively. It is typically assumed that the latent heat flux is very small or negligible when the air is saturated. The above results show that in the present study, the latent heat

flux is quite significant at the saturation state. We searched through the literature but could not find any study that actually estimated the surface heat flux at the saturation condition, for comparison. The results in Table 4.1 provide the first estimation of the surface heat flux at saturation state and showed that for the present setup, it is significant. The physical explanation of the observed latent heat flux at saturation state is provided below.

For unstably stratified conditions, when the bulk water is warmer than air, there is a sensible heat transfer from water to air, in addition to the latent heat flux. For these thermally unstable conditions, when the tank top was open, due to the exchange of air masses between the tank and the surroundings by convective motion, the bulk air temperature inside the tank remained same as the room air temperature. However, for the saturated case when the lid was closed, the warmer air above the water surface was not replaced by the cool air from outside, which resulted in an increase in the air temperature inside the tank. The temperature measurements on the airside have shown that at a height of 18 cm from the water surface for saturated air conditions, the air temperature was increased by 4 ^{o}C and 2 ^{o}C compared to the room air temperature, for 36 ^{o}C and 30 ^{o}C cases, respectively. In this situation, the top lid and the side walls that bound the air acted as cold surface. The water vapors in air when came in contact with this surface, released the heat of condensation and deposited on the surface in the form of condensate film (Incropera 2006). As the vapor condensed on the top lid and side walls, the same amount of water vapor was taken up by the air from water to maintain the saturation state. This process occurred in the quasi-steady form that is, a continuous film condensation resulted in a continuous mass transfer from water to air to replenish the vapor loss from air. Thus,

a net latent heat transfer occurred from water to air, as observed in the present study. Thus, it can be concluded that the air saturation during unstably stratified conditions, resulted in a net latent heat flux transfer from water to air due to the vapor condensation at the tank boundaries.

Another factor that contributes to the latent heat transfer during saturation state is the bulk air-water temperature difference. As mentioned earlier, during unstable stratification when the water is warmer than air, there is a sensible heat transfer from water to air which resulted in an increase in the air temperature. An increase in the air temperature increases the saturation pressure of vapor in air. This allows more moisture to be added to air resulting in the latent heat transfer. The present study provided the evidence of the latent heat transfer at the saturation state. However, detailed velocity and temperature measurements on the airside during saturation state are necessary in order to improve our understanding about the heat transfer process across the air-water interface at this state.

As mentioned above, at the saturation state the temperature of air was increased by 4 °C and 2 °C for 36 °C and 30 °C cases, respectively. This resulted in a reduction in the sensible heat flux through the surface. This is evident in the surface sensible heat flux values in Table 4.1, which shows that as the air became saturated, the surface sensible heat flux was reduced by 40 - 45%.

The horizontal and vertical root-mean-square (RMS) turbulent velocities are plotted in Figs. 4.2 (a) and 4.2 (b), respectively, as a function of depth for saturated and unsaturated cases. Fig. 4.2 (a) shows that for both saturated and unsaturated cases, the variation in the horizontal velocity with depth is relatively small. For unsaturated cases,

the profiles show that the horizontal turbulent velocities increased within a depth of approximately 5 mm and then started decreasing to a certain depth after that became almost constant. The profiles for the saturated case also show a similar trend in the near-surface region. However, the increment in the horizontal velocity within 5 mm for the saturated case is relatively very small compared to the unsaturated case. Comparison of the depth-averaged velocity magnitude between the saturated and unsaturated cases shows that the horizontal turbulent velocity for unsaturated case is a factor of 5.8 and 4.6 higher than that for the saturated case at the bulk water temperatures of 30 °C and 36 °C, respectively.

The air-water interface is a shear-free boundary with the slip boundary condition for the horizontal velocity. That is, the horizontal motions exist at the water surface. The plot in Fig. 4.2 (a) shows that for the saturation case the horizontal motions immediately below the water surface are a factor of 5 and 4 smaller than that for the unsaturated case for the bulk water temperature of 30 °C and 36 °C, respectively. Bukhari and Siddiqui (2007) simulated the air and water velocity fields during natural convection. They have shown that for the bulk water temperatures of 37 °C and 32 °C, and the bulk air temperature of 22 °C, the RMS airside velocity was more than an order of magnitude larger than the waterside RMS velocity. The strong motion on the airside influences the waterside velocity field via the common boundary (i.e. the air-water interface). The strong motions on the airside increase the horizontal velocity at the common boundary. This velocity at the boundary influences the velocity field on the waterside.

On the airside, the temperature and vapor concentration differences between the surface and bulk influence the velocity field (Gebhart and Pera1971). For the unsaturated

case, as the water evaporates it diffuses upward through the air and at steady state this upward movement must be balanced by a downward diffusion of dry air so that the concentration at any height remains constant. If the air column above the water surface is wide enough, the humid air rises by natural convection through the center of the column and the dry air descends along the walls (Bejan 1993). Bukhari and Siddiqui (2007) also observed similar bulk airflow pattern from simulations. For the saturated case, the mass transfer is controlled by the film condensation simultaneously occurring at the side walls and the top lid. The airflow pattern for this case is not known, however, it is expected to be different from that for the unsaturated case and would be much more complicated. Thus, the pattern of mass diffusion on the airside in both cases would be different. The concentration gradient and surface to bulk temperature difference on the airside for the saturated case would be much lower than that for the unsaturated case. Thus, a significant reduction in the air velocity magnitude is expected at the saturation state, which causes a substantial reduction in the horizontal velocity magnitude at and beneath the water surface as observed in Fig. 4.2 (a). Thus, it can be concluded that during natural convection in a coupled air-water system, the waterside velocity field is also influenced by the airside velocity field in addition to the waterside bulk-to-surface temperature difference.

Fig. 4.2 (a) shows that for almost all cases, the shape of the profiles changes at depths greater than 3 cm. That is, the velocity magnitude decreases up to a depth of approximately 3 cm and then it remains almost constant at greater depths. As discussed earlier, the strong airside velocity field influences the waterside velocity field by inducing horizontal velocity at the boundary. For the unsaturated case, the airside horizontal

velocity is more than an order of magnitude larger than the waterside horizontal velocity (Bukhari and Siddiqui 2007). Thus, for waterside, the horizontal velocity at the interface is expected to be large. Beneath the air-water interface, the horizontal velocity field is the superposition of the horizontal velocity field due to the interface velocity and the horizontal velocity field due to the convective motion induced by the waterside bulk to surface temperature difference. As the depth increases, the horizontal velocity induced by the interface decreases. For unsaturated cases, since the magnitude of the interface induced horizontal velocity is expected to be large in the near-surface region, the overall effect is a decrease in the horizontal velocity with depth in the near-surface region. As greater depths, the horizontal velocity field due to the convective motion would be more dominant and the variation in the horizontal velocity magnitude is minimal within the given depth. For the saturated cases as discussed earlier, the air velocity magnitude would be significantly smaller and thus, the magnitude of the horizontal velocity field induced by the interface velocity would also be small and thus, the decrease in horizontal velocity within in the near-surface region is relatively small.

Fig. 4.2 (b) shows a sharp increase in the vertical component of the turbulent velocity with depth for all cases. For unsaturated cases, the plot shows that the vertical turbulent velocity increased rapidly up to a depth of approximately 3 cm and then it remains almost constant to a certain depth. For the bulk water temperature of 30 ^{o}C, the plot shows that the vertical turbulent velocity increased at greater depths. However, for the higher bulk water temperature (36 ^{o}C), it remained almost constant within the measurement depth. For the saturated cases, the plot shows that the vertical turbulent velocity increased with depth similar to the unsaturated cases, but as the depth further

increased, the magnitude of the vertical velocity tends to decrease. Comparison between saturated and unsaturated cases show that similar to the horizontal turbulent velocity, the vertical turbulent velocities are larger in magnitude for unsaturated cases for the same bulk water temperatures. In the depth range 3 - 4 cm from the water surface where the largest increase in the vertical turbulent velocity was observed, the magnitude of the vertical turbulent velocity for the unsaturated case was a factor of 2 and 2.8 higher than that for the saturated case at the bulk water temperatures of 36 °C and 30 °C, respectively. For both 36 °C and 30 °C cases, the surface heat flux was a factor of 1.9 and 2.2 higher when the air was unsaturated. High heat transfer through the surface makes the water surface layer cooler and denser which starts falling deep into the water more vigorously than that for the saturated conditions for the same bulk water temperatures. In other words, the surface to bulk temperature gradients would be larger and could exist up to greater depths. For the saturated cases, the velocity increased sharply in the near-surface region and then after a short distance it started to decrease. This change in the shape of the profiles indicates that the temperature gradient exists over relatively shorter depth. Thus, the flow accelerates over a shorter distance from the interface and then started to decelerate and the vertical convective motions become very weak. Furthermore, the horizontal velocity magnitude at the interface is also significantly different for saturated and unsaturated cases, which would also influence the vertical velocity field.

Table 4.1 shows that the surface heat flux for the saturated case at 36 °C is slightly larger than that for the unsaturated case at 30 °C. However, the magnitude of the horizontal turbulent velocity is significantly lower for the former and the vertical turbulent velocity of the former is about 30% less than the latter in 3 - 4 cm depth range.

The significant difference in the horizontal turbulent velocity magnitude is likely due to the significant reduction in the air velocity during the saturation case. The comparable magnitudes of the vertical velocity within 5 mm from the surface and the surface heat fluxes for both cases indicate that the vertical density gradients in the near-surface region could also be comparable for both cases. The decrease in the vertical velocity magnitude at greater depths for the 36 °C saturation case could be due to the reason that at greater depth the magnitude of the vertical density gradients is lower than that for the 30 °C unsaturated case. Detailed waterside temperature measurements in the vertical plane would provide better explanation for this behavior.

The comparison of plots in Figs. 4.2 (a) and 4.2 (b) shows that for all cases, in the near-surface region, the magnitude of the horizontal velocity is significantly large compared to the vertical turbulent velocity. However, away from the surface, the magnitude of the vertical turbulent velocity is larger than the horizontal turbulent velocity. This is due to the reason that in the near-surface region, the horizontal velocity is influenced by the velocity at the interface which is controlled by the airside motion and the vertical velocity approaches zero at the interface. At greater depths, the vertical turbulent velocity increases due to the strong vertical convective motion in the form of rising plumes and falling sheets (Bukhari and Siddiqui 2006, Volino and Smith 1999).

Adrian *et al.* (1986) proposed scaling parameters for the fluid bounded by the solid walls undergoing thermal convection when heated from below. They defined the length scale as water depth denoted by z_*, and the velocity scale is defined as,

$$w_* = \left(\beta g Q_o z_*\right)^{1/3} \tag{4.3}$$

where, β is the thermal coefficient of expansion, g is the acceleration due to gravity and Q_o is the kinematic heat flux defined as,

$$Q_o = \frac{q_s''}{\rho c_p} \tag{4.4}$$

where, q_s'' is the surface heat flux, ρ is the density and c_p is the specific heat. They argued that this scaling is applicable in the regions where the flow is dominated by convection, which covers almost the entire fluid domain except a very thin layer adjacent to the solid wall where conduction is the primary mode of heat transfer. Bukhari and Siddiqui (2006) showed that this scaling is also applicable to the flow beneath air-water interface undergoing evaporation when the air is unsaturated. The values of $w*$ for all cases are presented in Table 4.1. The RMS horizontal and vertical turbulent velocities normalized by $w*$ are plotted in Figs. 4.3 (a) and 4.3 (b), respectively, versus the normalized depth. For both unsaturated cases, the data collapsed into a relatively narrow band (Bukhari and Siddiqui 2006), however, for the saturated cases, the data collapsed well only in certain range. The plots show the horizontal turbulent velocity for the saturated cases collapsed reasonably well for $z/z^* < 0.1$, whereas, the vertical velocity collapsed well for $z/z^* < 0.03$ and $z/z^* > 0.2$.

The profiles in Figs. 4.2 (b) and 4.3 (b) also show that there is an increase in the vertical velocity very close to the interface (i.e. within the range $z < 5$ mm or $z/z^* < 0.02$) for all cases except the unsaturated case at 30 °C. The vertical velocity is expected to decrease as it approaches the interface due to the no-penetration boundary condition. Katsaros *et al.* (1977) proposed a model for the thermal boundary layer beneath the air-water interface during natural convection. According to this model, there is a thin layer at

the water surface where the heat is transferred due to molecular diffusion. Beneath this layer, there is another layer which they termed "Thermal source layer" that acts as a source for the cold water to produce falling sheets. They argued that within this layer the cold water is replaced by the rising warm water that results in a net upward warm advection into this region. Thus, the vertical velocity component due to the vertical advection could be relatively large in this layer. They predicted the depth of the thermal source layer to be about 1.25 mm, for surface heat flux of 210 W/m^2. Thus, an increase in the vertical velocity near the interface in the present study indicates the existence of the thermal source layer. The profiles in Figs. 4.2 (b) and 4.3 (b) show that for the case of 36 ^{o}C, the thickness of the thermal source layer for the unsaturated case is 2.5 mm and for the saturated case is 3.3 mm. Similarly, for the bulk water temperature of 30 ^{o}C, the thermal source layer was not observed for the unsaturated case which could be due to reason that the thickness of this layer is smaller than the velocity resolution. For the saturated case, the thickness of the layer is 2.5 mm. The trends at both 30 ^{o}C and 36 ^{o}C indicate that for the given bulk water temperature, the thickness of the thermal source layer is increased for the saturated case. However, this behavior is not consistent with the trend for a given saturated or unsaturated case, as the heat flux decreased (i.e. the bulk temperature changed from 36 ^{o}C to 30 ^{o}C), the thickness of the thermal source layer also decreased. This discrepancy could be due to the reason that some other parameter(s) which is influenced by the saturation would play an important role in controlling the thickness of the thermal source layer. For example, for a given bulk water temperature, the surface temperature and the bulk-to-surface temperature difference would change when the air become saturated. This would change the temperature difference across the

conduction layer which would influence the thermal source layer. The detailed dynamics within the thermal source layer are not well understood. Katsaros *et al.* (1977) presented a conceptual model of this region based on the comparison of their temperature profiles with the theoretical conduction profiles. Detailed and high-resolution velocity and temperature measurements in this region are necessary to understand flow dynamics in this layer.

The turbulent kinetic energy (TKE) is plotted in Fig. 4.4 as a function of depth for saturated and unsaturated cases. As seen in Fig. 4.2, except in the region adjacent to the interface, the magnitude of the horizontal turbulent velocity is smaller than the vertical turbulent velocity and also the variation in the horizontal velocity with depth is relatively small. Therefore, the shape and magnitude of the TKE profiles is dominated by the behavior of the vertical turbulent velocity. In the depth range 3 - 4 cm, the magnitude of TKE for the unsaturated case is a factor of 17 and 9 larger than that for the saturation case for the bulk water temperatures of 30 °C and 36 °C, respectively. Similar to the vertical turbulent velocity, the TKE for the saturation case starts decreasing with depth within a short distance from the interface. This indicates that for the saturation case, the flow accelerates to a shorter distance from the interface and then starts decelerating. That is, the falling sheets accelerate as they plunge into the deeper layer but within a short distance they become weak. However, for the unsaturated case, the falling sheets accelerate as they plunge into the deeper water to much greater depths. This indicates that the flow mixing for the saturated cases is restricted to a relatively small region near the interface. As discussed earlier, small density gradients for the saturated cases could be responsible for this behavior.

Bukhari and Siddiqui (2006) conducted a detailed spectral analysis of the length and time scales of the turbulent motions for the unsaturated case. They observed the existence of the buoyancy subrange within the inertial subrange where the turbulent kinetic energy is removed by working against the buoyancy forces (Turner 1973). This was the first evidence of the existence of the buoyancy subrange beneath air-water interface during natural convection. They observed buoyancy subrange in the spectra of the horizontal velocity at all depths. However, for the vertical velocity, no buoyancy subrange was observed in the near-surface region for the higher heat flux. They argued that the buoyancy subrange exits only when the turbulence is strong enough to work against the buoyancy forces. They also found that the range of the length scales of the turbulent motions involved in the interactions with the buoyancy forces does not vary with the heat flux. However, the range of timescales of the turbulent motion reduces with a decrease in the heat flux.

The wavenumber spectra of the horizontal and vertical turbulent velocities were computed for all cases. The one-dimensional wavenumber spectrum was computed in the horizontal direction at all depths in each velocity field and then averaged at each depth. The wavenumber spectra of the horizontal velocity for the saturated and unsaturated cases are shown in Figs. 4.5 (a), 4.6 (a) and 4.7 (a) at depths of 0.33, 2.9 and 8.0 cm, respectively. The spectra are normalized by w_* and z_*. The results in Figs. 4.5 (a), 4.6 (a) and 4.7 (a) show that for the saturated case the buoyancy subrange was observed at all depths. However, the range of wavenumbers over which the buoyancy subrange was observed was smaller than that for the corresponding unsaturated cases. The plots also show that for the saturated case, the range of wavenumbers over which the

buoyancy subrange was observed decreased with a decrease in the bulk water temperature. The plots also indicate that with an increase in depth, the buoyancy subrange became shorter and shifted towards the low wavenumbers. That is, as the overall horizontal turbulent motions became weaker with depth, only a small range of relatively larger and energetic turbulent motions were able to work against buoyancy.

The wavenumber spectra of the vertical velocity for the saturated and unsaturated cases are shown in Figs. 4.5 (b), 4.6 (b) and 4.7 (b) at depths of 0.33, 2.9 and 8.0 cm, respectively. For the saturated cases, no buoyancy subrange was observed at the depth of 0.33 cm. This is due to the reason that the turbulence is not strong enough to work against the buoyancy forces (Bukhari and Siddiqui 2006). At a depth of 2.9 cm where the vertical velocity magnitude is largest for the saturation cases, the buoyancy subrange was observed for 36 °C case but not for the 30 °C. However, at a depth of 8.0 cm where the vertical turbulent velocity magnitude is very small, the buoyancy subrange is manifested at both bulk water temperatures. The presence of the buoyancy subrange at this depth indicates that the buoyancy forces are very weak at this depth and the turbulent intensity (which is relatively weak itself) is strong enough to work against the buoyancy forces. Similar to the horizontal velocity spectra, the wavenumber range for the buoyancy subrange is shorter for the saturated case compared to the unsaturated case.

In Figs. 4.5 (a), 4.6 (a) and 4.7 (a), the inertial subrange was observed at wavenumbers greater than 1500 rad/m. The plots show that the wavenumber range for the inertial subrange is almost the same for both saturated and unsaturated cases and at both bulk water temperatures. This indicates that scales of the horizontal turbulent motions at which the conventional energy transfer takes place is not influenced by the airside

relative humidity or the bulk water temperature. An interesting feature that was observed in the horizontal velocity spectra is that the buoyancy subrange is separated from the inertial subrange. For the unsaturated cases, there is some indication of this separation for the 30 °C case. However, for the saturated cases, this trend is more obvious at both bulk water temperatures. As discussed earlier, for the saturated case, the wavenumber range over which the buoyancy subrange exists decreased towards the low wavenumbers. Since the wavenumber range of the inertial subrange remains unchanged, the buoyancy subrange is separated from the inertial subrange as it is shifted towards the low wavenumbers. In the spectra of the vertical velocity, this separation was not observed for the unsaturated case. For the saturated case, it was observed only at a depth of 8 cm (see Fig. 4.7 (b)). In the wavenumber range that separates the two subranges, the spectra exhibits a slope of -1/2. Turner (1973) argued that the buoyancy subrange exists within the inertial subrange. This implies that the slopes of both subranges should merge within a small range of wavenumbers as evident in the vertical velocity spectra and also in the horizontal velocity spectra for unsaturated case at 36 °C. The existence of the third subrange where the spectra exhibits -1/2 slopes implies that the energy transfer mechanism in this range is different from the other two ranges. The small slope in this range indicates that the energy transfer at these scales is significantly slower than that in the buoyancy and inertial subranges. In this range, the turbulence is too weak to work against the buoyancy forces and, the dissipation rate is not the controlling parameter for the energy transfer. Thus, it can be argued in buoyancy-driven flows, when the turbulence is relatively weak, in addition to the buoyancy subrange, another subrange exists within the inertial subrange, where the turbulent motions are simply convected by the buoyancy

forces. Detailed information about the density gradients and buoyancy forces is necessary in order to provide the physical explanation for the manifestation of this subrange, which is beyond the scope of the present work.

The physical mechanism of the energy interaction beneath air-water interface when the air is saturated can be described as follows. Both the horizontal and vertical turbulent motions are much weaker than that for the unsaturated case. Therefore, the buoyancy subrange was not observed for all cases. For the cases where the buoyancy subrange was observed, it was found that the wavenumber range of buoyancy subrange decreased with depth. That is, as the depth increased, only larger turbulent motions were able to work against the buoyancy. In other words, at smaller depths (i.e. near the surface), there is a range of turbulent motions at relatively higher wavenumbers that were strong enough to work against buoyancy but at greater depths, these turbulent motions became so weak that they were not able to work against buoyancy and simply advected by the buoyancy forces. Thus, it can be concluded that the energy interaction is highly dependent on the energy of the turbulent motions and the magnitude of the buoyancy forces.

4.5 Conclusions

The impact of the air saturation on the turbulent structure beneath the air-water interface has been investigated. The results show that air saturation has a significant impact on the waterside turbulent structure. As the air becomes saturated, the magnitudes of the horizontal and vertical turbulent velocities are decreased on average, by factors of 5 and 2.5, respectively; and the horizontal motions at the water surface are reduced by a factor of 4 to 5. The significant reduction in the waterside velocities is attributed to the

reduction in the surface heat flux, airside velocities and the waterside vertical density gradients during the saturation state. It is observed that the latent heat flux at the saturation state is not equal to zero. The film condensation on the tank walls at the saturation state is found to be responsible for the latent heat flux. The spectral analysis shows that both the horizontal and vertical turbulent motions are much weaker than that for the unsaturated case. For the saturated cases, the range of the turbulent motions responsible for working against buoyancy forces is smaller than that for the unsaturated cases. Furthermore, with an increase in depth, only larger turbulent motions within this range work against the buoyancy and the remaining smaller turbulent motions in the range are advected by the buoyancy forces. It was concluded that during natural convection, when the turbulence is relatively weak, in addition to the buoyancy subrange, another subrange exists within the inertial subrange, where the turbulent motions are simply convected by the buoyancy forces and that the energy interaction is highly dependent on the energy of the turbulent motions and the magnitude of the buoyancy forces.

Case	*Unsaturated Conditions*		*Saturated Conditions*	
T_b (°C)	36	30	35.7	29.8
q''_{total} (W/m^2)	678	367	420	211
q''_s (W/m^2)	591	309	333	153
$q''_{sensible}$ (W/m^2)	49	26	26.4	16
q''_{wall} (W/m^2)	87	58	87	58
w_* (mm/s)	5.1	4.0	4.2	3.1
Ra^*	1.17×10^{12}	5.16×10^{11}	7.14×10^{11}	3.05×10^{11}

Table 4.1: T_b, bulk water temperature; q''_{total}, total heat flux; q''_s, heat flux through the water surface; $q''_{sensible}$, sensible flux through the water surface; q''_{wall}, wall heat flux; w_*, velocity scale; Ra^*, flux-based Rayleigh number.

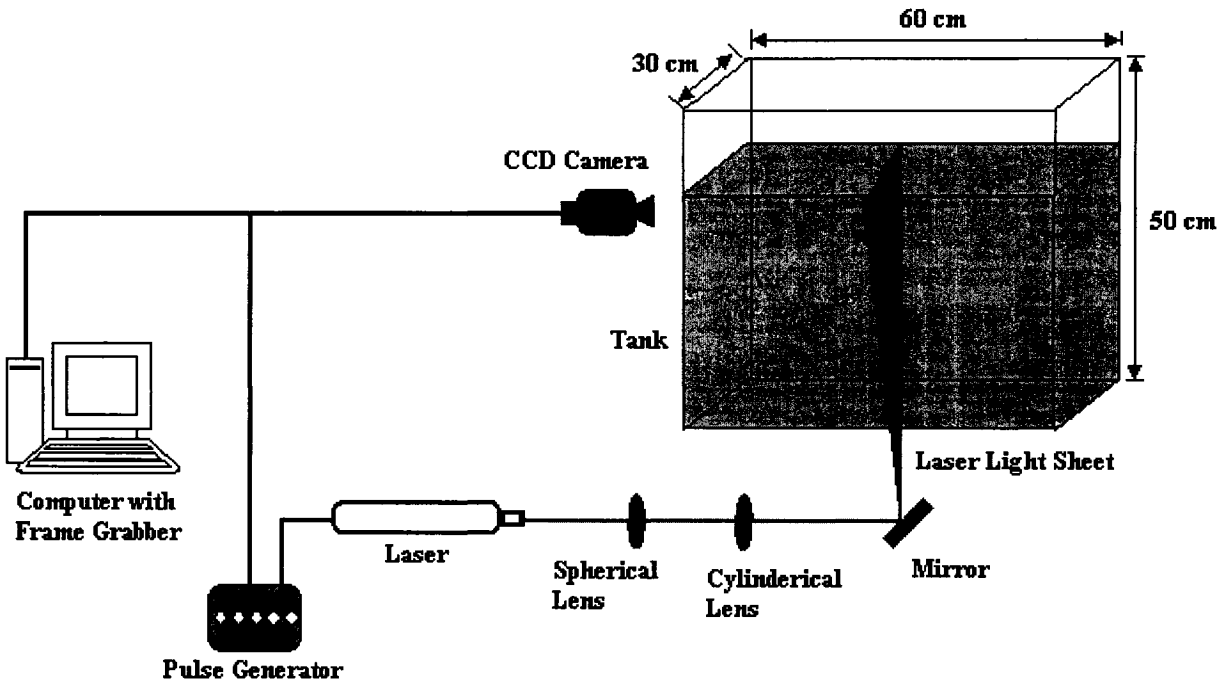

Fig. 4.1: Schematic of the experimental setup.

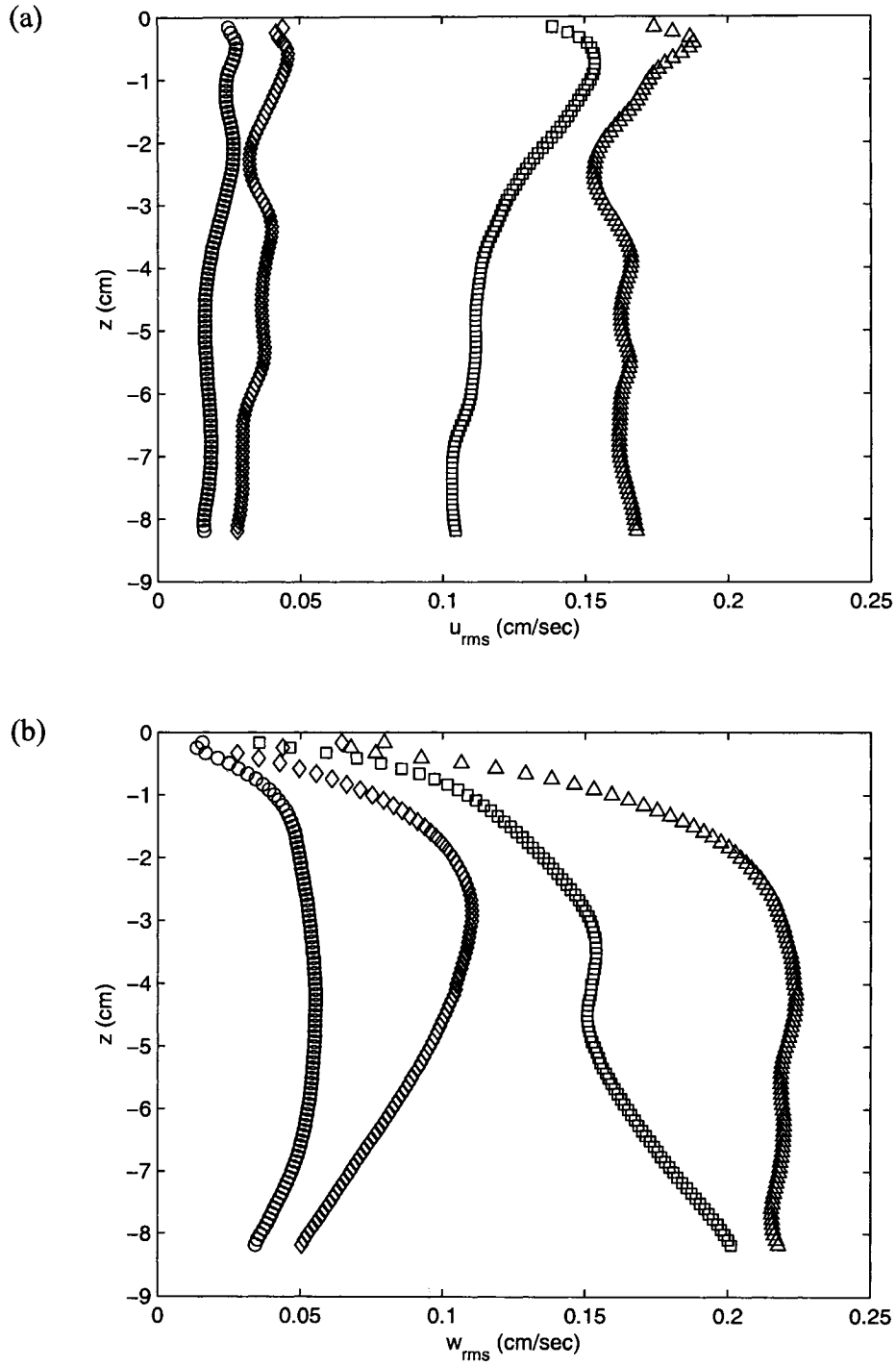

Fig. 4.2: Vertical profiles of the RMS turbulent velocities, (a) horizontal, (b) vertical. ○, = 30 °C (saturated); □, = 30 °C (unsaturated) (Bukhari and Siddiqui 2006); ◊, = 36 °C (saturated); Δ, = 36 °C (unsaturated) (Bukhari and Siddiqui 2006).

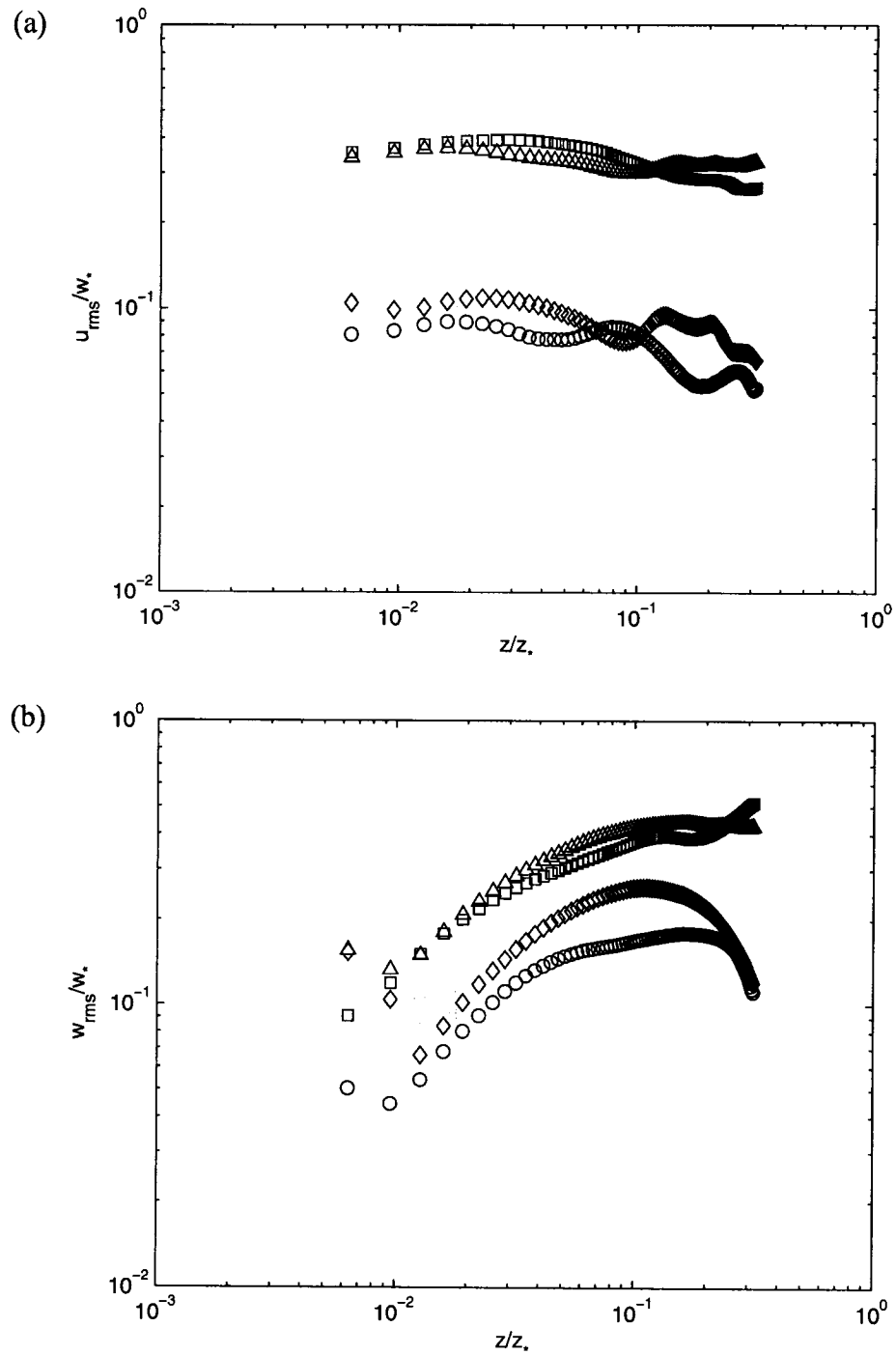

Fig. 4.3: Vertical profiles of the RMS turbulent velocities normalized by w_*., (a) horizontal, (b) vertical. ○, = 30 °C (saturated); □, = 30 °C (unsaturated) (Bukhari and Siddiqui 2006); ◊, = 36 °C (saturated); Δ, = 36 °C (unsaturated) (Bukhari and Siddiqui 2006).

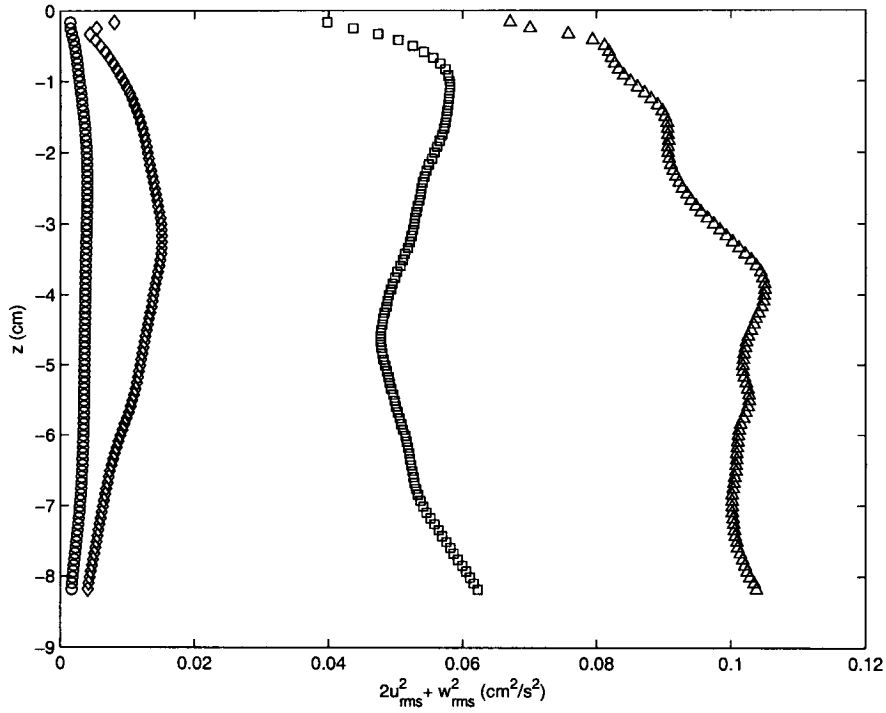

Fig. 4.4: Vertical profiles of the mean turbulent kinetic energy. ○, = 30 °C saturated; □, = 30 °C (unsaturated) (Bukhari and Siddiqui 2006); ◊, = 36 °C (saturated); Δ, = 36 °C (unsaturated) (Bukhari and Siddiqui 2006).

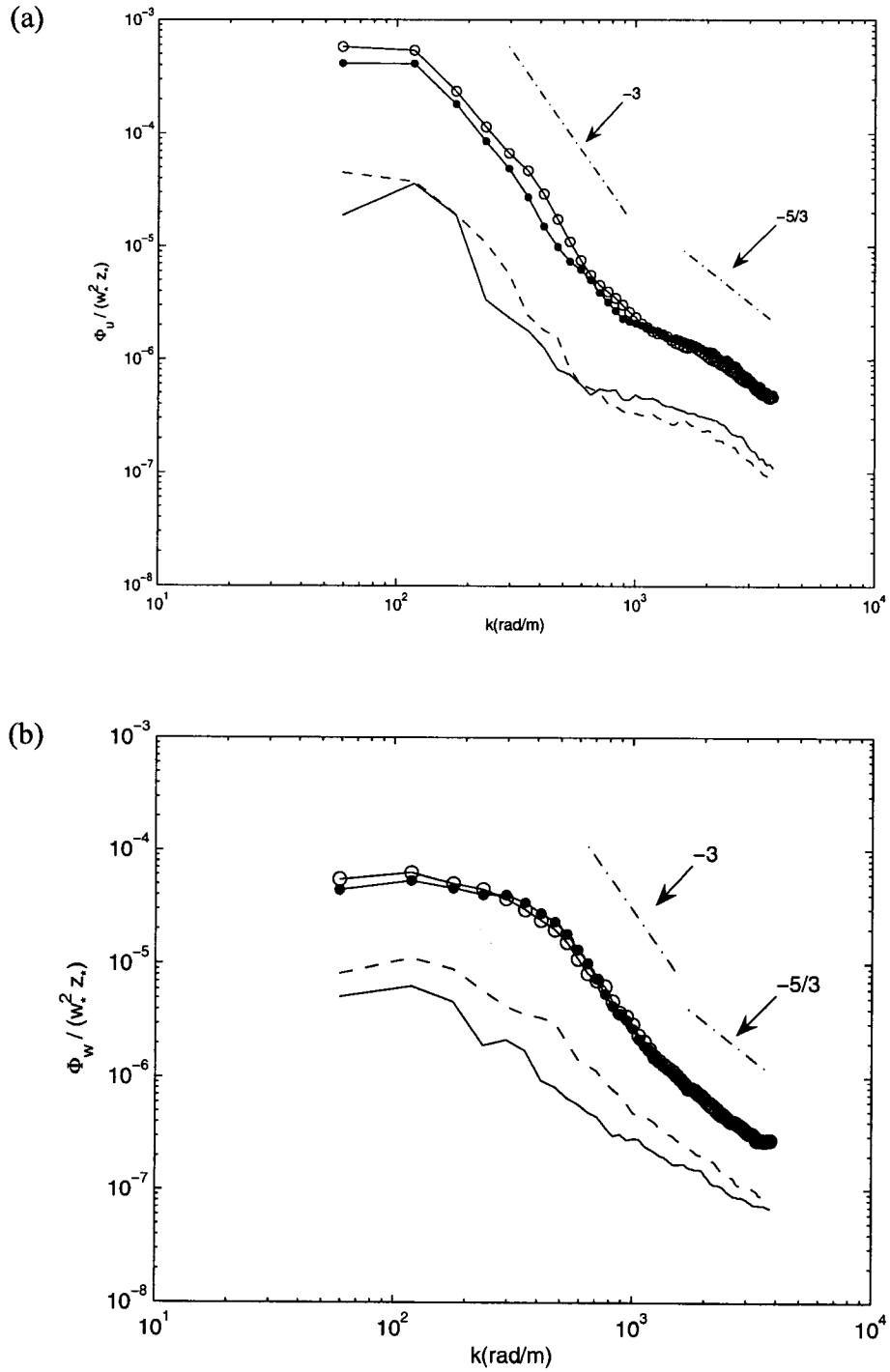

Fig. 4.5: Normalized wavenumber spectra of the turbulent velocities, (a) horizontal, (b) vertical, at depth z = 0.33 cm. ○, = 36 °C (unsaturated); ●, = 30 °C (unsaturated); dashed line, = 36 °C (saturated); solid line, = 30 °C (saturated). Dashed-dotted lines represent slopes.

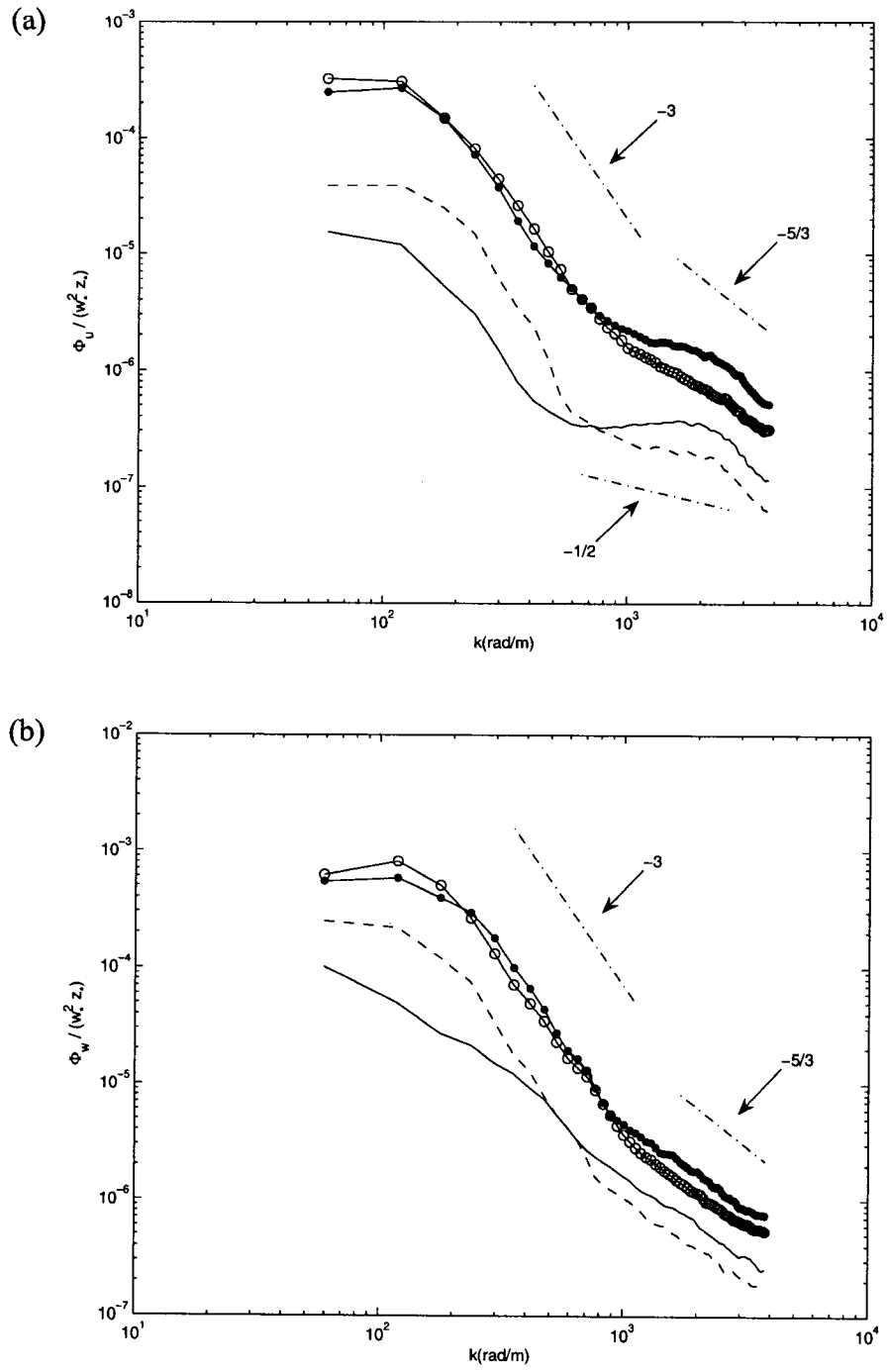

Fig. 4.6: Normalized wavenumber spectra of the turbulent velocities, (a) horizontal, (b) vertical, at depth z = 2.9 cm. ○, = 36 °C (unsaturated); ●, = 30 °C (unsaturated); dashed line, = 36 °C (saturated); solid line, = 30 °C (saturated). Dashed-dotted lines represent slopes.

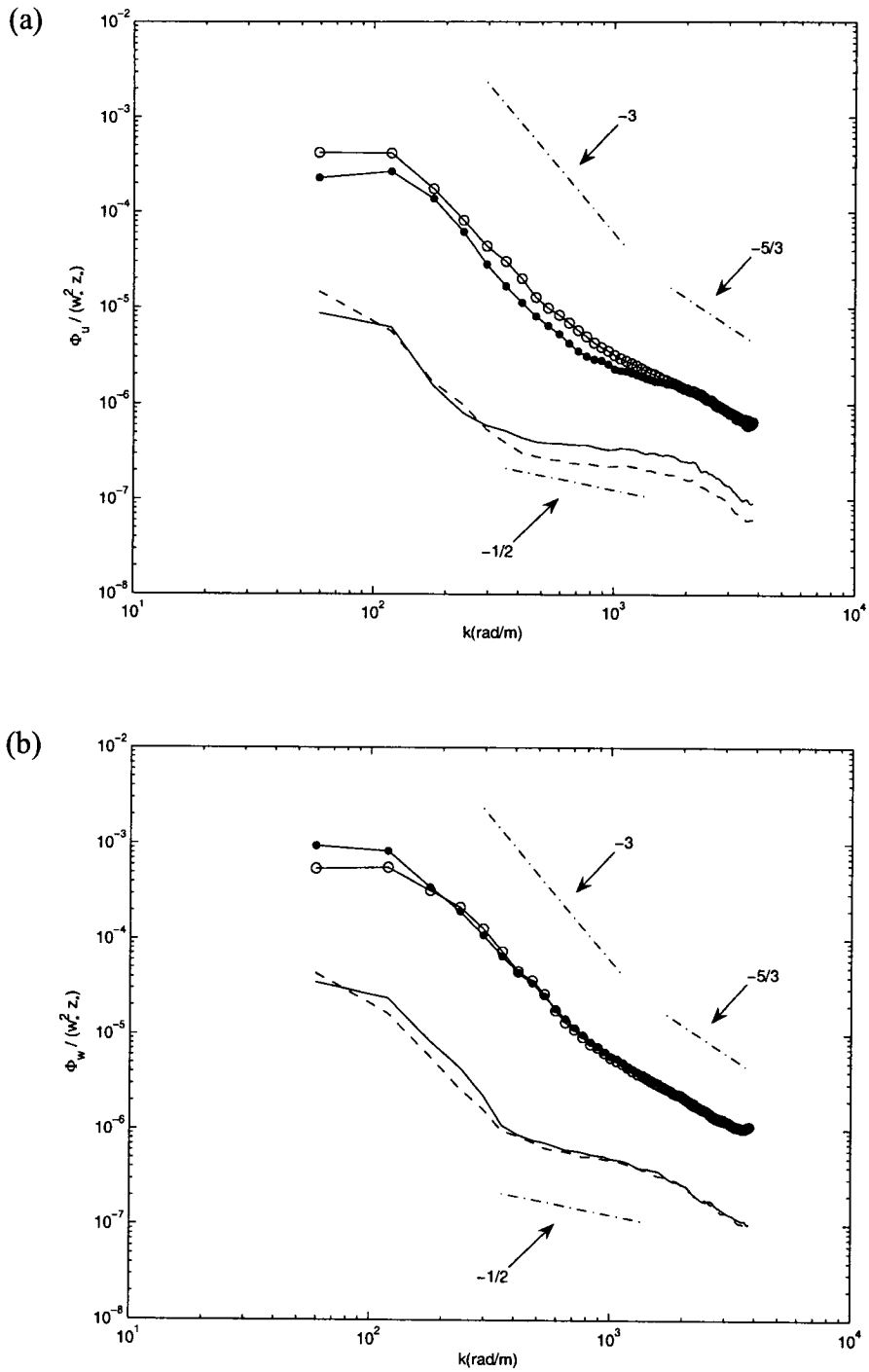

Fig. 4.7: Normalized wavenumber spectra of the turbulent velocities, (a) horizontal, (b) vertical, at depth z = 8.0 cm. ○, = 36 °C (unsaturated); ●, = 30 °C (unsaturated); dashed line, = 36 °C (saturated); solid line, = 30 °C (saturated). Dashed-dotted lines represent slopes.

Chapter 5

An Experimental Study of the Thermal Field underneath an evaporative water surface using Laser Induced Fluorescence (LIF)

5.1 Abstract

An experimental study was conducted to investigate the temperature field beneath an evaporating water surface using laser induced fluorescence (LIF) technique. The spatial distribution of temperature field in a plane perpendicular to the surface shows the presence of falling cold and rising warm water parcels. Large temperature variations are observed within the surface layer whose thickness is of the order of a millimeter which varied horizontally. Spatially and temporally averaged temperature profiles show a characteristic boundary layer distribution in the near surface region with an extensive core of constant temperature in the bulk. The temperature profiles at the higher heat flux show larger depth of temperature variations in the near surface region compared to the lower heat flux. Relationship between the scales of conduction and convection layers for velocity and temperature defined for solid wall case are also found to be valid for free surface case however, the length scales ratio showed the opposite trend. The mean temperature profiles show three distinct regions beneath the water surface where the depth dependency of temperature is different. In the conduction layer, the temperature varied linearly with depth. In the intermediate region, the temperature varies as z^{-1}

whereas, in the bulk region, the temperature varied as $z^{-1/3}$. These dependencies are in good agreement with that for wall-bounded natural convection.

5.2 Introduction

Turbulent thermal convection in a horizontal fluid layer cooled from above has been of considerable interest due to its wide range of applications from geophysical flows in oceanography and meteorology, to technologically relevant flows in heating, ventilation and air conditioning (HVAC), and chemical and nuclear engineering. These flows are ranging from thermal convection, in which buoyancy is the primary motive force, to forced convection in which both hydrodynamic and thermal fields are of equal importance. In thermal convection, for a case of warm water body cooled from above by air, heat flows from the bulk warm water to the surface through conductive and convective modes. At the interface, heat is transferred due to molecular conduction (sensible heat transfer) and evaporation (latent heat transfer). Evaporation results in the formation of cool thin layer at the interface. The bulk warm water underneath has a lower density compared to the cool and denser interface which results in an unstable situation in the fluid layers. A non-dimensional parameter Rayleigh number (Ra) measures the relative strengths of the buoyancy and viscous forces. If the buoyancy forces are small compared to the viscous forces, any disturbances from the quiescent state are damped out. The turbulent motion first occurs when the Rayleigh number is increased by several orders of magnitude beyond the critical Rayleigh number of 1700 for the initiation of convection (Somerscales and Gazda 1969). When the Rayleigh number exceeds 10^6, fully turbulent convection exists in the flow (Goldstein and Chu 1969). This turbulent thermal convection maximizes the heat transport.

Various techniques have been used to obtain the temperature distribution in water. It includes thermocouple (TC) probes, thermistors, resistance temperature devices (RTD) and thermo-chromic liquid crystals (TLC). Thermocouples, thermistors and RTD's are point measurement techniques and extensively used in a wide range of heat transfer applications. A carefully calibrated probe is capable of measuring temperatures with the precision of ± 0.1 K or even better. The primary limitations of using probes are their relatively large spatial resolution and physical intrusiveness in the flow i.e. the effect of the probe on the flow pattern can never be avoided. In addition, their point measurement nature makes full-field temperature mapping very cumbersome because large number of probes must be placed and monitored simultaneously. The finite size of the probe also does not allow measurements very close to the surface. Thermo-chromic liquid crystals are commonly used to visualize temperature fields. The temperature measurements of the TLCs depend on their optical properties because these materials change color with temperature via reflection of specific wavelength of light. The relationship between the color and temperature allows quantitative temperature measurements. The difficulty in using TLC is that one has to calibrate each point of the region of interest. In addition, the accuracy of TLC relative to the measurement range is not very large (Sakakibara and Adrian 1999).

Recently, a new technique has been developed to obtain high resolution temperature measurements in a two dimensional plane, non-intrusively called laser induced fluorescence (LIF). This technique uses temperature sensitive fluorescent dyes excited by the laser light and has been considered as a feasible temperature mapping technique (Kim *et al.* 2003). The fluorescence intensity of the dye molecules is

proportional to the exciting light intensity, the concentration of the dye and the optical constant of the dye called quantum efficiency. The relative accuracy of this method is higher than that of the TLC method because it allows a wider range of temperature variations (Sakakibara and Adrian 1999). The dye whose fluorescence intensity depends on the temperature can be used to measure the temperature of the flow field keeping its concentration and exciting light intensity constant, is called the temperature sensitive dye (Heon 2003). But the variation in the exciting light intensity may change the fluorescence intensity and the gray scale values of the fluorescence images. The exciting light intensity may vary due to the laser beam or laser sheet divergence, scattering by small particles in the beam path (impurity of the solution) and time dependent lasting efficiency (Sakakibara and Adrian 1999, Kim *et al.* 2003). Therefore, it is essential to compensate the effect of the change in the light intensity in the fluorescence images to get true representation of the temperature field.

Most of the previous studies on thermal convection were performed between parallel plates uniformly heated from below and cooled from above. However, the convection beneath an evaporative water surface has not been adequately studied. There are only few studies reported in the literature which investigated the flow and thermal behavior beneath the air water interface during natural convection. Volino and Smith (1999) used infrared imagery and digital particle image velocimetry (DPIV) to measure surface temperature and sub-surface velocity fields at high Rayleigh numbers. They observed that the temperature field at the water surface was very complex showing different scales of thermal structures that appear to be randomly located on the water surface. The cool skin layer present on the water surface was approximately 0.5 and 2 ^{o}C

cooler than the bulk water for low and high heat flux cases, respectively. They found that the cooler water surface plunges into the warmer bulk water below, in sheet-like plumes. However, no strong correlation between the temperature field and the sub-surface velocity fields was observed. Flack *et al.* (2001) measured surface temperature and sub-surface turbulence during evaporative convection using infrared imagery and two component laser Doppler velocimetry, respectively. They conducted experiments with water temperature 14 - 16 °C above the bulk air temperature for two different free-surface conditions; one with a clean surface (shear free condition) and the other in the presence of a surfactant monolayer. Similar to Volino and Smith (1999), they also observed a wide range of temperature scales at the surface, including very fine scales for the clean surface. For the surfactant case, they observed that the small-scale thermal structures at the surface are damped out by the surfactant. They also found that the surfactant influences the subsurface flow field and reduces the magnitude of turbulent fluctuations. Saylor *et al.* (2001) measured the water surface temperature fields using infrared imagery for a range of heat fluxes 30 – 500 W/m^2 with and without a surfactant monolayer. They observed an increase in small scale structures with an increase in the heat flux for both clean and surfactant cases. The effect of the surfactant monolayer on the structures of the temperature field was also evident from their IR images. They found that the surfactant monolayer eliminates the small scales which were present in the clean fields. Their surface temperature fields showed a variation of temperature from 0.6 to 2.6 K and this variation increased with an increase in the heat flux.

Bukhari and Siddiqui (2007) numerically investigated the airside and waterside flow behavior in a coupled air-water system undergoing natural convection. They

concluded that the air and water temperatures significantly affect the magnitude of the velocity fields on both air and water sides. For high water temperatures, they found that the magnitude of the root-mean-square (RMS) airside velocity is an order of magnitude higher than the RMS waterside velocity. Bukhari and Siddiqui (2006) experimentally investigated the turbulent structure beneath the air-water interface during natural convection using DPIV technique. The experiments were conducted for three cases. Two cases correspond to the unstable thermal stratification with bulk water 13 °C and 7 °C warmer than the bulk air and the third case correspond to the neutral condition. Based on the analysis of the two-dimensional turbulent velocity fields they argued that during natural convection, the waterside flow field is three-dimensional that undergoes different flow interactions locally, which result in the formation of complex flow patterns. They also observed self-similar behavior in the turbulent velocities for different cases and showed that the scaling parameters used for the flow above a heated solid wall are also suitable for the flow field beneath the evaporative interface. From the spectral analysis they showed that the buoyancy subrange exists within the inertial subrange when the turbulent motions are strong enough to work against the buoyancy force. Spangenberg and Rowland (1961) used Schlieren photography to study the convection currents induced by evaporation at the water surface. They observed that the cool water surface collects along lines, which causes local thickening of the surface layer that becomes unstable and plunges into deeper water in the form of sheets. They also observed that the form of the plunging regions generated at the surface is time-dependent and changes continuously and have no fixed pattern. They found more sheets per unit area with an increase in the heat flux.

The only detailed analysis of the temperature field in the thermal boundary layer beneath the water surface during thermal convection is reported by Katsaros *et al.* (1977). They measured the mean and instantaneous temperature profiles using resistance thermometer, traversing parallel and perpendicular to the surface at high Rayleigh numbers. They observed that the measured mean temperature profile in the boundary layer was highly nonlinear and away from the surface the temperature variations were organized showing an almost constant temperature. From the data and visualization of the flow, they deduced that the cold fluctuations were due to cold water plunging down from the boundary layer just under the surface. They argued that the thermal boundary layer acts as a source of the fluid for the cold sheets and warm water enters the boundary layer from below by advection.

With the limited theoretical and experimental studies on the natural (thermal) convection process, thermal structure beneath the evaporative water surface in particular near the interfacial region is not well understood. Volino and Smith (1999), Flack *et al.* (2001) and Saylor *et al.* (2001) measured water surface temperature using IR imagery. However, the results presented in these studies are mostly qualitative description of the thermal fields at the water surface. Katsaros *et al.* (1977) conducted a detailed analysis of the temperature field underneath the free water surface using traversing probe. However, horizontal spatial resolution of the temperature measurement was relatively low and the effect due to the probe intrusion on the flow pattern could not be avoided particularly during traversing. In the present study, non-intrusive laser induced fluorescence (LIF) technique has been used to investigate the thermal characteristics beneath air-water interface during natural convection. As far as the authors know, this is the first study

reporting the temperature measurements beneath water surface during natural convection using LIF. Sakakibara and Adrian (1999) also measured the temperature field using LIF. However, their study was focused on the thermal convection over a heated horizontal surface. They used two-color laser-induced fluorescence technique using Rohdamine B and Rohdamine 110, as temperature indicator dyes. For their experiments mean heat flux was 27 kW/m^2, the mean temperature drop from the heated surface to the center of the mixed layer was 15 K and the Rayleigh number was 1.3×10^7. They observed that the flow field was dominated by turbulent structures in the form of plumes, ridges and thermals. Collen *et al.* (1999) measured water temperature field between heating and cooling walls, during natural convection using LIF. They used Rhodamine B fluorescent dye as a temperature indicator. They observed temperature stratification in the middle of the test section. They also found large temperature gradients near the hot and cold walls with relatively constant temperature in the middle section. However, they did not present any detailed analysis of the temperature field. Their main focus was to verify the experimentally measured temperature field with the numerically estimated field using finite element package SEPRAN.

5.3 Principle of LIF Technique

Fluorescence is the property of an atom or a molecule that is excited by an incident light. Absorption of photon energy by a fluorescent dye molecule results in an increase in its potential energy from the ground state to the excited state. After a very short interval, termed as fluorescence lifetime, it emits light at longer wavelength known as radiative process. The absorption of photon energy by a fluorescent molecule can only occur when the incident light has wavelength within specific range known as the

absorption band. The emission of fluorescence occurs at certain wavelength, larger than the absorption band and at lower energy due to the loss of some of the absorbed energy by the molecule during interactions with the environment before it emits fluorescence. These non-radiative processes reduce the fluorescence efficiency. The fluorescence energy I emitted per unit volume (W/m^3) is defined as (Sakakibara and Adrian 1999),

$$I = I_o C \phi \varepsilon \tag{5.1}$$

where, I_o is the incident light flux (W/m^2), C is the concentration of the dye solution (kg/m^3), ϕ is the quantum efficiency and ε is an absorption coefficient (m^2/kg). The quantum efficiency, ϕ, is the ratio of the total energy emitted per quantum of energy absorbed by the molecule. That is,

$$\phi = \frac{(energy)_{emiiited}}{(energy)_{absorbed}} \tag{5.2}$$

The value of the absorption coefficient 'ε' is usually expressed at the maximum wavelength of the absorption and does not have significant temperature dependency. In most of the dyes, the quantum efficiency is temperature dependent. The change in the fluorescence intensity is normally small, usually less than a fraction of one per cent per Kelvin. However the sensitivity of some dyes such as Rohdamine B can be as high as 2 % per Kelvin (Sakakibara and Adrian 1999). Therefore, it is possible to measure the temperature of the solution keeping incident light intensity and concentration constant. Incident light intensity 'I_o' is likely to be inhomogeneous and affected by various factors including convergence and divergence of the laser light sheet, scatter by small particles in the beam path and refraction of the light passing through the medium. This variation in the incident flux through the medium leads to the selection of dyes having different

quantum efficiency dependence on the temperature. The dye with strong temperature dependence is called the temperature sensitive dye and used for temperature field analysis. The fluorescence images of the temperature sensitive dye show the effect of both temperature and incident light variations. Therefore, the bias in the temperature measurements caused by the incident light variations can be compensated by normalizing the fluorescence intensity by the reference images (Collen *et al.* 1999).

5.4 Experimental Setup and Methodology

Experimental setup used in the present study is shown in Fig. 5.1. Experiments were conducted in a glass tank 60 cm long, 30 cm wide and 50 cm deep. The initial water depth was set equal to 26 cm and the bulk air temperature was 23 °C. During the experiments, the tank top was left open to allow evaporation into the room air. The measurements were made in a plane perpendicular to the water surface at the mid-tank location along the longer tank dimension i.e. 30 cm from the end. In the present study, Rhodamine B (RhB) is used as temperature sensitive dye which has an absorption band peak at 543 nm and an emission band peak at 575 nm (Tekni Science Inc.). An Nd:YAG laser (Solo PIV 120XT, New Wave Research Inc.), at 532 nm wavelength was used to excite the dye molecules which is suitable for the absorption wavelength band of the RhB dye (Sakakibara and Adrian 1999, Collen *et al.* 1999). A set of optics is used to produce a laser light sheet in the region of interest to measure temperature field in a two-dimensional plane. A CCD camera (JAI CV-M2) with resolution of 1600 × 1200 pixels was used to record the images. The field of view of the camera was set equal to 3.2 cm horizontal and 2.4 cm vertical. A long pass filter that transmits wavelengths longer than 560 nm (Newport Experience Solutions Corporation) was attached to the camera lens to

avoid low wavelength reflected light from entering the camera. The camera was connected to a PC equipped with a frame grabber (DVR Express, IO Industries, London, ON, Canada) that acquired 8-bit images at a rate of 30 Hz. A four-channel digital delay generator (555-4C, Berkeley Nucleonics Corporation, San Rafael CA) was used to control the timing of the laser light pulses. The bulk temperature of water was monitored by using Traceable Digital Thermometer (Control Company USA) which has an accuracy of ±0.05 °C. Thermometer was placed near the corner of the tank at a depth of 12 cm from the interface. Two experimental cases were considered that correspond to the bulk water temperatures of 36 and 30 °C. Hereinafter, these cases are referred as high and low heat flux cases, respectively. The experimental procedure is as follows. The tank was filled with clean tap water at a temperature of 38 °C. RhB dye with the concentration of 0.05 mg/l was mixed with water and stirred thoroughly. The data acquisition was started as soon as the bulk water temperature reached the set bulk water temperature value i.e. 36 and 30 °C for first and second case, respectively. For each case, 4500 fluorescence images were acquired at a rate of 15 Hz for a period of five minutes. The total heat loss per unit area (q''_{total}) from the tank was computed by measuring the rate of decrease of the bulk water temperature that is dT_b/dt in the mid plane depth in a separate set of experiments under identical conditions. The surface heat flux (q''_s) was computed as the difference between the total heat loss and the heat loss through the walls. Details of the heat flux measurements are given in Bukhari and Siddiqui (2006). The values of the total and surface heat fluxes for both cases are presented in the Table 5.1.

5.5 Calibration

Calibration in the LIF technique is necessary in order to obtain temperature fields. In the present study, calibration was performed in two steps. In the first step, calibration was conducted to estimate the effect of pulse energy variation and to compensate for the non-uniformity in the laser light sheet on the gray scale values of the images. The intensity of the light sheet along the horizontal axis has a Gaussian-like distribution. That is, higher gray-scale values in the center of the light sheet, which decreased gradually towards the edges. We followed a procedure similar to Collen *et al.* (1999) who considered two reference images to compensate for the effects of non-uniformity in the fluorescence images due to the laser light intensity distribution. In the present study for each case, the first and last fluorescence images were considered to compute a reference image from the average of first and last images. The horizontal distribution of the gray values in the bulk water region was then obtained by depth-averaging the data in the corresponding region of the reference image. The gray-scale value corresponding to the bulk water temperature measured from the digital probe was considered as a reference to compute the deviation in the horizontal gray-scale values from the reference value due to the non-uniformity in the laser light sheet. The computed deviations in the gray-scale values in the reference image were then used to correct the effect of laser light intensity variation in the acquired data set.

Degradation of dye due to chemical/photochemical decomposition results in a decrease in the fluorescence intensity during excitation (Collen *et al.* 1999). To estimate the change in fluorescence intensity over the data acquisition period of 5 minutes, another set of experiments were conducted at the room temperature. The images were acquired

for 5 minutes at 30 Hz. The gray-scale values in the first and last images were compared to compute the change in the fluorescence intensity. The results show that the change in gray-scale values due to chemical/photochemical decomposition over 5 minutes duration is 0.1%. Collen *et al.* (1999) also argued that the pulse energy between the successive pulses of the Nd:YAG laser varies approximately 3% resulting in a variation of the fluorescence intensity for constant temperature of about 3%. In their case, for 30 images, they estimated that the influence of variations in the laser power was minimized to 0.55%. Using the same approach, for 4500 images, the influence of the laser power variation was estimated to be 0.045%.

Establishing a relation between the fluorescence intensities (i.e. image gray-scale values) and the temperature is necessary in order to convert gray-scale values into temperature units. In the second step, the calibration was conducted to obtain a relationship between the gray values and the temperature. To obtain a calibration equation, calibration images were taken during the same set of experiments. To acquire calibration images, the digital thermometer probe was placed at a depth of approximately 2 cm from the interface and 1 cm behind the laser light sheet. The calibration images were acquired at different bulk water temperatures varied from approximately 37 ^{o}C to 24.5 ^{o}C. Two fluorescence images were acquired at each temperature. Immediately after the acquisition of the calibration images, the digital temperature probe was placed back to its original position to monitor the bulk temperature. However in the calibration images, signature of the temperature probe was also visible. The gray values near the probe (excluding the probe image) in an area of approximately 0.5 cm^2 were averaged and considered to be the most representative of the temperature reading shown by the digital

thermometer probe. It should be noted that the image of the probe did not influence the gray-scale values in the region adjacent to the probe. A linear fit to the data provided the calibration equation. This calibration equation was then used to convert the gray values of the fluorescence images into the temperature units.

The uncertainty in temperature measurements using LIF technique is due to the uncertainty in the calibration equation, pixel-depth of the camera (8-bit in the present case), laser light intensity variation, change in fluorescence intensity due to chemical/photochemical decomposition, and the uncertainty in the digital temperature probe. Accounting all these factors, the uncertainty in the temperature measurements in the present study is estimated to be ±0.86 °C. The uncertainty in the present study is comparable to the uncertainty reported in the previous LIF studies. For example, Kim *et al.* (2003), reported an uncertainty of ±1 °C, Sakakibara and Adrian (1999) estimated an uncertainty of ±1.4 °C and Collen *et al.* (1999) found an uncertainty of ±1.7 °C.

5.6 Interface detection

During LIF imagery, the position of the camera was set in a way that at the beginning of the experiments, the upper edge of the image was 150 pixels (i.e. 0.3 cm) above the air-water interface. As the camera was left undisturbed during the entire set of experiments, the water level dropped from the first experimental run to the second due to continuous evaporation from the water surface. To obtain accurate estimates of the near-surface temperature fields, the correct location of the air-water interface for each experimental run is necessary. A scheme was developed to accurately detect the air-water interface in the LIF images based on the gray-value variations. Since no light was emitted or reflected from the airside, the portion of the image that corresponds to the airside was

relatively dark with low gray-scale values. On the waterside, low temperature regions correspond to higher gray-scale values and high temperature regions correspond to lower gray-scale values. As a thin cool layer is formed at the water surface due to evaporation, the gray-scale value at the interface was maximum, which decreased away from the interface on both sides. In the present scheme, the gray-scale values in each column of the fluorescence image were checked pixel by pixel from top to bottom. The coordinates of the highest gray scale value in each column were then recorded that correspond to the interface location. The uncertainty in locating the interface was ±2 pixels (i.e. ±40 μm). Once the interface was located, the portion of the image above the interface was removed. The remaining portion of the image then corresponds to the temperature field on the waterside from the interface to the bulk region. These images were then used for further analysis.

5.7 Results and Discussion

Fig. 5.2 shows the spatial distribution of the time-averaged waterside temperature field in the vertical plane for the high heat flux case (i.e. bulk water temperature of 36 °C). In the figure, darker regions correspond to the cool water and the brighter regions correspond to the warm water. The cool layer at the water surface is also evident in the figure. Evaporation from the water surface is the primary source for the creation of this cool surface layer. As the bulk warm water is less dense than the cool layer near the interface, convective currents are induced into the water which comprised of the falling sheets of cool and dense water and rising plumes of warm water. The temperature field in Fig. 5.2 also shows the presence of falling sheets and rising plumes within the

measurement region. The alternate rising plumes and falling sheet are observed in the middle portion of the image. Cold and warm regions are also visible in the right and left portions of the image, however, these regions are not extended vertically. That is, they are deviated from the vertical path. Bukhari and Siddiqui (2006) presented and discussed the waterside turbulent velocity behavior during natural convection under same conditions. They showed that the rising plume or falling sheets does not follow a continuous vertical path throughout the domain. Instead, they undergo various local interactions that distort and divert the motion of most of the rising plumes and falling sheets. Adrian *et al.* (1986) visualized the flow above a heated wall and observed that the thermal plumes originated from the bottom wall were deviated as large as 60 degree from the vertical, which is consistent with the present observations beneath evaporative water surface.

Large temperature variations are observed within the surface layer whose thickness is of the order of a millimeter. The image also shows that the thickness of the surface layer varied horizontally. It is observed that the surface layer is thicker above the falling sheet and thinner above the rising plume. This is due to the reason that the cold water in the surface layer converges to form the falling sheet. Katsaros *et al.* (1977) also visualized the vertical convection patterns using rheoscopic fluid. They observed that the cold water in a region under the water surface converges along lines and then plunges down in the form of sheets. These falling sheets dissipate as move into the bulk water. Spangenberg and Rowland (1961) used Schlieren photography to study the convection currents induced by evaporation at the water surface. They also observed that the cool water surface collects along lines, which causes local thickening of the surface layer that

becomes unstable and plunges into deeper water in the form of sheets. The surface thermal imagery of Volino and Smith (1999) also shows that the cold water converges along lines at the water surface which further confirm the sheet-like structure of the falling sheets. The trends in Fig. 5.2 supported the argument of Spangenberg and Rowland (1961) that as the thickness of the cool layer increases, it becomes unstable and plunges in the deeper water in the form of falling sheets. Katsaros *et al.* (1977) also observed horizontal temperature variations in the near-surface region which decreased with depth which is consistent with the present results.

Fig. 5.3 shows the vertical temperature profiles for both cases. The profiles are spatially and temporally averaged at each depth from 4500 fluorescence images captured during each case. The characteristic boundary layer and near-isothermal bulk region are evident in the figure. The plot shows as expected, that the lowest temperature is observed at the interface where the cool surface layer exists and the maximum temperature is in the bulk region at greater depths. In the present study, the closest temperature measurement with respect to the interface, are observed at a depth of 20 μm. Considering the uncertainty in locating the water surface as discussed earlier, the present study provides the first non-intrusive waterside temperature measurements within a distance of 40 μm from the air-water interface during natural convection. The plot shows a linear temperature variation immediately below the interface. This region corresponds to the conduction layer where the heat transfer is primarily due to molecular conduction (Katsaros *et al.* 1977) and this thin layer does not take part in the turbulent exchange. The thickness of the conduction layer was found to be approximately 0.8 mm and 1.1 mm for

the low and high heat flux cases, respectively. This indicates that the conduction layer thickness increases with the heat flux.

The profiles in Fig. 5.3 show a sharp temperature increase within the conduction layer followed by a gradual temperature increase over a depth of 5 - 7 mm. At greater depths, the temperature remained almost the same and equal to the bulk water temperature. At greater depth where the influence of the molecular conduction in the vertical direction vanishes, the upward advection has a little effect on the temperature profiles since $\frac{\partial T}{\partial z}$ is nearly zero and most of the interaction occurs due to the turbulent exchange. The constant bulk temperature behavior shown in the profiles indicate that bulk of the fluid is well mixed due to interactions of different flow structures such as rising plumes, falling sheets and horizontal flows. The detailed analysis on the interaction of these flow structures is presented in Bukhari and Siddiqui (2006). Katsaros *et al.* (1977) presented temperature profiles acquired at different instances under constant heat flux conditions. These profiles also show that the maximum temperature variations are within 8 mm depth from the interface followed by an almost constant bulk temperature.

The mean surface temperature for low and high heat flux cases are 32.4 °C and 27.3 °C, respectively. This indicates that the surface to bulk temperature difference was larger for the high heat flux case (ΔT = 3.5 °C) compared to the low heat flux case (ΔT = 2.6 °C). This is due to the reason that the temperature field at higher bulk water temperature has larger surface heat flux and is more active as the warm fluid rises to the surface and cold fluid falls rapidly in the form of the cool sheets. Saylor *et al.* (2001) also observed an increase in the small scale structures with an increase in heat flux in their infrared images which indicate that the surface temperature field becomes more chaotic at

high surface heat fluxes. Bukhari and Siddiqui (2006) observed that from the neutral condition (i.e. equal bulk air and water temperatures) to 36 °C bulk water case, the turbulent kinetic energy on the waterside was increased by a factor of four, and from 30 °C to 36 °C bulk water cases, the turbulent kinetic energy was increased by a factor of two. They also observed a sharp increase in the turbulent kinetic energy within the top 1 cm layer for all cases. These results indicate that strong turbulent motions are induced as the bulk air-water temperature difference increases, which enhance mixing.

Previous studies on natural convection for free surface or wall bounded flows also found a sharp temperature gradient near the surface and nearly isothermal regions away from the surface. The thermal and hydrodynamics boundary conditions for the natural convection between solid walls are different from that beneath an evaporative water surface. For the former case, the velocity becomes zero at the boundaries due to no slip condition and the thermal boundary condition could be constant temperature or constant heat flux. However, for the latter case, slip occurs at the water surface that is, a non-zero horizontal velocity component and the surface temperature is not constant. The thermal boundary condition would be a quasi-constant heat flux (Katsaros *et al.* 1977). Furthermore, the heat transfer from the water surface is in the form of latent and sensible heat, where the former constitutes almost 90% of the total surface heat flux (Volino and Smith 1999, Bukhari and Siddiqui 2006, and Katsaros *et al.* 1977), whereas, sensible heat transfer is the mode for the wall bounded case. Thus, in the near-surface region, the flow and thermal structures for the two cases could be different. Bukhari and Siddiqui (2006) found that the turbulent structure beneath evaporative water surface is similar to that observed in the near-surface region above a heated wall. They observed that the

normalized vertical velocity fluctuations were comparable for both cases, whereas, the normalized horizontal fluctuations away from the boundary were higher for the heated wall case. Katsaros *et al.* (1977) compared the Nusselt number for a range of Rayleigh number for free surface and wall bounded cases and found a reasonable agreement between the two. They however, observed that the slope of Nusselt number versus Rayleigh number relation is steeper for the evaporative water surface case.

In natural convection, two length scales are typically used to normalize the depth. In convection layer (i.e. the entire water layer except the conduction layer) which is also referred to as the outer layer, the water depth, z_*, is used as the scaling parameter, whereas, in conduction layer, the thickness of the conduction layer, δ, is used as the scaling parameter (Adrian *et al.* 1986). The thickness of the conduction layer in the present study is obtained from the linear range of the mean temperature profiles in Fig. 5.3. That is, the depth at which the linear temperature range ends is considered as the thickness of the conduction layer. The values of δ are given in Table 5.1. The normalized mean temperature profiles for both cases are plotted versus the depth normalized by convection or outer layer and conduction layer scaling in Fig. 5.4 (a) and 5.4 (b), respectively. Both plots show that for the given heat flux cases, the temperature profiles collapse very well with both outer and inner layer scaling over the entire depth. The plot in Fig. 5.4 (b) also shows that the temperature difference across the conduction layer depends on the bulk temperature and surface-to-bulk temperature difference. It was also observed that more than 70% of the bulk-to-surface temperature loss occurs across the conduction layer. Deardorff and Willis (1967) also found that 70% temperature change occurred across the conduction layer. Goldstein and Chu (1969) observed 80%

temperature change across the conduction layer. Both of these studies were focused on the natural convection between the solid walls. As mentioned earlier, the only detailed temperature measurements beneath evaporative water surface were conducted by Katsaros *et al.* (1977). They presented a single normalized temperature profile obtained by averaging the data at different heat fluxes. The mean temperature profile from Katsaros *et al.* (1977) is also plotted in Fig. 5.4 (b) for comparison. The plot shows that the data from Katsaros *et al.* (1977) slightly deviated from the present experimental data within the conduction layer. The temperature profile in their case is extended up to approximately 8δ where it reached close to the bulk value. In the present study, we observed that for both cases, the temperature reached the bulk value close to 10δ. Goldstein and Chu (1969) studied two Rayleigh number ranges and found that for the low Rayleigh number range (6×10^5 to 6×10^6), the bulk temperature is reached around 4δ and for the high Rayleigh number range (9×10^6 to 2×10^8), the bulk temperature is reached close to 6δ. Considering the uncertainties in the estimation of δ, the agreement between the present and previous studies is good. Chu and Goldstein (1973) showed that the thickness of the thermal boundary layer increases with an increase in the Rayleigh number.

As mentioned earlier, Bukhari and Siddiqui (2006) showed that the convective or outer layer velocity and length scales proposed for the natural convection over solid walls are also applicable to the velocity fields beneath evaporative water surface during natural convection. Adrian *et al.* (1986) proposed relationships between the conduction and convection layer scales of length, velocity and temperature based on Reynolds and Prandtl numbers for wall bounded natural convection. These relationships are given as

$$z_*/z_0 = (Re_* Pr)^{3/4} \tag{5.3}$$

$$w_*/w_0 = (Re_* Pr)^{1/4} \tag{5.4}$$

$$\theta_*/\theta_0 = (Re_* Pr)^{-1/4} \tag{5.5}$$

where z_* is the water depth, z_0 is conduction layer thickness (δ in the present study), Re_* is the Reynolds number, Pr is the Prandtl number, w_* is the velocity scale in the outer layer, w_o is the velocity scale in the conduction layer, θ_* is the temperature scale in the outer layer, θ_o is the temperature scale in the conduction layer. Since in the present study, we are able to resolve conduction layer therefore, we investigated the validity of these relationships beneath evaporating water surface. The values of parameters listed in the above equations are presented in Table 5.1. The results show that the velocity and temperature scales relations (equations 5.4 and 5.5) agreed well for free surface flows, however the ratio of the conductive and convective length scales beneath evaporative water surface does not agree with the relation in equation (5.3). The results show that beneath evaporative water surface, the ratio z_* / z_o decreased with an increase in the surface heat flux which is due to the increase in the thickness of the conduction layer. However, according the equation (5.3), this ratio should be smaller for the high heat flux case. This implies that in wall bounded natural convection such as, flow above a heated wall, the thickness of the conduction layer decreases with an increase in the wall heat flux. This discrepancy can be explained on the basis of the difference in the thermal boundary condition at the interface. In wall bounded natural convection, the heat transfer across the solid-fluid interface is sensible heat transfer. The decease in conduction layer thickness at higher heat flux in this case would be due to stronger turbulent motions at higher heat flux, which reduce the thickness of the conduction boundary layer. Therefore,

the conduction layer thickness is dependent on Prandtl and Reynolds number. In natural convection beneath evaporative water surface, the modes of heat transfer are sensible and latent heat transfer where latent heat transfer constitutes more than 80% of the total surface heat flux. The latent heat flux causes a significant energy reduction in the conduction layer due to evaporation as compared to the sensible heat flux. Bukhari and Siddiqui (2006) found smaller horizontal velocity fluctuations beneath evaporative water surface in the convection layer compared to the wall bounded case. Thus, the conduction layer is expected to grow with the heat flux beneath evaporative water surface. In this case, the turbulence in the convection layer does not significantly influence the thickness of the conduction layer and therefore, it is mainly influenced by the thermal diffusivity. Thus, the thickness of the conduction layer is expected to be the function of Prandtl number only. Thus, it can be concluded that the ratio of the convection to conduction layer thicknesses beneath evaporative water surface is different from that of the solid wall case. The present results propose a new scaling relation for the convection and conduction layer thickness of the form,

$$z_*/z_o = C\,Pr^2 \tag{5.6}$$

where, C is a constant whose value for the present study is 11.5.

Adrian *et al.* (1986) experimentally determined a constant for plotting mean temperature profile normalized by the conduction layer thickness. They defined the constant as

$$\frac{\Delta\overline{T}}{\theta_0} = A\,\mathrm{Pr}^{1/4} \tag{5.7}$$

where $\Delta\overline{T}$ is the temperature difference between the bulk temperature and the average temperature in the conduction layer, θ_0 is the temperature scale in the conduction layer and Pr is the Prandtl number. They found that for water with $4.5 < Pr < 6$, $A = 3.49$ in wall bounded natural convection. In the present study, the value of A is found to be 5.68 and 6.04 for high and low heat flux cases, respectively. The higher values of A in case of evaporative water surface implies that the average temperature in the conduction layer relative to the bulk temperature and the temperature scale (θ_0) is lower compared to that for the solid wall case. This is likely due to cooler temperature at the water surface because of latent heat transfer (i.e. evaporation).

Previous studies on wall bounded natural convection have reported the depth dependency of the mean temperature. Kraichnan (1962) conducted a theoretical analysis of the thermal convection for various Prandtl numbers. He investigated the temperature in a region of fluid where turbulent heat and momentum transfer effects are larger than the viscous effects. For high Rayleigh numbers ($Ra \geq 10^5$), he proposed a relation of the form $T_{(z)} = Cz^{-n}$ for the fluid mean temperature. He considered three different regions; (i) region adjacent to the wall (i.e. conduction layer) where molecular conduction and viscosity dominates, (ii) intermediate region where eddy conductivity and molecular viscosity dominates and (iii) the bulk region where eddy conductivity and eddy viscosity dominates. From the theoretical analysis he found that for high Prandtl numbers ($Pr >$ 0.1), in the third region, where eddies transfer both heat and momentum to the bulk of the fluid, the temperature has $z^{-1/3}$ dependency. In the intermediate region that lies between the conduction layer and bulk region where eddy and viscous momentum transfer are of equal magnitude, the temperature varies as z^{-1}. In the conduction layer, the temperature

varies linearly with z. In Fig. 5.4 (b), the power law profiles representing the depth dependency of the present temperature profiles are also plotted. The plot shows that the temperature varies as $z^{-1/3}$ in the region $z/\delta \geq 10$ which correspond to the bulk region where the mean temperature approached the bulk value. In the intermediate region i.e. $1< z/\delta \leq 7$, z^{-1} dependency is observed. The temperature profiles in the conduction layer are linear. The present results are in agreement with the theoretical results of the Kraichnan (1962) and provide the first quantitative evidence of the existence of three regions beneath the evaporative water surface where the temperature exhibits different depth dependency which is similar to that observed in the wall bounded natural convection. The profiles in Fig. 5.4 (b) also provide an estimate of the intermediate layer thickness which is approximately 6δ. Priestley (1959) derived a mean temperature profile for turbulent free convection over a single heated surface and found a temperature dependency of $z^{-1/3}$ in the bulk region.

Near-interface region plays an important role in controlling the heat flux across the air-water interface. Therefore, an improved understanding of the thermal and flow dynamics in this region is important. The temperature structure near the interface is governed by the growth and destruction of the conductive boundary layer. The cool surface layer at the interface thickens the boundary layer with time and after a certain period it becomes unstable and destroys. This breaking of the boundary layer exposes the bulk warm water to the surface. This process does not happen in the entire plane at ones, but rather it is a random process and is shorter in duration and limited to the thin region near the interface. Howard (1963,1966) also explained the generation of thermals and breaking of the boundary layer phenomenon in his model. He argued that the diffusion

first results in the formation of the thermal boundary layer which gradually get thicken with time and destroyed by the convective flow after a certain time period. This process repeats again and again and termed as the cyclic destruction of the boundary layer. Because of the motions within the boundary layer, the temperature varies horizontally and with time (Volino and Smith 1999, Katsaros *et al.* 1977). Sparrow *et al.* (1970) observed thermals as rising columns of fluid which had a mushroom like appearance. They found that the heating rate had a decisive influence on the generation of thermals. An infrared imagery of the surface temperature field taken by Volino and Smith (1999) revealed great number of structures. They found that the colder regions on the surface were approximately 0.2 °C cooler than the local mean temperature and 2 °C cooler than the bulk fluid temperature. These regions correspond to the cold sheet like plumes plunging into the bulk fluid temperature. They argued that the plumes are regions where boundary layer fluid is falling, so the boundary layer is effectively thicker there which result in a large bulk to surface temperature difference. The present results found that the surface was 2.7 to 3.5 °C cooler than the bulk water temperature. Since the near-surface regions plays an important role in controlling the flow dynamics and heat flux, a detailed analysis of the temperature field in this region is important to improve our understanding of the physical processes in this region. The temperature profiles in the near-surface region ($z/\delta \leq 16$) for both cases are plotted in Fig. 5.5 (a) and 5.5 (b). Howard (1963,1966) derived theoretical equations for the conduction phase for constant boundary temperature and constant heat flux conditions. The conduction profiles for these conditions based on the modified equations in Katsaros *et al.* (1977) are given as;

$$T(z,t) - T_b = (T_s - T_b) erfc\left(\frac{z}{2(\alpha t)^{1/2}}\right) \tag{5.8}$$

for constant boundary temperature and

$$T(z,t) - T_b = \frac{2Q(\alpha t)^{1/2}}{k} ierfc\left(\frac{z}{2(\alpha t)^{1/2}}\right) \tag{5.9}$$

for constant heat flux conditions.

Where T_b is the bulk water temperature, T_s is the water surface temperature, z is the water depth, α is the thermal diffusivity, k is the thermal conductivity, Q is the surface heat flux and t is the time constant.

The conduction profiles based on equation (5.8) and (5.9) are also plotted in Fig. 5.5 for comparison. The plots show that both theoretical profiles agreed very well with the experimental data within the conduction layer for both heat flux conditions. Beneath the conduction layer, the theoretical profiles reached the bulk temperature around $z/\delta = 2$. This is an expected behavior of the theoretical profiles for the conduction phase as they only account for the conduction heat transfer in near-surface region. Comparison of the experimentally observed profiles with the theoretical ones beneath the conduction layer shows that in the intermediate region, the mean temperature is lower than that predicted by the theoretical profiles. However, in the bulk region, i.e. $z/\delta > 10$, both experimental and theoretical profiles have the same bulk values. This indicates that in the intermediate region, the thermal behavior cannot be predicted by the conduction phase theory. This is the region which is actively involved in the formation of cold falling sheets and their replacement by rising warm plumes from the bulk region. Katsaros *et al.* (1977) also observed the deviation of the theoretical conduction profiles from their experimental profiles. They however, found temperatures higher than the theoretical ones in this

region. They argued that the higher temperatures are due to the net upward advection of the warm fluid from the bulk to replace the cold falling sheets. However, they did not provide any quantitative evidence to support their hypothesis. The only consistency between the present results and those of Katsaros *et al.* (1977) in the intermediate region is that both deviate from the theoretical conduction profiles. The deviation from the theoretical behavior can be explained on the basis of the velocity field in this region. In physical units, the intermediate region lies within a depth 0.8 mm $< z <$ 6 mm for low heat flux case and 1.1 mm $< z <$ 8 mm for the high heat flux case. Bukhari and Siddiqui (2006) showed the vertical profiles of waterside horizontal and vertical turbulent velocities for the conditions identical to that in the present case. They observed an increase in the horizontal turbulent velocity within a depth of approximately 5 - 7 mm from the water surface which lies within the intermediate region. Their vertical turbulent velocity profiles showed a gradual decrease in velocity magnitude towards the surface, but for high heat flux case, within a depth of approximately 3 mm, the vertical turbulent velocity magnitude again started to increase. These results indicate that within the intermediate layer, the turbulence is relatively strong which implies enhanced mixing of warm and cold fluid parcels. Thus, the average temperature of the fluid in this region would be less than that when the fluid is considered to be stagnant with conduction heat transfer as the only mode, as assumed in the theoretical case. Thus, the cooler temperatures in the intermediate region in the present study suggest intense turbulent mixing in this region unlike the net warm upward advection as proposed by Katsaros *et al.* (1977).

5.8 Conclusions

In this experimental study the temperature field has been investigated in horizontal layer of water beneath an evaporating water surface using laser induced fluorescence technique. This technique enabled the first non-intrusive temperature measurements in the conduction layer within 40 μm from the water surface. Two-dimensional temperature field perpendicular to the water surface shows the cool skin layer immediately underneath the evaporative water surface whose thickness varied horizontally. It is also observed that the surface layer is thicker above the falling sheet and thinner above the rising plume. Vertical profiles of the mean temperature show the characteristic boundary layer distribution in the near surface region followed by an isothermal region in the bulk. The temperature profiles within the conduction layer and in the bulk region are found to be in good agreement with theoretical profiles and past experimental data. The temperature profiles showed the existence of three regions beneath the water surface with different depth dependency of the temperature in each region. In the conduction layer, the temperature varied linearly, in the intermediate region the temperature varied as z^{-1} and in the bulk region temperature varied as $z^{-1/3}$. These dependencies are in good agreement with that predicted theoretically for wall bounded natural convection. Relationship between the scales of conduction and convection layers for velocity and temperature for solid wall case are found to be valid for free surface case, however, the ratio of the convection and conduction layer length scales showed the opposite trend beneath air-water interface which is attributed to the evaporation. A new relationship for the length scales is proposed.

Case	High Heat flux	Low Heat flux
T_b (°C)	36	30.1
q''_{total} (W/m^2)	678	367
q''_s (W/m^2)	591	309
$z*$ (mm)	260	260
δ (mm)	1.1	0.8
w_* (mm/s)	5.1	4.0
w_0 (mm/s)	0.528	0.43
$\theta*$ (°C)	0.0286	0.02
θ_0 (°C)	0.277	0.186
$Re*$	1930	1300
Pr	4.56	5.25
Ra	1.8×10^7	1.28×10^7

Table 5.1: q''_{total}, total heat flux; q''_s, heat flux through the water surface; $z*$, the water depth; δ, conduction layer thickness; $w*$, the velocity scale in the outer layer; w_o, the velocity scale in the conduction layer; $\theta*$, the temperature scale in the outer layer; θ_o, the temperature scale in the conduction layer; $Re*$, the Reynolds number; Pr, the Prandtl number; Ra, Rayleigh number.

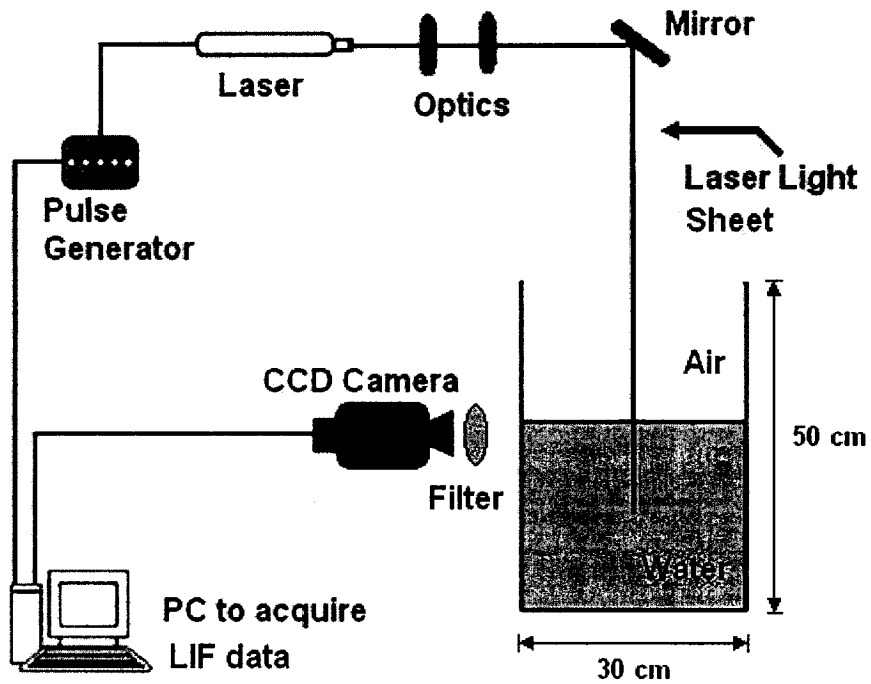

Fig. 5.1: Schematic of the experimental setup.

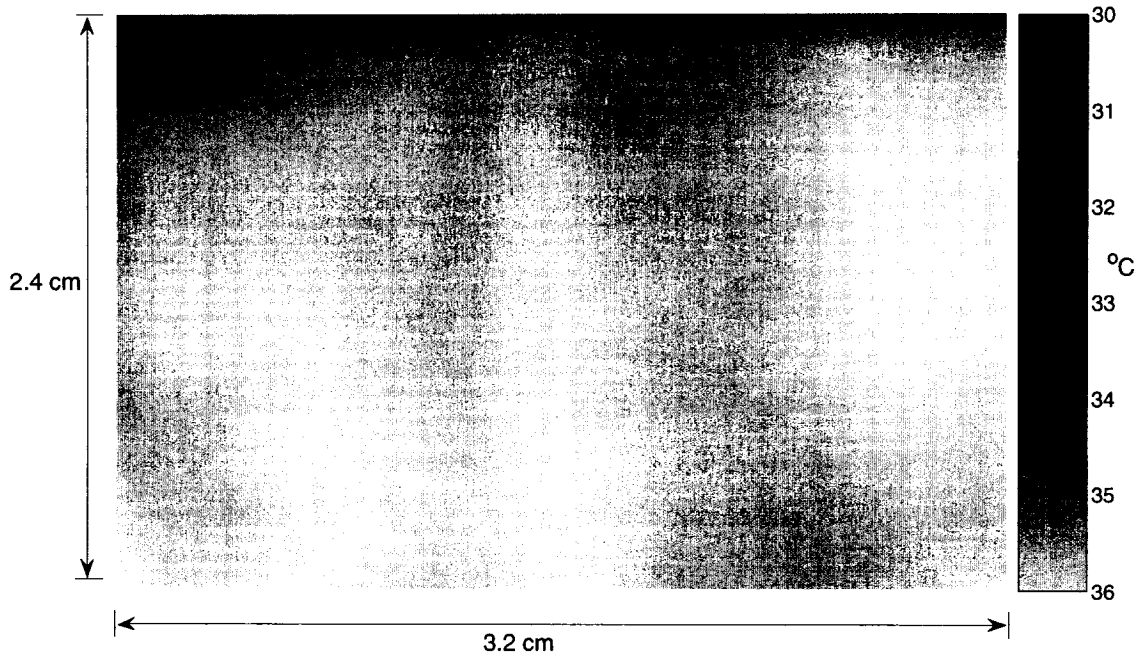

Fig. 5.2: Mean temperature field in a vertical plane at bulk water temperature of 36 °C.

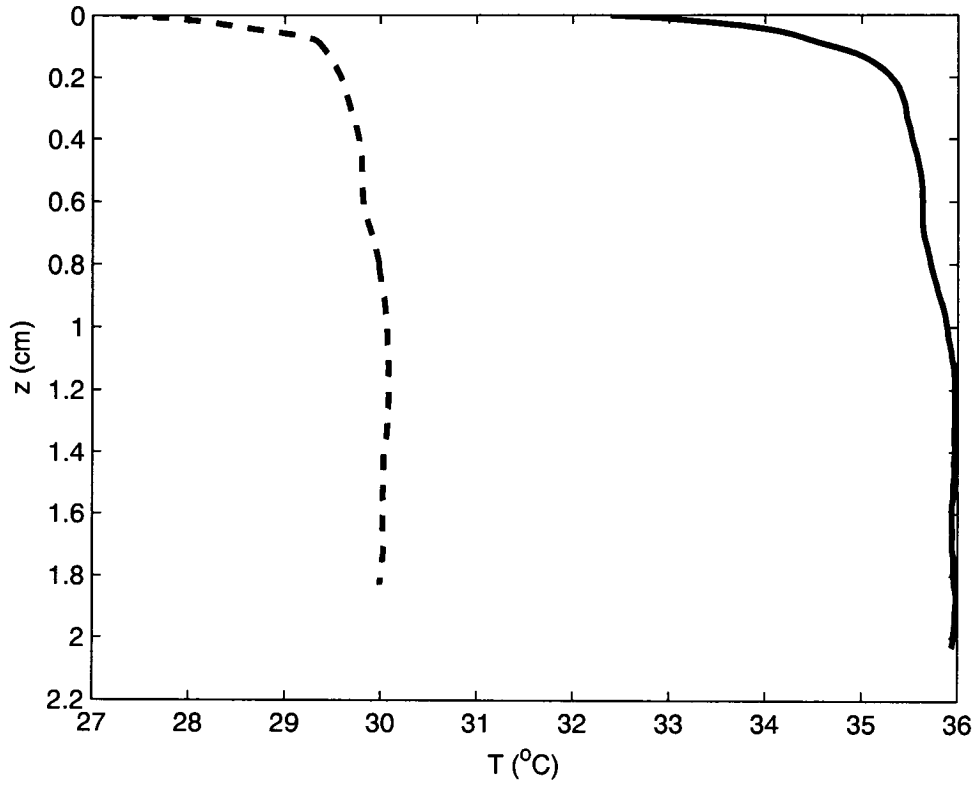

Fig. 5.3: Mean temperature profiles at bulk water temperatures of 36 °C (thick solid line) and 30 °C (thick dashed line) versus the depth (z).

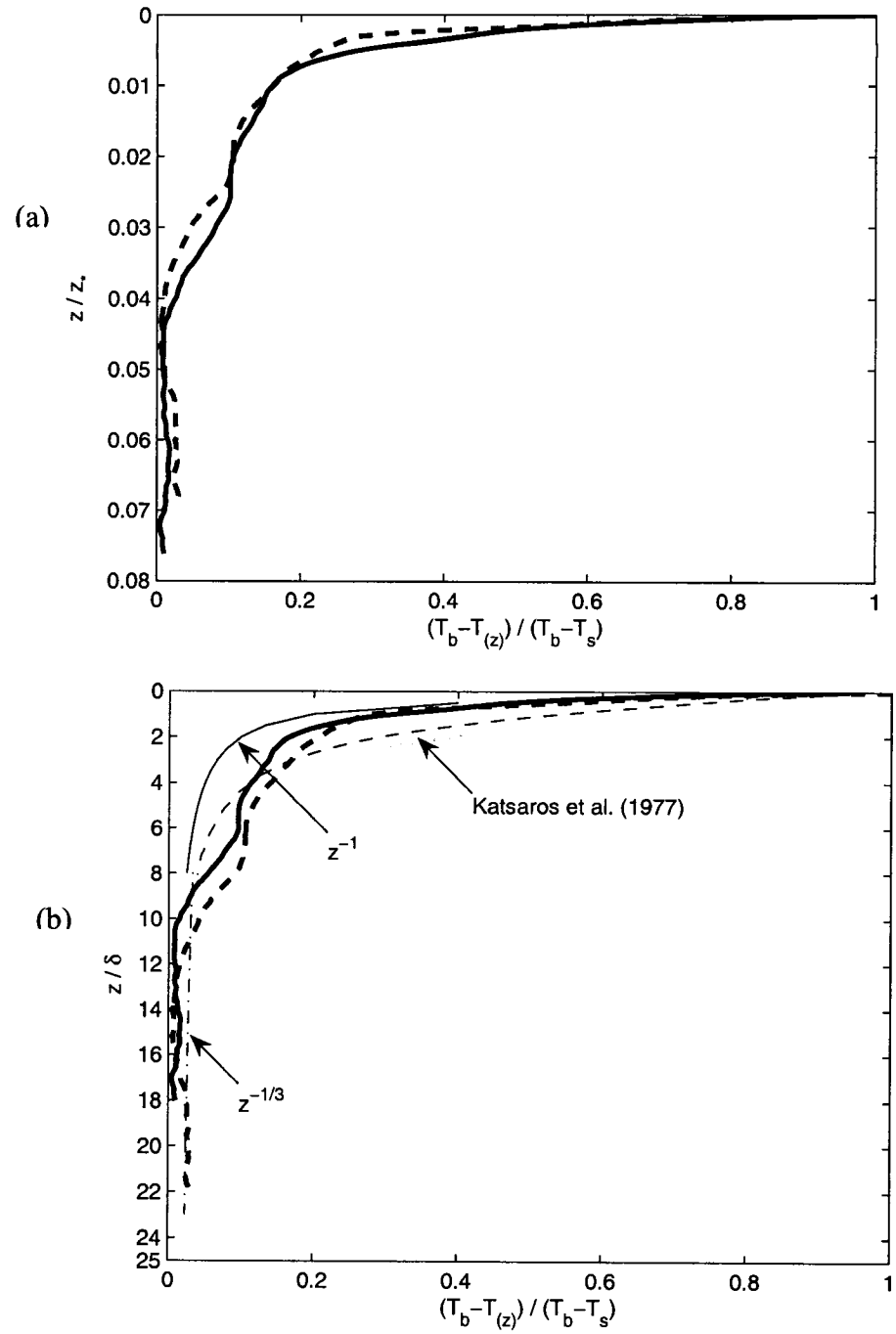

Fig. 5.4: Normalized mean temperature profiles at bulk water temperatures of 36 °C (thick solid line) and 30 °C (thick dashed line) versus depth normalized by (a) convective layer scaling (z/z_*), (b) conduction layer scaling (z/δ). In Fig. 5.4 (b), thin dashed-line represents the experimental data of Katsaros *et al.* (1977), thin solid line represents z^{-1} slope, thin dashed-dotted line represents $z^{-1/3}$ slope. [It should be noted that Katsaros *et al.* (1977) used the characteristic length scale twice the conduction layer thickness. Their data was rescaled based on the conduction layer thickness to plot in Fig. 5.4 (b)].

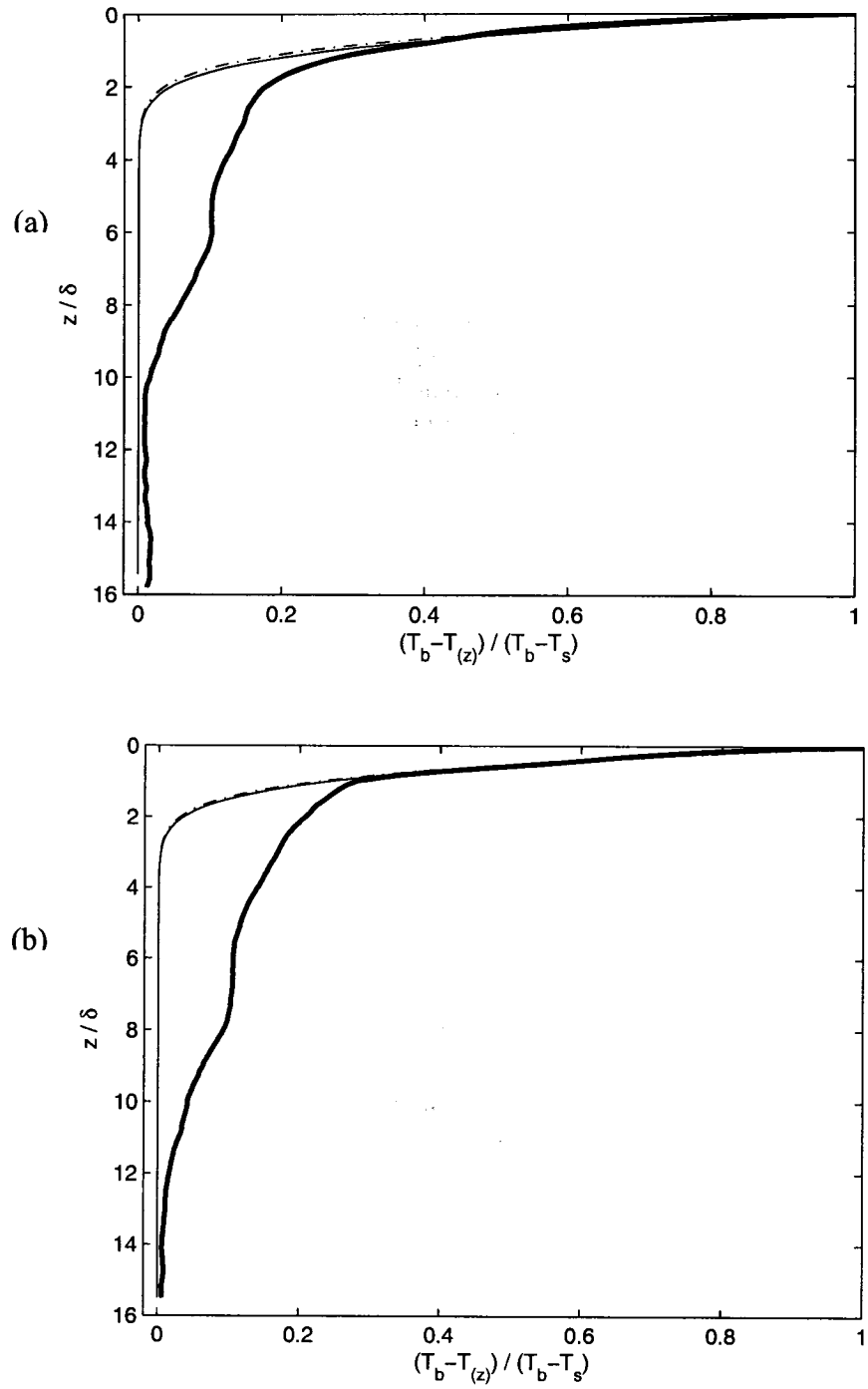

Fig. 5.5: Theoretical and experimental normalized temperature profiles versus z/δ (a) 36 °C and (b) 30 °C. Experimental temperature profile (thick solid line), theoretical temperature profiles based on constant temperature boundary condition (dash-dotted line), theoretical temperature profile based on constant heat flux boundary condition (thin solid line).

Chapter 6

An Experimental Study of the Airside Flow Structure during Natural Convection

6.1 Abstract

We report on an experimental study conducted to investigate the airside flow structure above an evaporative water surface during natural convection. Two-dimensional airside velocity fields were measured using PIV for three different surface heat flux conditions. Detailed analysis of the turbulent velocity fields shows a complex flow structure due the local interactions of fluid motions in vertical, horizontal and normal directions. The trends of turbulent intensity profiles on air and water sides are found similar. However, the airside turbulent intensities are approximately 20 times stronger than that on the waterside. The spectral analysis of the turbulent velocities showed the existence of two distinct power law regimes. In low wavenumber regime, the buoyancy subrange is observed with a slope of -3 whereas, in high wavenumber range, the inertial subrange with the classical slope of -5/3 is observed. It is also concluded that the instantaneous flow structure and evaporation rate measured at one location may not be the accurate representation of the instantaneous flow behavior in a relatively wider region and that the dynamics of strong near-surface physical mechanisms and their influence on the air-water heat and mass transfer rates should be adequately incorporated in the transport models to improve their accuracy.

6.2 Introduction

Natural convection is an important phenomenon in the coupled air-water system during which, the water surface undergoes evaporative cooling. The heat transfer from water to air occurs via two modes; sensible heat transfer due to the bulk air-water temperature difference and latent heat transfer due to evaporation. The air and water temperatures control the evaporation rate and the sensible heat transfer across the interface. In addition to this, the temperature difference also influences the air and water velocity fields, which in turn alter the heat transfer rate. In natural convection process, the cool and dense water parcels at the interface plunges into the deeper warm water, and the warm and humid air parcels at the interface rise and penetrate into the cool and dry air above. As the water evaporates, it diffuses upward through the air and at steady state this upward movement of humid air is balanced by a downward movement of dry air. The exchange of mass and heat across the air-water interface during natural convection is important in a wide range of applications from environmental to industrial. For example, the heat and mass exchange between the ocean and atmosphere has a significant impact on the global climate. From the industrial aspect, it is important in the HVAC and chemical process applications such as condensers, evaporators, bubbly flows and reactors. Despite its significance, the natural convection process across the air-water interface is not well understood. Very few studies have reported the waterside velocity and temperature measurements beneath an evaporating interface. Volino and Smith (1999) simultaneously measured the surface temperature and two-dimensional sub-surface velocity fields using infrared imagery and particle image velocimetry (PIV), respectively. The temperature field they observed was very complex showing different

scales of thermal structures that appear to be randomly located on the water surface. No strong correlation between the temperature field and the sub-surface velocity fields was observed. Flack *et al.* (2001) measured the surface temperature of water and sub-surface velocity using infrared imagery and laser Doppler velocimetry, respectively, for clean and surfactant-contaminated water surfaces. They observed that the near-surface turbulent intensities were higher beneath the clean surface as compared to the contaminated surface and that this difference decreased with the distance from the free surface. The surface temperature field showed that the surfactant dampens the small-scale thermal structures. Bukhari and Siddiqui (2006) experimentally investigated velocity fields beneath the air-water interface during natural convection using PIV, and presented a detailed analysis of the waterside turbulent structure. Their results indicate the three-dimensional nature of the waterside flow field that results in the formation of complex flow patterns. They also observed self similar behavior in the turbulent velocities for different cases. They also showed the existence of the buoyancy subrange in the spectra of the waterside turbulent velocities, where the turbulent kinetic energy is removed by working against buoyancy. The only detailed analysis of the temperature field in the thermal boundary layer beneath the water surface during natural convection is reported by Katsaros *et al.* (1977). They observed that the mean temperature profile in the boundary layer was highly nonlinear and away from the surface the temperature variations were organized showing an almost constant temperature. From the data and visualization of the flow, they deduced that the cold fluctuations were due to cold water plunging down from the boundary layer just under the surface. They argued that the

thermal boundary layer acts as a source of the fluid for the cold sheets, and warm water enters the boundary layer from below by advection.

The research focusing on the investigation of the airside flow and thermal structure above evaporative water surface particularly in the near-surface region is almost non-existent. As far as we know, there are only two numerical studies on the airside flow field; however, no experimental study has been reported on the airside velocity measurements in the near surface region. Bukhari and Siddiqui (2007) numerically investigated the airside and waterside flow behavior in a coupled air-water system undergoing natural convection. They simulated the bulk flow fields for unstable and stable thermal stratifications and neutral condition. They found that during unstable thermal stratification, the magnitude of the root-mean-square (r.m.s.) airside velocities is more than an order of magnitude higher than the r.m.s. waterside velocities. They concluded that the bulk air and water temperature difference is important in controlling the magnitudes of the velocity fields. They however, did not investigate the turbulent structure. Sparrow and Nunez (1988) numerically simulated the airflow above an evaporative water surface in a partially filled open-topped vertical circular tube whose inside diameter varied from 3.8 cm to 6.10 cm. They considered two cases, one with the insulation around the tube and the other without insulation. They studied the bulk airflow patterns in the air column above the water surface and in the ambient air above the tube. For the case without insulation, they found that the air from the ambient entered the tube in an annular region adjacent to the wall and left from the middle. While for the case with insulation, they found the reverse trend. That is, the air entered the tube in the middle and left from the annular region adjacent to the wall. They argued that this reversal reflects

the rearrangement of the buoyancy field caused by the vertical upward increase in temperature at the tube walls.

The natural convection in air bounded by solid horizontal walls has been studied in the past by many researchers for example, Deardorff and Willis (1967), Goldstein and Chu (1969), Thomas and Townsend (1957). The natural convection process through an evaporative water surface is not identical to that above a heated wall. One major difference is the boundary condition which is no-slip for the solid wall case and slip for the water surface. Furthermore, the moisture transfer on the airside also influences the airside flow dynamics, which is not present in case of solid wall.

Better understanding of airflow structure above an evaporative water surface is very important in environmental and global applications. The interaction between ocean and atmosphere has a major influence on atmospheric circulation and air-sea heat and mass exchange. The meteorological approaches for atmospheric circulations has been modeled using different approximations such as homogeneously stratified atmosphere with a constant potential temperature gradient, which gives qualitative insight into the general effects of stratification. However turbulence theories and direct numerical simulations generally use the Boussineq approximation or only model the large scales by assuming that they are completely stratified. Majority of the theories consider that all the regions are isotropic in which horizontal structures are dominated by energy fluxes, while vertical structures are dominated by buoyancy fluxes (Lovejoy *et al* . 2005). The near-surface processes which influence the air-sea heat and mass transfer are not well understood and hence are not properly incorporated into the available climatic models. In order to obtain accurate estimates of air-water heat and mass exchange during natural

convection, a better understanding of the near-surface characteristics of airside velocity fields, the energy and buoyancy fluxes, the structure of turbulence, dynamics of turbulent motions and their impact on the exchange processes is necessary. As mentioned above, most of the previous laboratory studies were focused on the investigation of waterside flow characteristics during natural convection and no significant attention has been paid to investigate the airside flow structure above the water surface. The scarcity of the studies and lack of understanding about the airside flow structure above the water surface motivated us to conduct an experimental study to investigate the airside flow structure in detail.

6.3 Experimental Setup

Experiments were conducted in a glass tank 60 cm long, 30 cm wide and 50 cm deep. The tank was filled with clean tap water up to a depth of 26 cm. During experiments the tank top was left open to allow evaporation from the water surface. The airside velocity field was measured using particle image velocimetry (PIV). For PIV measurements, the flow under investigation must be seeded with tiny particles. Since the tank top has to be left open, the air inside the tank and in the entire surrounding area must have homogeneous seeding so that the seed particle density within the measurement region should remain uniform. Thus, if the tank is placed in a room then the entire room must be seeded. This could damage the instrumentation and affect the image quality due to the seed deposition on the camera lens. Thus, to overcome this issue, the glass tank was placed inside another large glass tank (see Fig. 6.1). The large tank is 45 cm wide, 90 cm high and 300 cm long. Prior to the experimental runs, the air inside the large tank was seeded and the tank was completely sealed. Vegetable oil mist with average diameter of

0.25 μm was used as the seed particles. The airside velocity fields were measured for three experimental conditions that correspond to the bulk water temperatures of 36, 30 and 23 °C. The surrounding bulk air temperature inside the room was 23 °C during all experimental runs. The bulk water temperatures of 36 and 30 °C correspond to the situation when the water is warmer than the air, and both air and water flow fields are unstably stratified. However, the bulk water temperature of 23 °C corresponds to the neutral case in which both bulk air and water are at the same temperature. Hereinafter, the cases at the bulk water temperatures of 36 °C, 30 °C and 23 °C are referred as high, medium and low heat flux cases, respectively.

The PIV velocity measurements were made in a plane perpendicular to the water surface at the mid-tank location along the longer tank dimension as shown in Fig. 6.1. A Continuum Minilite 25 mJ Nd:YAG laser was used as a light source for the PIV measurements. A CCD camera (JAI CV-M2) with the resolution of 1600 × 1200 pixels was used to image the flow. The field of view of the camera was set equal to 7 cm horizontal and 9 cm vertical. The vertical position of the camera was set in a way that the lower edge of the image coincides with the water surface. The camera was connected to a PC equipped with a frame grabber (DVR Express, IO Industries, London, ON, Canada) that acquired 8-bit images at a rate of 30 Hz. A four-channel digital delay generator (555-4C, Berkeley Nucleonics Corporation, San Rafael CA) was used to control the timing of the laser light pulses. For each experimental run, the data were acquired for 5 minutes i.e. 9000 images at a rate of 30 Hz. During experiments, the temperature was measured using thermistors (TJ 72-44033, Omega Engineering, Inc.) with an accuracy of 0.1 °C, at seven different heights that varied from 7.5 mm to 11.5 cm above the interface. Thermistors

were placed in the corner of the tank to avoid any disturbance to the flow in the measurement plane. The waterside bulk temperature was measured by placing a thermistor at a depth of 5.5 cm from the interface. Thermistors were calibrated using Traceable Digital Thermometer (Control Company USA) which has a resolution of 0.001 °C with ± 0.05 °C accuracy. The relative humidity was measured at heights of 5.5 and 37.5 cm from the water surface using humidity probes (HX92AV-D, Omega Engineering, Inc.) with an accuracy of ±2.5%. The temperature and relative humidity data were acquired via a 16-channel data acquisition card (PCI-6036E, National Instruments) using the LabView data acquisition software.

As the large tank was sealed, therefore, it was expected that the humidity level inside the tank would rise. Therefore, it was important to check the variations in the bulk relative humidity and the air temperature inside the large tank during the data acquisition. For this purpose, the bulk temperature and relative humidity were also recorded in the large tank at a location 100 cm from the middle of the small tank and 60 cm above the water surface. It was found that from the start to the end of the data acquisition, the bulk relative humidity was changed by 12.8 % for the high heat flux case and by 5.4 % for the medium heat flux case. The maximum bulk relative humidity in the large tank at the end of the data acquisition was observed to be 41.2 % for the high heat flux case which is close the normal conditions and well below the saturation state. The bulk air temperature was changed by 0.6 °C for the high heat flux case and by 0.2 °C for the medium heat flux case. For the neutral case, no appreciable difference in the bulk relative humidity and bulk air temperature was observed.

The PIV technique computes velocity vectors by cross-correlating the interrogation region in the first image with the corresponding search region in the second image of an image pair. In the present study, the size of the interrogation region was set equal to 24 × 24 pixels and the size of the search region was set equal to 48 × 48 pixels. A 50 % window overlap was used in order to increase the nominal resolution of the velocity field to 12 × 12 pixels. This resulted in the spatial resolution of 0.7 × 0.7 mm of the velocity field. For all cases, the velocity vectors nearest to the surface were located 1.4 mm above the air-water interface. Due to the difference in velocity magnitudes for all cases, a constant time separation between the two images of an image pair will give different particle shifts for different cases. That is, smaller particle shift for small velocity magnitude. Very small particle shift increases uncertainty in the velocity measurements. Thus, the time separation between the two images of an image pair was varied in each case, in order to obtain reasonable particle shifts (Appendix C). A scheme was used to identify the spurious velocity vectors and then correct them using a local median test (Siddiqui *et al.* 2001). Typically, 1 % of the velocity vectors were spurious. The uncertainty in the velocity measurements was estimated to be less than 9 % (Appendix A).

The total heat loss per unit area (q''_{total}) from the tank (i.e. loss through walls and from the surface of water) was computed in the same setup under similar experimental conditions in a separate set of experiments. The rate of decrease of the bulk water temperature, dT_b/dt, was measured using a thermistor. The data were acquired for 15 minutes for each case. The q''_{total} was computed using the relation,

$$q''_{total} = \rho \times c_p \times d \times (dT_b/dt) \tag{6.1}$$

where, d is the water depth in the small tank and ρ is the density of water. To compute the heat loss by conduction through the side walls, the tank was completely filled up to the rim and covered by the glass lid of the same thickness as the side and bottom walls. The rate of decrease of the bulk water temperature was recorded at the mid tank location. The heat loss through the sidewalls, lid and bottom of the tank was computed using the following relation.

$$q''_w = \rho \times c_p \left[\frac{lbd}{2(lb + bd + ld)} \right] \frac{dT_b}{dt} \tag{6.2}$$

where l, b, and d are the length, breadth and depth of the tank (Katsaros *et al.* 1977). The surface heat flux (q''_s) was computed by subtracting the heat flux through the walls from the total heat loss of water (q''_{total}).The values of the total and surface heat fluxes for all cases are given in the Table 6.1.

6.4 Results and Discussion

The airside root-mean-square (r.m.s.) horizontal turbulent velocity is plotted in Fig. 6.2 (a) as a function of height for the three cases. The plot shows that the magnitude of horizontal turbulent velocity increases with the surface heat flux. A sharp increase in the horizontal turbulent velocity was observed within a 5 mm thick layer immediately above the water surface. In this layer, the horizontal velocity is increased by 70 – 100 %. With a further increase in height, the horizontal velocity was first decreased and then slightly increased. The shapes of the velocity profiles were also found to be similar for different heat flux conditions. The waterside turbulent properties under similar conditions are presented in Bukhari and Siddiqui (2006). The waterside r.m.s. horizontal turbulent

velocities from Bukhari and Siddiqui (2006) are plotted in Fig. 6.2 (b) for comparison. The plot shows that the waterside horizontal turbulent velocity has a trend similar to the airside horizontal velocity. That is, a sharp increase in the horizontal velocity immediately below the water surface within a 5 mm thick layer followed by a gradual decrease and then increase in the velocity magnitude. Comparison of the velocity magnitudes on both sides of the interface shows that the airside horizontal turbulent velocities are more than an order of magnitude (approximately 20 times) stronger than the waterside turbulent velocities, for the similar experimental conditions. The airside r.m.s. vertical turbulent velocity is plotted in Fig. 6.3 (a) as a function of depth for the three cases. The plot shows that the magnitude of the vertical turbulent velocity increases with an increase in the surface heat flux. The plot also shows that the vertical velocity increased sharply with the distance from the water surface to a height of 2 - 4 cm and then decreased slightly with a further increase in height. A similar trend was observed for the waterside r.m.s. vertical turbulent velocity plotted in Fig. 6.3 (b) from Bukhari and Siddiqui (2006). The airside vertical turbulent velocities are found to be an order of magnitude (approximately 20 times) larger than the corresponding waterside velocities, similar to the horizontal turbulent velocities. Furthermore, the shapes of the vertical profiles are also similar for different cases. Comparison of the horizontal and vertical turbulent velocities shows that for any given case except very close to the surface, the magnitude of the vertical turbulent velocity is larger than the horizontal turbulent velocity. The large magnitude of the vertical turbulent velocity is due to the strong buoyancy fluxes in the vertical direction and also due to the reason that away from the surface, the vertical velocity is more influenced by the rising plumes and falling sheets of

the fluid. Another interesting observation is that the ratio of the airside to waterside velocities remains approximately the same for both horizontal and vertical turbulent velocities for all cases. Bukhari and Siddiqui (2007) numerically simulated the bulk flow on air and water sides during natural convection and found that for unstably stratified condition, the r.m.s. airside velocity is more than an order of magnitude larger than the r.m.s. waterside velocity, which is in agreement with the present results. For neutral condition, they did not observe large airside velocity magnitudes and attributed this to the limitations of the numerical model used to simulate airside flow. Their r.m.s. velocities however, were based on the velocity fields in the entire computational domains on air and water sides.

The results in Figs. 6.2 (a) and 6.3 (a) provide the first experimental observation of the airside near-surface turbulent intensities during natural convection. The results in Figs. 6.2 and 6.3 also provide the first detailed quantitative comparison of the magnitudes and structure of airside and waterside turbulent velocity fields during natural convection. The results show that although the turbulent structure is similar in both flow regimes but the turbulent motions on the airside are significantly stronger than the waterside. The trend observed in the r.m.s. horizontal and vertical velocities are similar to that observed in a fluid bounded by solid walls. Adrian *et al.* (1986) studied the natural convection in water bounded between two horizontal walls with the heat addition from the bottom wall. They observed a sharp increase in the r.m.s. horizontal turbulent velocity in the layer adjacent to the wall, followed by a slight decrease in the velocity magnitude and then it remained almost constant up to the middle region between the two walls. Their vertical turbulent velocity profile was approximately symmetric about the mid-plane, increased

monotonically with distance from the wall to a certain height and then remained constant up to the mid-plane. Flack *et al.* (2001) also observed similar trend in the waterside turbulent velocities beneath an evaporating surface. They observed maximum horizontal turbulent velocity close to the surface, which decreased with depth.

Figs. 6.2 and 6.3 show that the turbulent velocity profiles are self similar for different experimental conditions and therefore, can be represented by appropriate scaling parameters. Adrian *et al.* (1986) proposed scaling parameters for the fluid bounded by the solid walls undergoing thermal convection when heated from below. Bukhari and Siddiqui (2006) have shown that this scaling is also applicable to the flow beneath evaporative water surface during natural convection. Due to the similar flow structures on air and water sides, the same scaling is expected to be appropriate for the airside flow as well. The velocity scale is defined as,

$$w_* = (\beta g Q_o z_*)^{1/3} \tag{6.3}$$

where, β is the thermal coefficient of expansion, g is the acceleration due to gravity, z_*, is the convective length scale defined as the thickness of the convection layer, and Q_o is the kinematic heat flux defined as,

$$Q_o = \frac{q_s''}{\rho c_p} \tag{6.4}$$

where, q_s'' is the surface heat flux, ρ is the density, and c_p is the specific heat (Adrian *et al.* 1986). Adrian *et al.* (1986) argued that except for very thin layer adjacent to the wall where conduction is dominant, the heat transfer mode in the rest of the fluid is convection. Thus, in their case, i.e. for fluid bounded by two walls, z_* was defined as the distance between the two walls. For free surface case, where the water is bound from the

top by free surface and from the bottom by solid wall, z_* is set equal to the water depth (Flack *et al.* 2001, Bukhari and Siddiqui 2006). For the airside, these definitions of z_* are not appropriate as the air is bounded by the free surface from bottom but unbounded from the top as the tank top was left open. In such situation, it is difficult to estimate the true depth of the convection layer as the upper edge of the convection layer extends to the height where the heat flux is almost negligible. However, as an approximation, it is assumed that in the present setup, the convection layer is mainly confined within the airside of the small tank. Thus, the value of z_* is set equal to the distance from the water surface to the top of the small tank, i.e. $z_* = 24$ cm. Since z_* is a constant value, therefore, by changing the z_* value, the values of w_* will be changed but the relative difference between the w_* values for different cases will remain the same. The values of w_* and Q_o for the three cases are presented in Table 6.1. The results show that w_* for airside is 30 to 36 times larger than that for the waterside. The velocity scale w_* is a measure of the large-scale turbulent convective motions. The above results based on the surface heat flux and physical parameters show that the turbulent motions on the airside are more than an order of magnitude stronger than that on the waterside, which is also confirmed by the turbulent velocity data in Figs. 6.2 and 6.3.

Normalized r.m.s. horizontal and vertical turbulent velocities on air and water sides are plotted in Fig. 6.4 (a) and 6.4 (b), respectively, versus the normalized depth. The plots show that the airside data collapsed into a relatively narrow band indicating that this scaling is also applicable to the airside data. The Fig. 6.4 (a) shows that for $z/z_* > 0.02$, the variations in r.m.s. horizontal turbulent velocities are relatively small. For $z/z_* < 0.02$, a sharp decrease in the airside horizontal turbulent velocity towards the air-water

interface is observed. The results also show that in the region $z/z_* < 0.02$, the airside horizontal turbulent velocity decreased as $z^{1/2}$. The normalized profiles of r.m.s. vertical turbulent velocity (Fig. 6.4 (b)) also show a sharp decrease in velocity in the region $z/z_* < 0.1$ on both air and water sides. The plot shows that in the region $z/z_* < 0.05$, the vertical turbulent velocity on the air and water sides decreased as z. Comparison of the airside and waterside velocities show that in relation to their respective convective velocity scales, the waterside turbulent velocities are relatively stronger than the airside. An interesting feature observed in Fig. 6.4 (b) is that for the high heat flux case (i.e. bulk water temperature of 36 °C), the behavior of the vertical turbulent velocity in the near-surface region is different from the medium and low heat flux cases. The plot shows that for medium and low heat flux cases, the magnitude of vertical velocity continuously decreased towards the air-water interface. This is an expected behavior as the vertical velocity fluctuations must be zero at the interface. However, for the higher heat flux case, the plot shows that the vertical turbulent velocity decreased towards the interface up to certain depth and then started to increase as it approached close to the interface. This behavior is observed in vertical turbulent velocity on both air and water sides. Since the airside and waterside velocities were measured in different sets of experiments at different times, the consistent trend in both velocity fields indicates that this trend is not due to some measurement error but rather related to some physical process in the flow at this condition. Obviously, at the interface, the vertical velocity fluctuations will become zero to satisfy the boundary condition. This unusual trend at the high heat flux was further investigated and discussed below.

During natural convection, the water surface cools down primarily due to evaporation which constitutes more than 80 % of the surface heat flux (Volino and Smith 1999, Katsaros *et al.* 1977, Bukhari and Siddiqui 2006). As the horizontal velocities are not zero at the interface, the cold water appears to converge along lines (Volino and Smith 1999, Flack *et al.* 2001), and then plunges into deeper water as falling sheets (Spangenberg and Rowland 1961). This cold water is replaced by the rising plumes of warm water from underneath. The infrared images of the surface temperature in Volino and Smith (1999) and Flack *et al.* (2001) show that the warm water rises to the surface in between the cold lines. Thus, at the surface, water moves horizontally between the rising plumes and falling sheets. That is, from the warm regions towards the cold lines. Volino and Smith (1999) showed that at higher heat flux, the surface temperature variations are large and the cold lines are closer to each other compared to the low heat flux case. The surface temperature field appeared to be more vibrant with fine scale thermal signatures at the higher heat flux. Volino and Smith (1999) also showed that the surface patterns for the high heat case changed rapidly with time. Katsaros *et al.* (1977) proposed a conceptual model for the thermal boundary layer beneath the air-water interface during natural convection based on the comparison of their measured temperature profiles with the theoretical conduction profiles. According to this model, there is a thin layer at the water surface where the heat is transferred due to molecular diffusion. Beneath this layer, they proposed another layer "Thermal source layer" that acts as a source for the cold water to produce falling sheets. They argued that within this layer the cold water is replaced by the rising warm water that results in a net upward warm advection into this

region. Their argument is based on the observation of higher water temperature in this region compared to the theoretical temperature profile.

We conducted a detailed investigation of the flow behavior on both air and water sides during natural convection. The high-resolution velocity measurements allowed us to study the turbulent flow structure in the near-interfacial region on both sides. In Bukhari and Siddiqui (2006), we have presented the turbulent velocity fields beneath the water surface which showed that the turbulent flow structure is complex due to different flow interactions. It was also observed that the water undergoes local mixing at different depths. The issue of increase in r.m.s. vertical velocity near the surface was not discussed in Bukhari and Siddiqui (2006) as this trend was not very prominent in the waterside data. The deviation in the r.m.s. vertical velocity on the airside is more prominent and is observed in a much thicker layer adjacent to the interface than that on the waterside. Furthermore, the spatial resolution of the airside velocity fields presented here is relatively higher than that of the waterside velocity fields. Therefore, a detailed analysis of the airside turbulent velocity fields had been conducted, to identify the cause of the observed trend. The analysis showed that similar to the waterside, the airside turbulent velocity fields are also comprised of complex flow patterns. The complexity and dynamics increased with an increase in the surface heat flux. Few turbulent velocity fields for the high heat flux case are plotted in Fig. 6.5 to illustrate the dynamics of the airside turbulent velocity field. The strong near-surface vortices are prominent in Fig. 6.5 (a). The plot shows the warm air rising from the surface is mixed locally with the relatively cold air from above. The local mixing is observed at different heights. The middle right portion of the plot shows a small region with almost negligible velocities

and the flow from left passes around this region rather than passing through it. This region indicates the presence of flow in the direction normal to the measurement plane. Fig. 6.5 (b) shows descending flow of cold air from above in the upper portion of the plot. The lower portion shows the rise of warm air mass from the interface. The plot shows that the interaction between the rising and falling air masses created a region of local mixing near the surface. The plot in Fig. 6.5 (c) shows two strong vortices and one relatively weak vortex immediately above the surface within the measurement region. Vortices at other heights are also visible in the plot. The plots in Fig. 6.5 illustrate the complex dynamics of the airside flow field above the evaporative water surface. Detailed inspection of the airside velocity fields for the high heat flux case showed the overall trend similar to that depicted in Fig. 6.5. That is, strong locally-generated vortices are present immediately above the interface, which cause intense local mixing. Thus, it can be argued that the increase in r.m.s. vertical velocity in the near-surface region for the high heat flux case is due to the presence of these vortices. As the thickness of this enhanced vertical velocity layer is higher on the airside, it can be further argued that for the similar surface heat fluxes, the near-surface vortices on the airside are larger in size compared to that on the waterside. The velocity fields also show that in the near-surface region, the strongest horizontal motions are observed few millimeters above the interface which is also consistent with the results in Fig. 6.3 (a). Although the increasing trend in the near-surface vertical velocity is very prominent at high heat flux, a slight indication of this trend is also observed in the r.m.s. airside vertical velocity data nearest to the surface for the medium heat flux case (see Fig. 6.4 (b)). This indicates that the near-surface vortices at lower heat fluxes are relatively weak, smaller in size and restricted to a

relatively thin layer adjacent to the surface. Higher resolution velocity measurements immediately adjacent to the interface are required to further explore this issue.

Based on the analysis of turbulent velocity fields on air and water sides, we present an improved description of flow dynamics on both sides of the air-water interface during natural convection. According to this description, the turbulent flow structure is much more complex than the simplistic mixing model of Katsaros *et al.* (1977). The present results show that in the bulk region, the rising plumes of warm fluid and the falling sheets of cold fluid do not travel in pure vertical direction. Instead, at different vertical locations, they undergoes a variety of interactions that include, interaction of rising plumes and falling sheets, interaction of vertical and horizontal motions, and interaction of falling sheet or rising plume with the flow in the normal direction. These flow interactions resulted in the formation of local vortices which cause local fluid mixing. Thus, a sheet of fluid after its formation is distorted or deformed within a short distance due to its interaction with other fluid parcels. New sheets are formed due to this interaction with new orientations; however, they again get distorted within a short distance. In the near-surface region, strong vortices are formed which cause intense mixing in this region. Thus, the cold water at the surface that collects along the lines undergoes mixing within few millimeters from the surface as it plunges into the water body. As a result, the falling sheets lost their orientation. Thus, the dynamics of the flow changes significantly within few millimeters from the interface. This could be the reason why Volino and Smith (1999) who conducted simultaneous measurements of the surface temperature and sub-surface velocity fields at a depth of 2 mm from the surface, did not observe strong correlation between the surface temperature field and sub-surface velocity

field. The intense mixing in the near-surface region also results in an increase in the temperature within this layer compared to the case when the fluid is stagnant. Thus, the higher temperatures observed by Katsaros *et al.* (1977) in the near-surface region could be due to this mixing. Thus, it can be argued that the "thermal source layer" defined by Katsaros *et al.* (1977) is in fact the layer comprised of strong near-surface vortices that enhance mixing.

The turbulent velocity fields on both air and water sides show that during natural convection, turbulent structures exist over a wide range of scales. Bukhari and Siddiqui (2006) presented a detailed spectral analysis of the length and time scales of the turbulent motions for the waterside flow field during natural convection. Their results provided the first evidence of the existence of the buoyancy subrange beneath air-water interface during natural convection. They observed buoyancy subrange in the spectra of the horizontal velocity at all depths. However, for the vertical velocity, no buoyancy subrange was observed in the near-surface region for the higher heat flux. In this paper, we present the spectral analysis of the airside turbulent velocity field. The one-dimensional wavenumber spectrum was computed in the horizontal direction at all depths in each velocity field and then averaged at each depth. The normalized wavenumber spectra of the horizontal and vertical turbulent velocities for the three heat flux cases at a height of 6.2 cm from the interface (i.e. in the bulk region) are presented in Figs. 6.6 (a) and 6.6 (b), respectively. The spectra of both horizontal and vertical turbulent velocities at all conditions show the existence of two distinct power law regimes. In the large-scale or low wavenumber regime (140 rad $m^{-1} < k < 500$ rad m^{-1}), the spectra exhibit a steeper slope of -3 that correspond to the buoyancy subrange.

Whereas, in the small-scale or higher wavenumber regime, (600 rad m $^{-1}$ < k < 3000 rad m^{-1}), the inertial subrange is observed with the classical slope of -5/3. The buoyancy subrange exists within the inertial subrange and within this subrange the turbulent kinetic energy is removed from the turbulent scales by working against the buoyancy forces. The local rate of energy transfer within this subrange is higher and the spectrum exhibits a steeper slope of -3 (Turner 1973). The plots show that relatively larger scales are involved in working against the buoyancy forces. These scales are responsible for the energy extraction and interaction with the buoyancy forces and are almost same for different heat flux conditions.

The normalized wavenumber spectra of airside horizontal and vertical velocities at a height of 2 mm (i.e. close to the interface) are plotted in Figs. 6.7 (a) and 6.7 (b), respectively. As shown in Fig. 6.7 (a), the buoyancy subrange is observed in the horizontal velocity spectra at medium and low heat fluxes. However, at the higher heat flux, the buoyancy subrange was not manifested and the inertial subrange covered most of the wavenumber range in the spectrum. In the vertical velocity spectra (Fig. 6.7 (b)), buoyancy subrange is observed for the medium and low heat flux cases, however, the inertial subrange is not well defined for the low heat flux case. For the high heat flux case, the inertial subrange was observed in the high wavenumber range, but in the low wavenumber range buoyancy subrange was not observed and the slope of spectrum in this wavenumber range was relatively very small. Bukhari and Siddiqui (2006) presented the wavenumber spectra at a depth of 2.5 mm from the water surface. They observed buoyancy subrange in all spectra at this depth except for the vertical velocity spectrum at the high heat flux. They argued that in the near-surface region, the vertical turbulent

motions were not strong enough to work against the buoyancy forces as a result the buoyancy subrange was not manifested in the spectrum. They also observe smaller slope in the spectrum in the lower wavenumber range. Thus, it can be concluded that for the high heat flux case at this height, the horizontal and vertical turbulent motions on the airside are relatively weak with respect to the buoyancy forces.

The wavenumber spectra in Fig. 6.7 at a height of 2 mm from the surface lies within the layer of large vertical velocity fluctuations for the high heat flux case. Thus, the trend of the horizontal and vertical velocity spectra for the high heat flux case would provide some insight into the dynamical behavior within the layer where strong vortices and intense mixing are observed. The spectra show that the horizontal turbulent motions at smaller scales are relatively stronger whereas, the vertical turbulent motions are significantly stronger over the entire wavenumber range in relation to the characteristic velocity scale. The wavenumber spectrum of the vertical velocity also shows that in the wavenumber range that correspond to the buoyancy subrange at greater depths (i.e. 140 rad $m^{-1} < k < 500$ rad m^{-1}), the spectrum exhibits a slope of -1. The existence of the third subrange where the spectra exhibits -1 slopes implies that the energy transfer mechanism in this range is different from the other two ranges. The small slope in this range indicates that the energy transfer at these scales is significantly slower than the buoyancy and inertial subranges. In this range, the vertical turbulent motions are too weak to work against the buoyancy forces and, the dissipation rate is not the controlling parameter for the energy transfer.

The absence of the buoyancy subrange for the high heat flux case was observed only in the region very close to the interface. At greater heights (5 mm and above), the

buoyancy subrange was manifested in both horizontal and vertical velocity spectra for the high heat flux case. For the two lower heat flux cases, the buoyancy subrange was observed at all measured depths. However, the vertical velocity spectrum for the medium heat flux case at a height of 2 mm (Fig. 6.7 (b)) shows that the range of wavenumbers associated with the buoyancy subrange is reduced towards the lower wavenumbers and the buoyancy and inertial subranges are separated by a third subrange with the slope of approximately -1. This subrange is similar to that observed in the vertical velocity spectrum for the high heat flux case at the same height. Thus, the physical behavior of the near-surface turbulent motions can be described as follows. When the buoyancy flux is weak and turbulence is relatively strong, a relatively wider range of large-scale turbulent motions work against the buoyancy forces. As the heat flux increases (i.e. an increase in the buoyancy flux), this range reduces and only larger-scale energetic turbulent motions work against the buoyancy forces. That is, the turbulent motions that were previously strong enough to work against buoyancy forces are now relatively weak because the increase in turbulent intensity is relatively small compared to the increase in the buoyancy flux. These weak motions appear to be relatively inactive as the energy transfer rate associated with them is low.

The frequency spectrum gives information about the energy and time scales of turbulent motions. The normalized frequency spectra of the airside horizontal and vertical turbulent velocities at a height of 5.5 cm from the interface are plotted in Figs. 6.8 (a) and 6.8 (b), respectively, for all heat flux cases. The frequency spectra show similar trends for all turbulent velocities. The buoyancy subrange was observed at frequencies greater than approximately 0.8 Hz and no inertial subrange was evident.

Bukhari and Siddiqui (2006) presented frequency spectra of the waterside turbulent velocities. They observed buoyancy subrange in the frequency range $0.06 < f < 0.4$ Hz. No inertial subrange was observed at higher frequencies i.e. $0.5 < f < 7.5$ Hz. The plots of wavenumber spectra indicate that the inertial subrange exists at scales smaller than that of the buoyancy subrange. Thus, it is likely that the inertial subrange in the frequency spectra exists at higher frequencies which cannot be resolved with 15 Hz PIV measurements used in the present study and Bukhari and Siddiqui (2006). Comparison of frequency range associated with buoyancy subrange for air and water velocity fields indicate that the time scales of turbulent motions working against the buoyancy are relatively larger on the waterside.

The evaporation rate or the latent heat flux from the water surface depends on the airside relative humidity and is the dominant mode of air-water heat transfer. The humid air masses near the surface ascend through the air column and replaced by masses of descending dry air. The local evaporation rate depends on the rate of removal of the local humid air mass which in turn depends on the dynamics of the airside velocity field in the near-surface region. To further explore this issue, the frequency spectra of relative humidity at a height of 5.5 cm from the interface (same height as that of the frequency spectra in Fig. 6.8) for high and medium heat flux cases are plotted in Fig. 6.9. The buoyancy subrange is prominent in the spectra of relative humidity at both heat fluxes in the frequency range $0.08 < f < 1$ Hz. At higher frequencies, no specific trends are observed and the spectra are almost flat. The plot shows that the timescale of humidity variation is greater than 1 sec. Comparison of humidity and velocity spectra (Figs. 6.8 and 6.9) confirms that the turbulent motions are responsible for the transport of humid air

masses and replace them with the dry air. However, it also shows that only energetic low frequency turbulent motions can transport the air masses and that high frequency turbulent motions ($f > 1$ Hz in the present case) are not strong enough to displace humid air. The results in Fig. 6.5 show the dynamical nature of the airside turbulent velocity fields, which varies continuously in time and space. Due to the transport of dry and humid air masses by the turbulent structures, significant spatial and temporal variations in the evaporation rate are also expected at the water surface. Since the evaporation rate is the dominant mode of heat transfer from water to air, a variation in the evaporation rate would also cause a variation in the temperature field at the water surface. That is, a local high evaporation rate may result in a cooler patch at the water surface. The infrared images in Volino and Smith (1999) showed that the thermal structure at the water surface is quite random. Thus, it is reasonable to argue that the airside velocity fields in the near-surface region control the orientation and dynamics of the thermal structure formed at the water surface, which in turn influences the dynamics of the waterside velocity field.

The present work deals with the coupled air-water system in which, water surface undergoes evaporative cooling. The global-scale application of this type is the ocean-atmosphere system. Approximately 48 % of the solar radiation incident on earth is absorbed by the ocean and land. Due to the larger fractional coverage of the earth's surface by water (~ 70 %) and due to it's substantially higher heat capacity, the bulk of the thermal energy at the earth surface is stored in the oceans. A portion of this energy is transferred to atmosphere in the forms of sensible and latent heat which constitutes 15 % and 45 % of the incident solar radiation, respectively (Pickard and Emery 1990). This energy drives atmospheric circulation and thus, controls the global climate. Distribution

of atmospheric kinetic energy over the range of scales is of considerable interest in analyzing the atmospheric circulation and weather forecasting. Nastrom *et al.* (1984) and Nastrom and Gage (1985) measured zonal and meridional winds over the ocean in the altitude range of 9 - 13 km using instruments placed on board airlines in routine commercial service. Cho *et al.* (1999) examined the wavenumber spectra of the wind velocity above the Pacific Ocean. Measurements were taken by aircraft at altitudes ranging from about 50 m to 13 km. Bauer (1997) conducted measurements at a height of 10 m above the sea surface using ERS-1 scatterometer. The spectral analysis of wind velocities in all of these studies shows the distinct buoyancy subrange (with the slope of -3) and inertial subrange (with the slope of -5/3), similar to that observed in the present study. For zonal winds, the buoyancy subrange covered the spatial scales from 500 - 10,000 km and the inertial subrange covered the spatial scales from 10 - 500 km. For meridional winds, the buoyancy and inertial subranges cover 50 - 900 km and 1 - 50 km, respectively. The baroclinic instability in the low wavenumber range and convective motions in the high wavenumber range are attributed as the possible sources of energy.

The trends observed in horizontal and vertical velocity spectra in the present study are similar to that observed in climatological studies above the ocean. This indicates that the flow dynamics observed in the present small-scale laboratory experiments could be used to study some aspects of the ocean-atmosphere interactions. Comparison of velocity magnitudes in Fig. 6.3 shows that the airside velocities are more than 20 times larger than that on the waterside. Even under the neutral conditions when the bulk air-water temperature difference was negligible and the surface heat flux was almost entirely due to evaporation, the airside velocity magnitude is significant. Thus, it can be argued that the

evaporation or the latent heat transfer from ocean plays a significant role in atmospheric circulation. The velocity fields in Fig. 6.5 show the complex nature of the flow field above the water surface. These plots indicate that the flow dynamics changes drastically from one region to another and that the velocity measurements in one region may not predict the flow behavior correctly even in the neighboring region. Thus, the instantaneous flow structure measured at one location may not be the accurate representation of the instantaneous flow behavior in a relatively wider region. Similarly, the evaporation rate would also vary significantly from region to region. Thus, it can be concluded that the complexity of the airside turbulent flow structure is an important factor that affects the performance of global climate models and hence, the weather predictions. The energy contained by turbulent scales in the near surface region plays a significant role in atmospheric forcing of the ocean and in air-sea interaction processes (Tournadre and Blanquet 1994). These turbulent scales in the near-surface region also play an important role in controlling the heat and mass transfer across the interface. Buoyancy forces introduce a source of kinetic energy removal in addition to the energy dissipation and enhance the turbulent kinetic energy removal compared to the convectional turbulent flows. The present results show the presence of strong vortices in the near-surface region which enhance local mixing and hence the local air-water heat and mass transport. The dynamics of these near-surface physical mechanisms and their influence on the air-water heat and mass transfer rates should be adequately incorporated in the transport models to improve their accuracy and hence the weather predictions.

6.5 Conclusions

An experimental study is conducted to investigate the airside flow structure above an evaporative water surface during natural convection for three different surface heat flux conditions. The results show that the turbulent intensity profiles are self-similar for each velocity component. Comparison of turbulent velocity magnitudes on air and water sides show that under a given condition, the airside turbulent intensities are approximately 20 times stronger than that on the waterside. An improved description of the flow dynamics during natural convection is presented which shows that the turbulent velocity fields are complex and dynamic. The complexity arises from the local interactions of fluid motions in vertical, horizontal and normal directions, which result in the formation of local vortices that cause local mixing. Due to local interactions, the flow structures lose their signatures over relatively small distances, making it very difficult to correlate with other parameters. The spectral analysis of the turbulent velocities showed the existence of two distinct power law regimes. In low wavenumber regime, the buoyancy subrange is observed with a slope of -3 where the turbulent kinetic energy is removed by working against the buoyancy, except at the high heat flux in the near-surface region where the turbulent motions are relatively weak with respect to the buoyancy forces. In high wavenumber range, the inertial subrange with the classical slope of -5/3 is observed. Comparison of frequency spectra of air and water velocities shows that the airside turbulent motions are faster than that on the waterside. The strong airside turbulent motions are found to be responsible for the transport of humid air parcels. It is argued that the airside turbulent velocity fields control the local evaporation rate which in turn influences the water surface temperature field and the waterside velocity field. It is

also argued that due to similarities in the spectral trends from the meteorological and present laboratory datasets, laboratory experiments could provide an improved insight into the atmospheric dynamics. Based on the present results it is concluded that the instantaneous flow structure and evaporation rate measured at one location may not be the accurate representation of the instantaneous flow behavior in a relatively wider region and that the dynamics of strong near-surface physical mechanisms and their influence on the air-water heat and mass transfer rates should be adequately incorporated in the transport models to improve their accuracy and hence the weather predictions.

T_{wb} (°C)	36	30	23
q''_{total} (W/m^2)	678	367	88
q''_s (W/m^2)	591	309	85
w_* (cm/s) (airside)	15.8	12.7	8.3
w_* (cm/s) (waterside)	0.51	0.40	0.23

Table 6.1: T_{wb}, bulk water temperature; q''_{total}, total heat flux; q''_s, heat flux through the water surface; w_*, velocity scale.

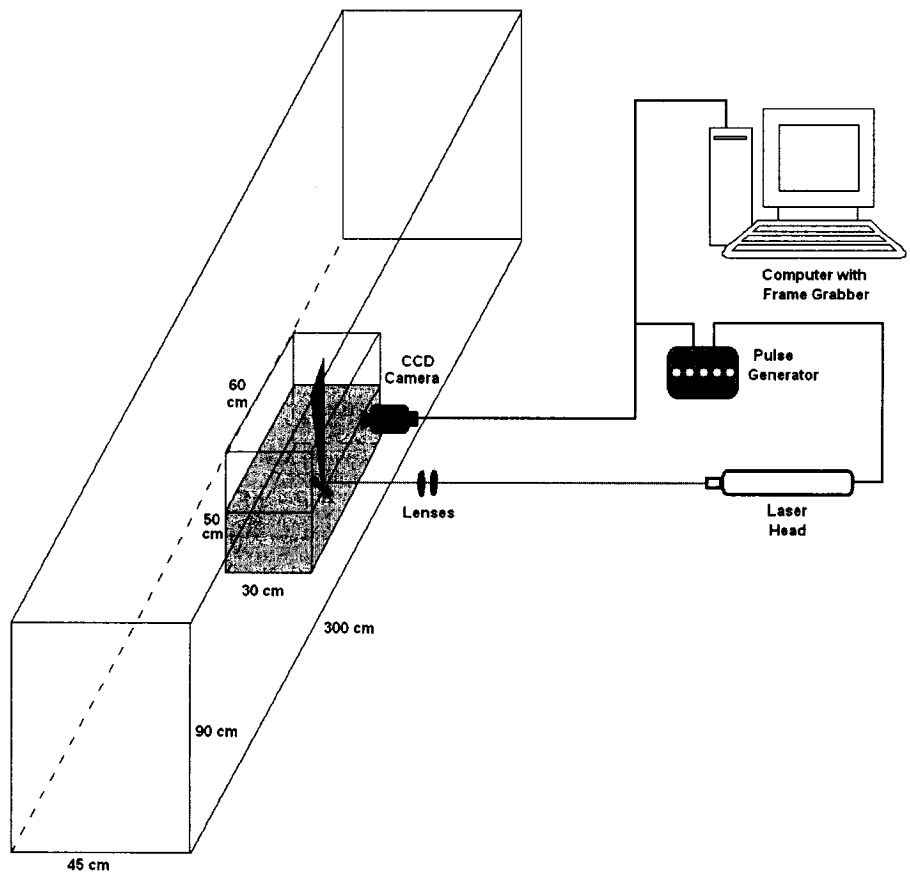

(a)

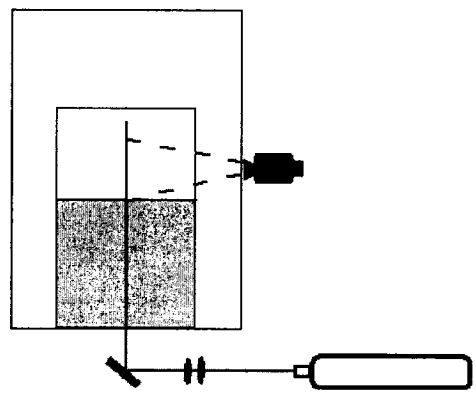

(b)

Fig. 6.1: Schematic of the experimental setup.

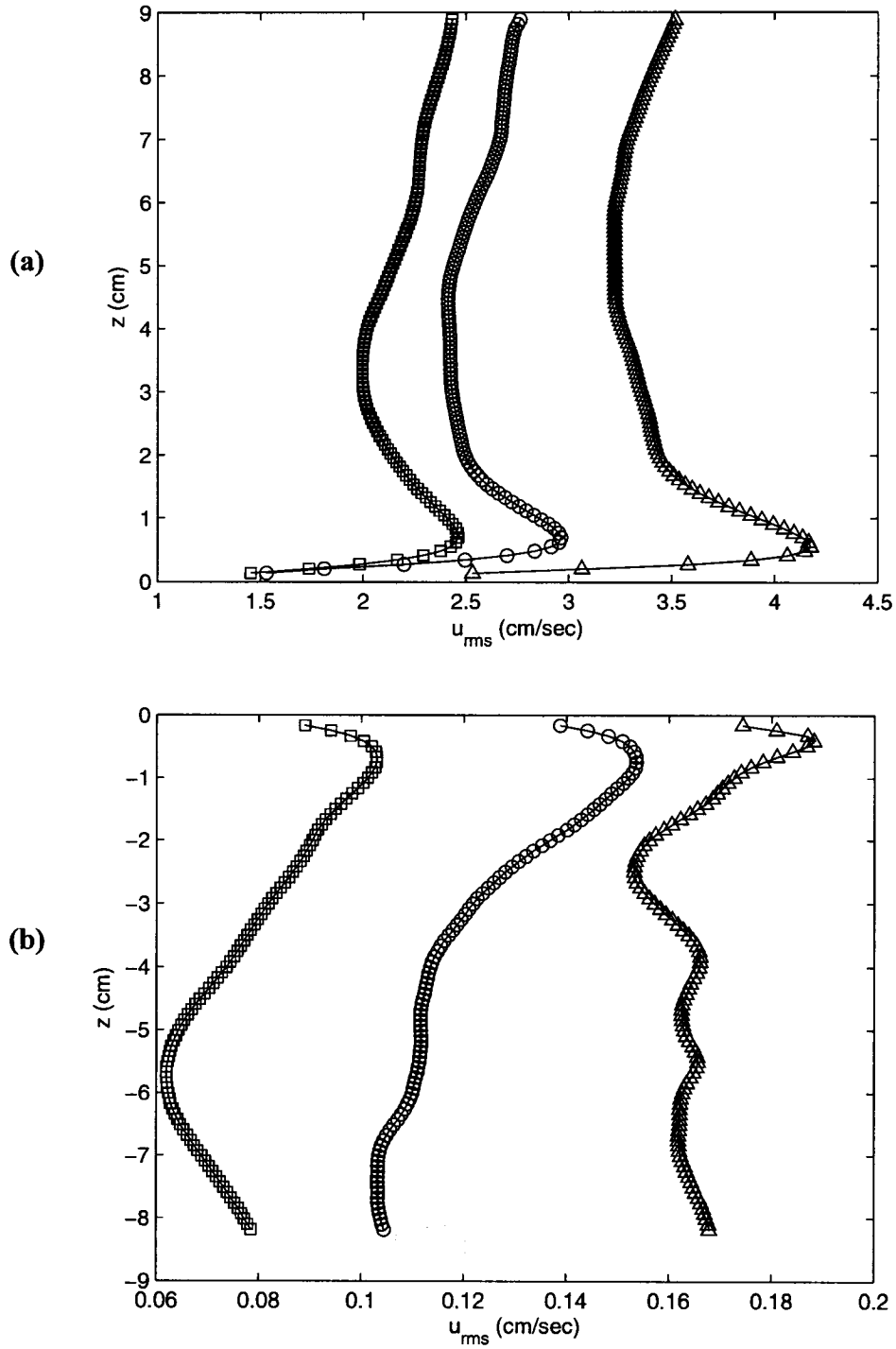

Fig. 6.2: Vertical profiles of RMS horizontal turbulent velocities, (a) airside (b) waterside. Δ, high heat flux; ○, medium heat flux; □, low heat flux. The waterside data is from Bukhari and Siddiqui (2006). The height (z) is measured from the water surface.

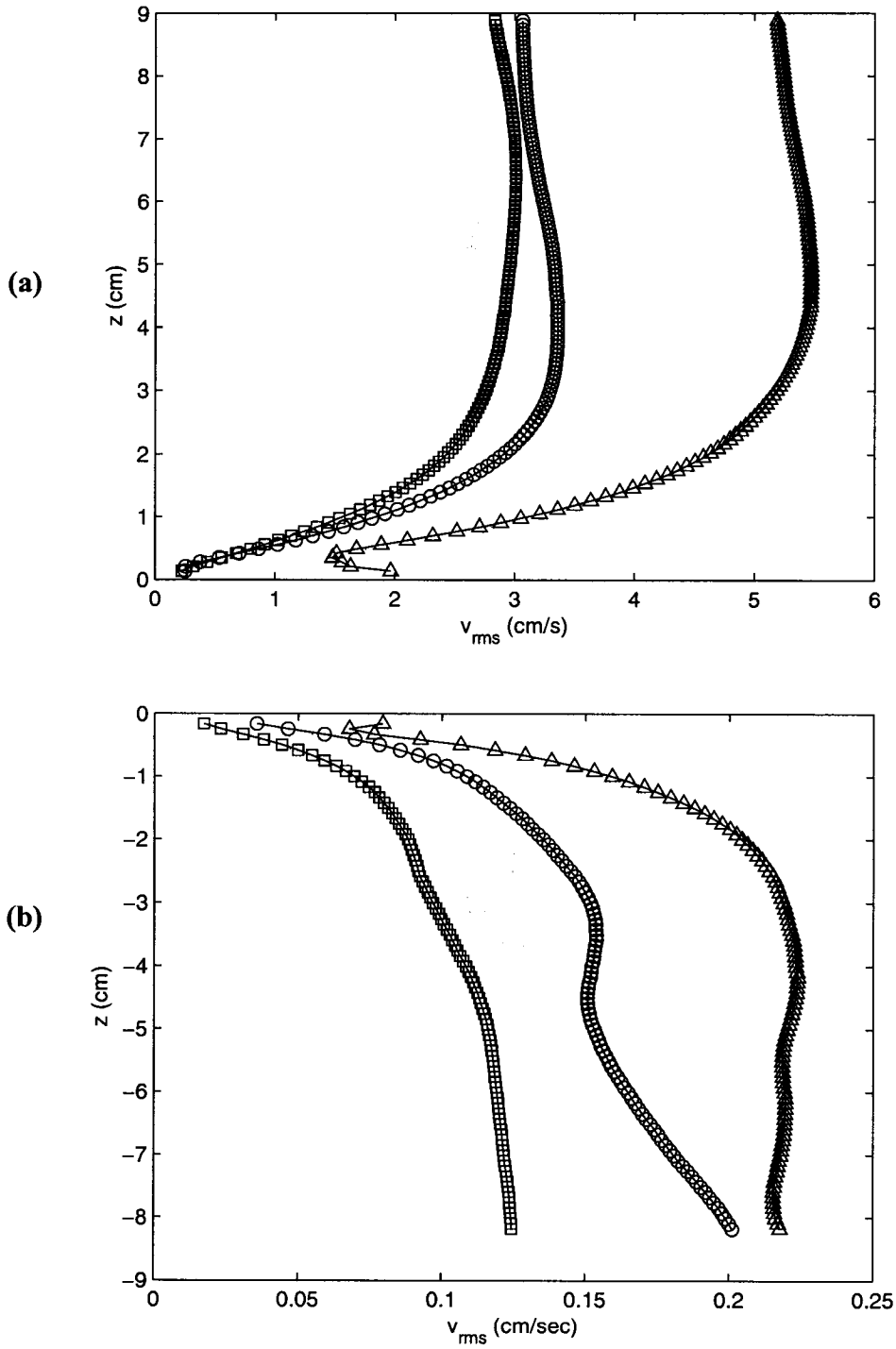

Fig. 6.3: Vertical profiles of RMS vertical turbulent velocities, (a) airside (b) waterside. Δ, high heat flux; ○, medium heat flux; □, low heat flux. The waterside data is from Bukhari and Siddiqui (2006).

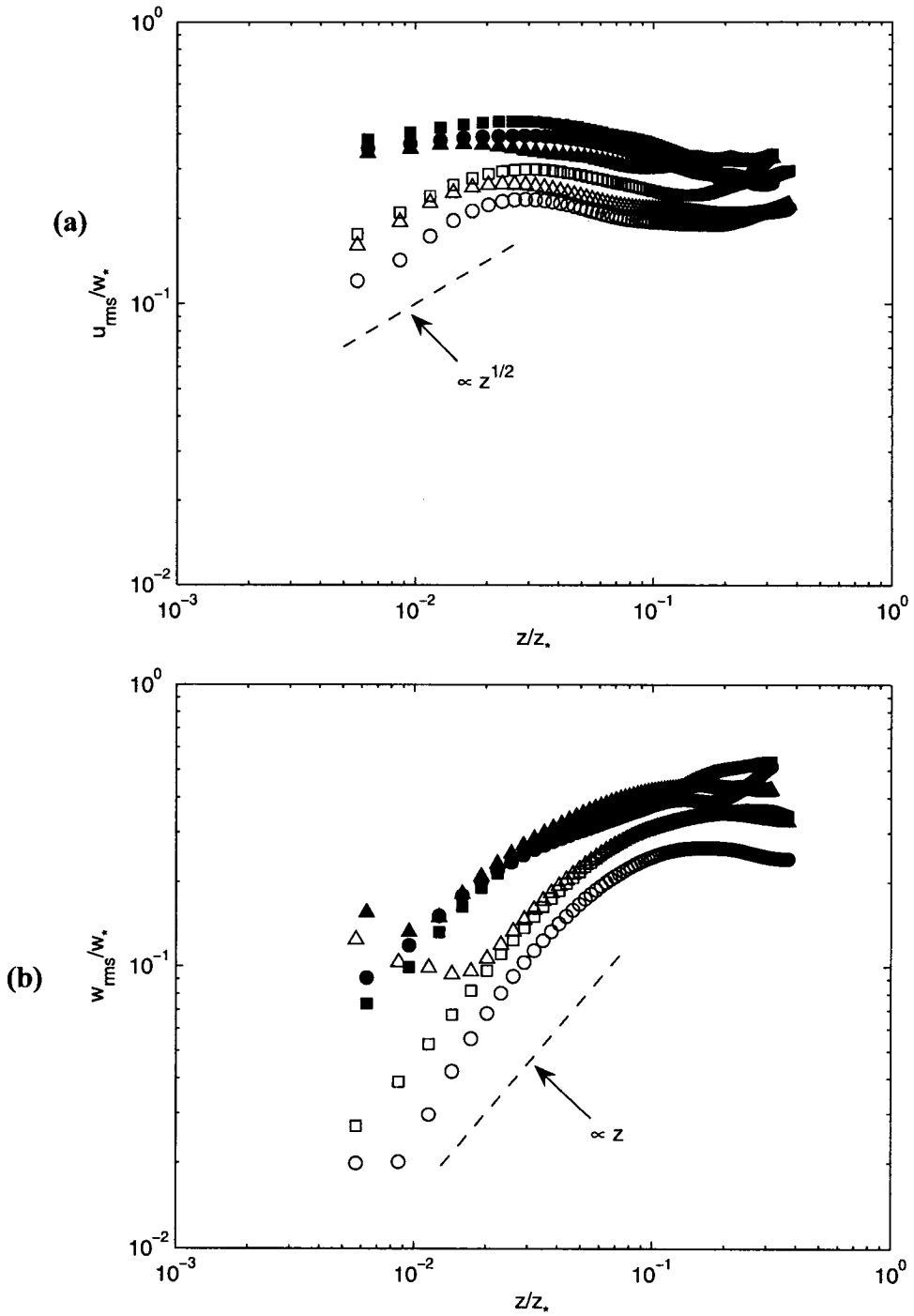

Fig. 6.4: Vertical profiles of air and waterside RMS turbulent velocities normalized by w_*. (a) horizontal velocity, (b) vertical velocity. Δ, high heat flux; ○, medium heat flux; □, low heat flux. Open symbols for airside data and solid symbols for waterside data. The waterside data is from Bukhari and Siddiqui (2006).

(6.5 a)

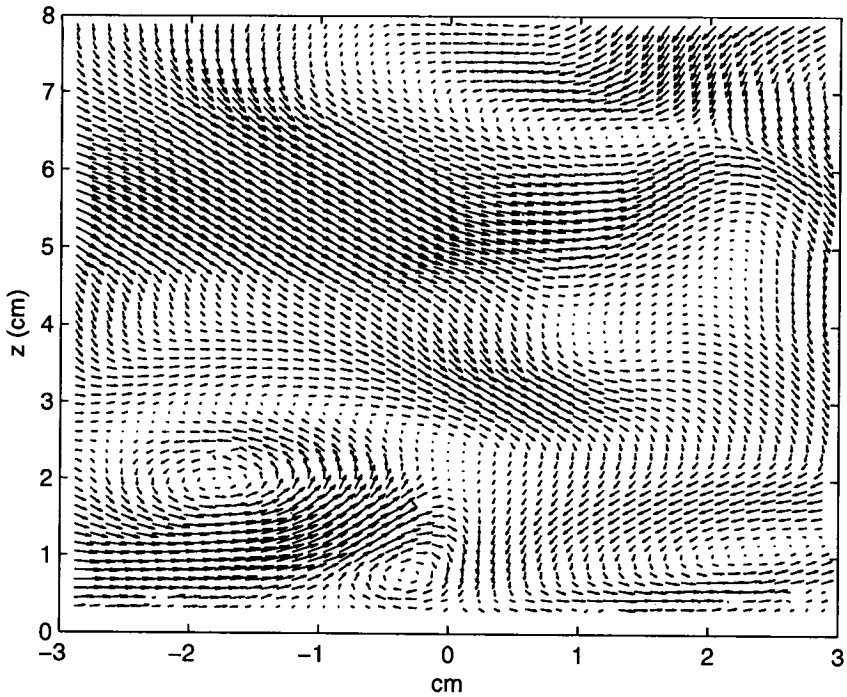

(6.5 b)

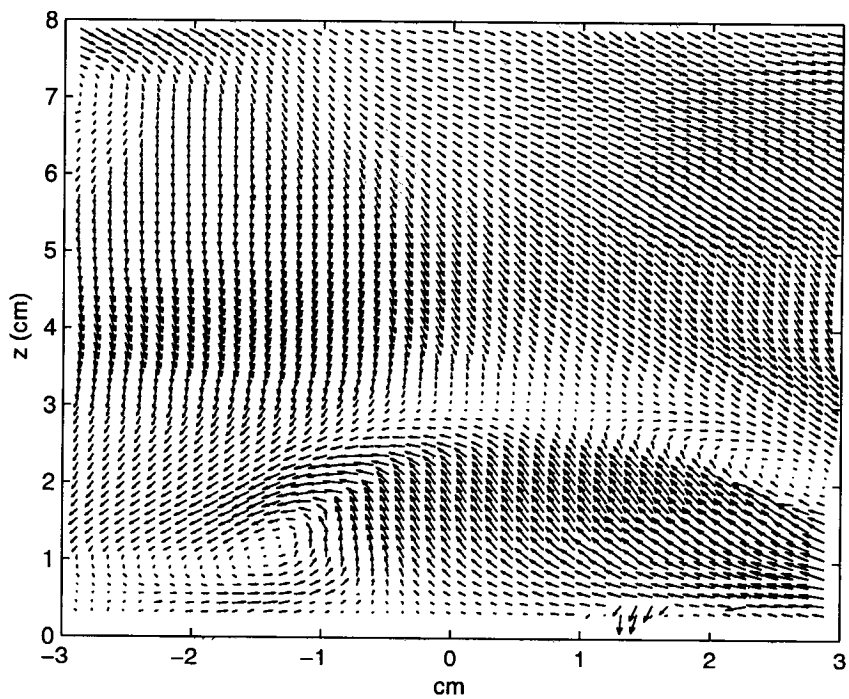

(6.5 c)

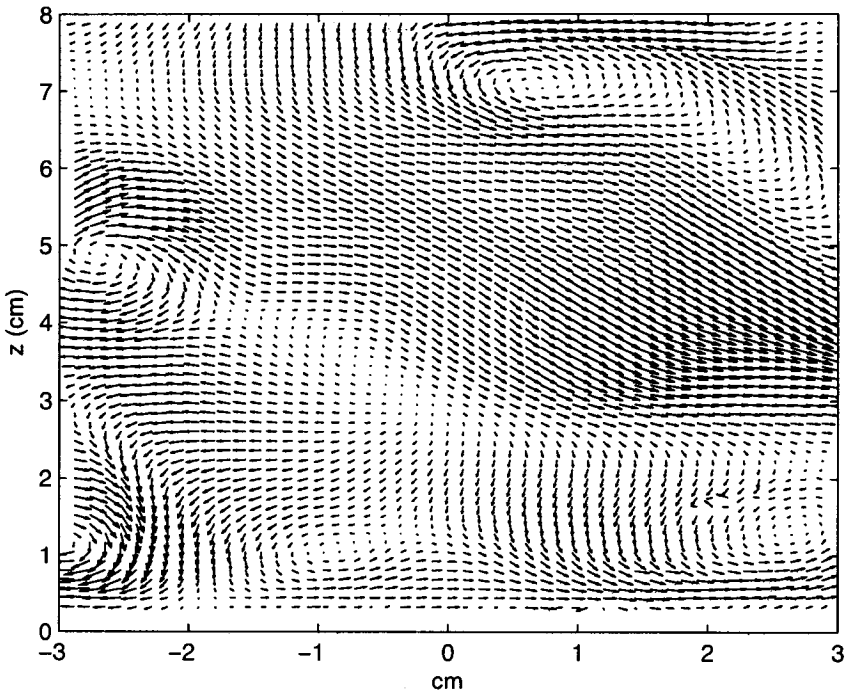

Fig. 6.5: Airside turbulent velocity fields at different instants of time for high heat flux case. Zero on x-axis represents mid tank location.

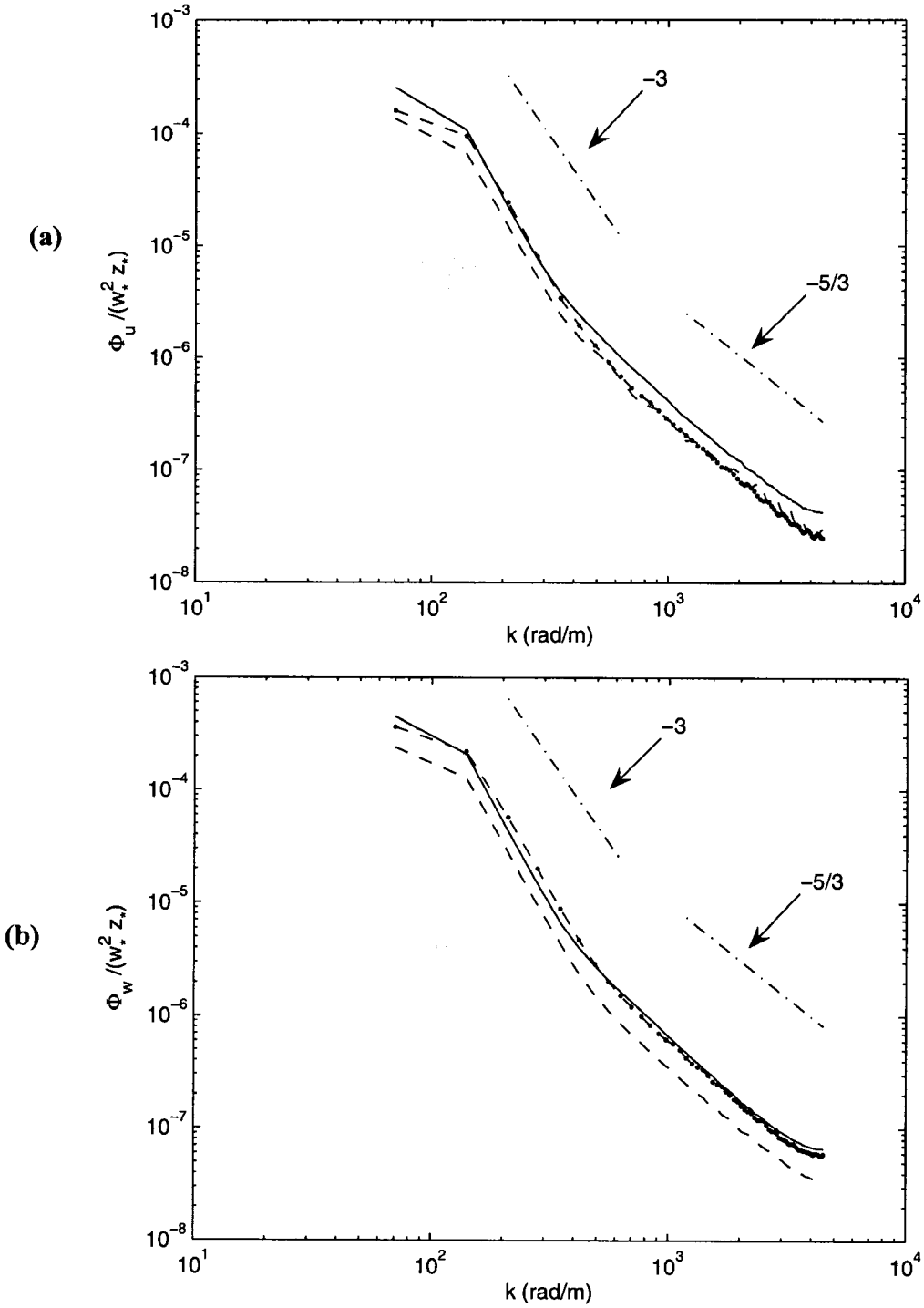

Fig. 6.6: Normalized wavenumber spectra at a height of 6.2 cm, (a) horizontal turbulent velocity, (b) vertical turbulent velocity. High heat flux (dot-dash); medium heat flux (dashed); low heat flux (solid). Dashed-dotted lines represent slopes.

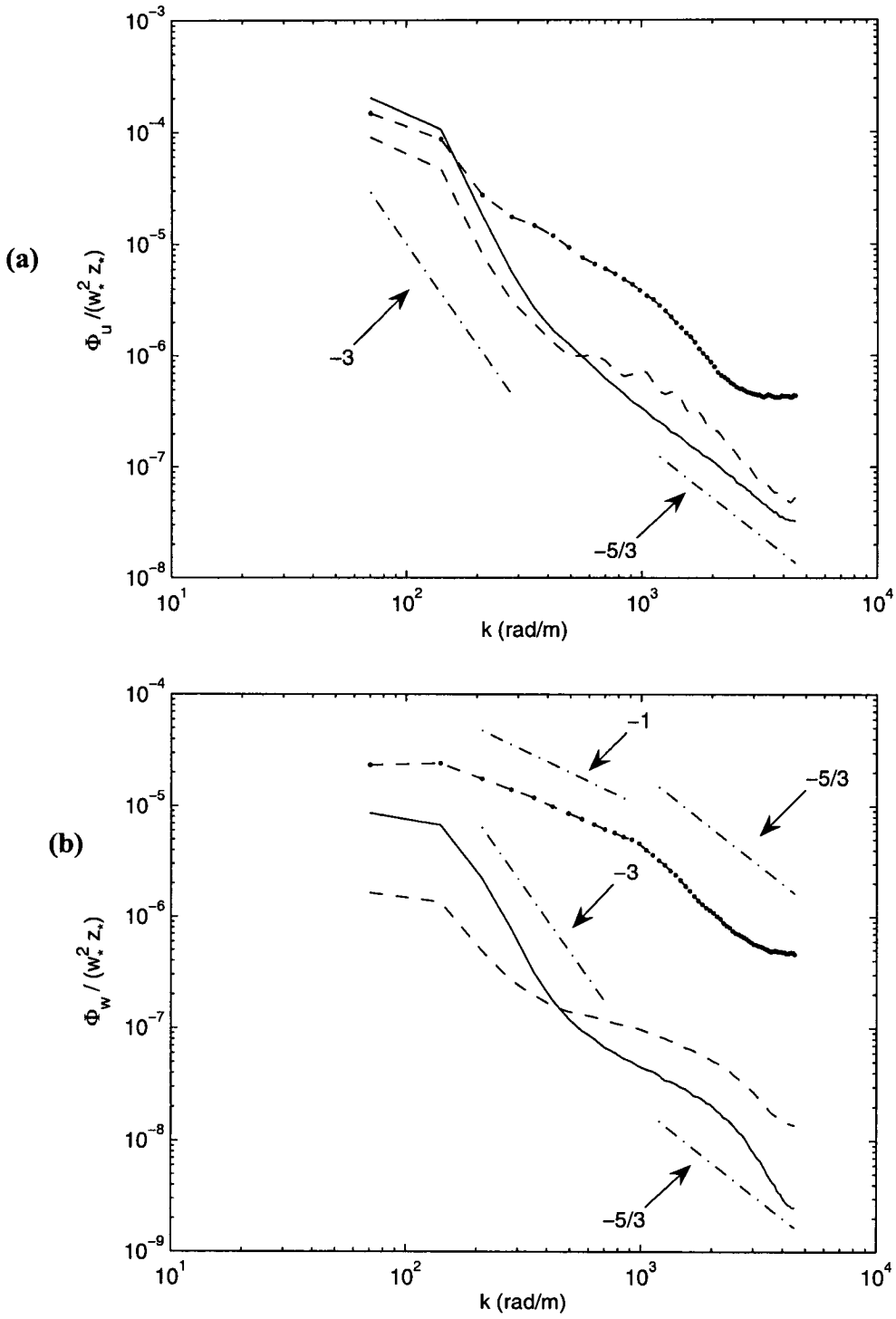

Fig. 6.7: Normalized wavenumber spectra at a height of 0.25 cm, (a) horizontal turbulent velocity, (b) vertical turbulent velocity. High heat flux (dot-dash); medium heat flux (dashed); low heat flux (solid). Dashed-dotted lines represent slopes.

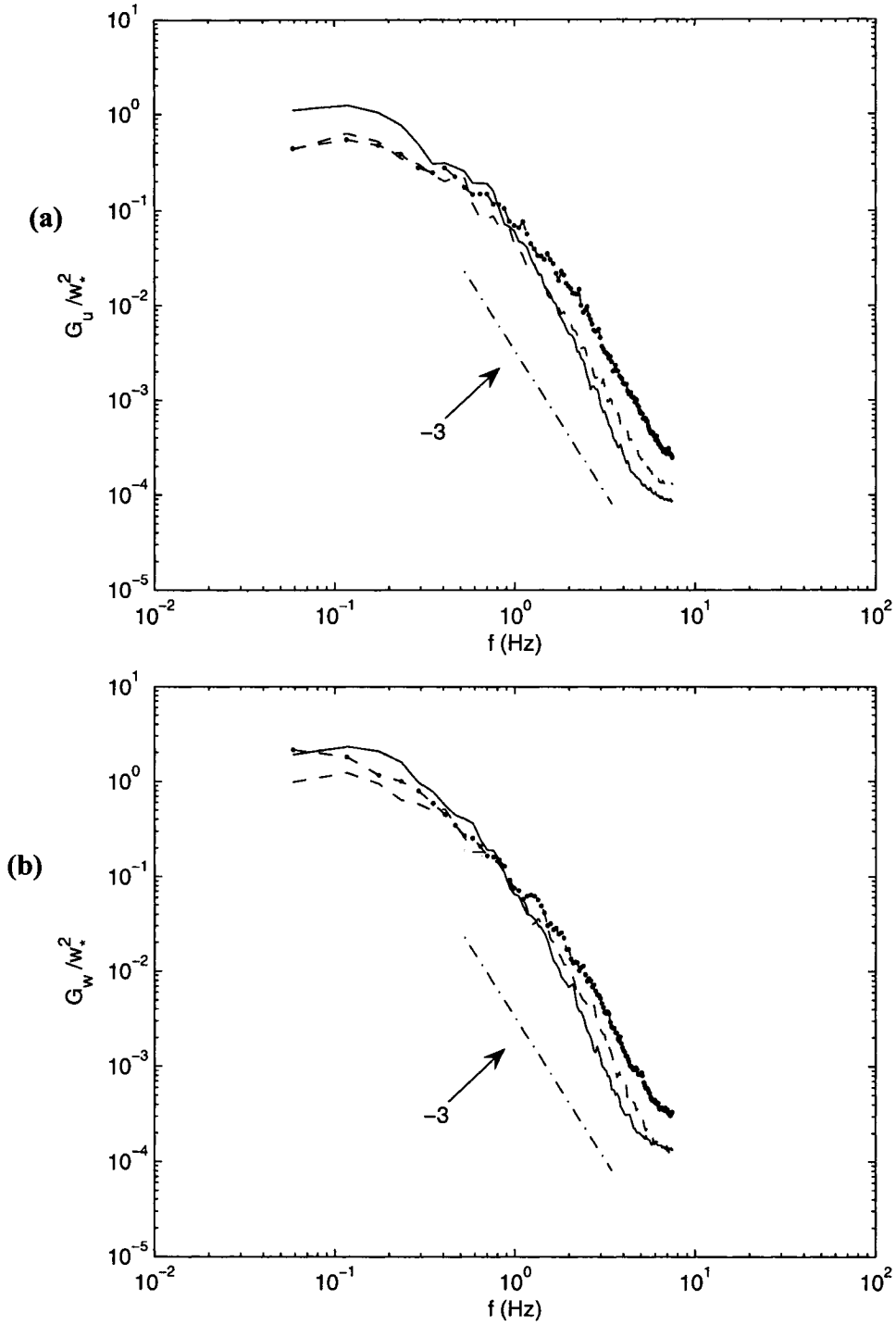

Fig. 6.8: Normalized frequency spectra at a height of 5.5 cm, (a) horizontal turbulent velocity, (b) vertical turbulent velocity. High heat flux (dot-dash); medium heat flux (dashed); low heat flux (solid). Dashed-dotted lines represent slopes.

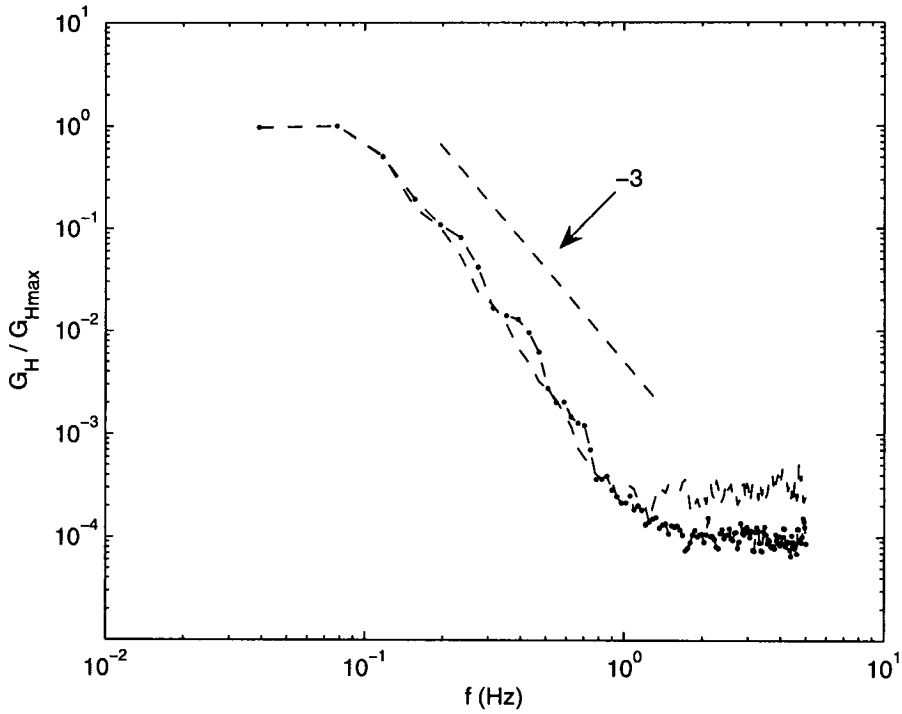

Fig. 6.9: Frequency spectra of relative humidity at a height of 5.5 cm. High heat flux (dot-dash); medium heat flux (dashed). Dashed-dotted lines represent slopes.

Chapter 7

Conclusions and Future Recommendations

7.1 Summary and Conclusions

In the present study a series of laboratory experiments has been conducted to investigate the flow fields on both sides of the air-water interface and thermal field on the waterside only, during natural convection. The main objectives of this study are to analyze the spatial structure of the thermal and hydrodynamic fields within the fluid layer and to determine the distribution of turbulent kinetic energy and its decay among the range of scales, on both air and water sides. The scaling parameters proposed for the wall-bounded natural convection were also examined for their applicability on the natural convection at stress-free air-water interface.

The experiments were conducted in a glass tank of 60 cm long, 30 cm wide and 50 cm deep. Three experimental conditions were considered for most of the experimental runs that correspond to the bulk water temperatures of 36, 30 and 23 °C. Thermal and hydrodynamic fields were measured using non-intrusive Laser Induced Fluorescence (LIF) and Particle Image Velocimetry (PIV) techniques, respectively. LIF measures temperature in fluid layers using temperature-sensitive fluorescent dye excited by the laser light. PIV measures velocity vectors in a plane simultaneously at many (thousands) points in a flow field.

The results presented in this thesis are the first detailed analysis of the turbulent structure on the air and water sides during natural convection. This research is aimed at

improving the fundamental understanding of the heat and mass transport across the air-water interface and the physical processes that influence this transport. This would lead to the improvement of heat and mass transfer models that will provide more accurate estimates of heat and mass transfer rates across the air-water interface during natural convection.

Chapter 2 describes the bulk structure of the flow fields on air and water sides in a coupled air-water system during natural convection. The velocity fields have been simulated using commercial CFD software Fluent. This chapter provides a good perception of the flow behavior and the bulk vortical motions in both fluid domains. The work presented in Chapter 2 is the first study in which the coupled air-water system has been considered and simultaneous air and waterside characteristics of the flow fields are simulated and analyzed. The results presented in Chapter 2, show organized vortical motions on the air and water sides. The magnitude of airside velocities is found to be an order of magnitude larger than the waterside velocities which show the existence of strong convective currents on the airside. It was concluded that the correlations for estimating the heat and mass fluxes during natural convection could be improved by considering the effect of the flow velocities.

In Chapter 3, the experimental results of the waterside turbulent structure beneath an evaporating water surface are reported. This chapter provides the first detailed qualitative and quantitative analysis of the waterside flow field during natural convection. It includes the analyses of turbulent velocity fields and turbulent properties. The results show that the waterside flow field undergoes different flow interactions that result in the formation of complex flow patterns and create local vortices. These vortices enhance

local mixing and heat transfer. In the near surface region, these vortices play an important role in renewing the water surface and controlling the thermal and momentum boundary layer thicknesses which regulates interfacial heat and mass fluxes. These flow patterns in the near-surface region form complex thermal structure at the interface which was observed by Volino and Smith (1999), Flack *et al.* (2001) and Spangenberg and Rowland (1961). Due to the varying nature of these interactions, it is difficult to predict the flow behavior in one region based on the flow behavior in a neighboring region, making this problem more complicated. The wavenumber and frequency spectra exhibit -3 slopes providing the first evidence of the existence of the buoyancy subrange beneath the evaporative water surface where the energy loss is due to the work against buoyancy. The spectral analysis also indicated that the turbulent motions must be strong enough to interact with the buoyancy forces otherwise, the turbulent energy transfer follows the convectional energy transfer mechanism with the classical slopes of -5/3.

In Chapter 4, the impact of air saturation on the waterside turbulent structure beneath air-water interface is investigated. The results show that air saturation has a significant impact on the waterside turbulent structure. As the air becomes saturated, the magnitudes of the horizontal and vertical turbulent velocities are decreased by factors of 5 and 2.5, respectively. This reduction in the waterside velocities is attributed to the reduction in the surface heat flux and the reduction in the airside velocity magnitude at the saturation state. The spectral analysis shows that both horizontal and vertical turbulent motions are much weaker than that for the unsaturated case. For the saturated cases, the range of the turbulent motions responsible for working against buoyancy forces is smaller than that for the unsaturated cases.

Chapter 5 describes the experimental results of the thermal convection in horizontal water layers beneath an evaporating water surface during natural convection. This is the first study which provided the non-intrusive measurements of the waterside temperature profile particularly, within the thin conduction layer immediately below the interface with high resolution. The temperature field in a plane perpendicular to the surface shows the presence of falling cold and rising warm water. Existence of the thin cool skin layer at the evaporating surface is also evident in the temperature field. The measured mean temperature profiles show a characteristic boundary layer distribution in the near surface region with an extensive core of constant temperature in the bulk. Linear temperature variation immediately below the interface corresponds to the conduction layer where the heat transfer is primarily due to molecular conduction. The power law dependency in the region between the conduction layer and the bulk is found to follow z^{-1} power law. However, away from the surface where eddies transfer heat and momentum, $z^{-1/3}$ dependency is observed. Relationship between the conduction and convection layers scaling of velocity and temperature, defined for solid wall case, are also valid for free surface case. Theoretical profiles proposed by Howard (1963) agreed very well with the experimental data within the conduction layer.

Chapter 6 presents the experimental results of the two-dimensional airside flow structure above evaporative water surface during natural convection. Detailed analysis of the airside flow structure shows that the velocity field is three-dimensional that undergoes different flow interactions. The results presented in Chapter 3 for waterside turbulent structure also show similar complexity of the waterside flow field. The results in Chapter 6 show strong convective motions on the airside compared to the waterside. The

magnitude of the airside turbulent velocities was found to be approximately 20 to 25 times higher than the waterside velocities. Simulation results presented in Chapter 2 also show strong convective currents on the airside. The wavenumber spectra of horizontal and vertical turbulent velocities show the existence of two power law regimes similar to that on the waterside. The regime at lower wavenumbers exhibits slopes of -3 which correspond to the buoyancy subrange. At relatively higher wavenumbers, the inertial subrange with the slopes of -5/3 is manifested where the energy transfer depends only on the energy dissipation rate. For high heat flux conditions, the spectra for horizontal and vertical turbulent velocities does not show the existence of the buoyancy subrange in the near surface region because the turbulent motions are relatively weaker than that at greater depths. It is argued that due to similarities in the spectral trends from the meteorological and present laboratory datasets, laboratory experiments could provide an improved insight into the atmospheric dynamics. Comparison of frequency spectra of air and water velocities shows that the airside turbulent motions are faster than that on the waterside and control the local evaporation rate which in turn influences the water surface temperature field and the waterside velocity field. It was also found that the instantaneous flow structure and evaporation rate measured at one location may not be the accurate representation of the instantaneous flow behavior in a relatively wider region.

7.2 Recommendations for Future Research

In the present research, laboratory experiments were conducted under three experimental conditions to investigate the thermal and hydrodynamic fields during natural convection from an evaporative water surface. Two cases correspond to the

unstable thermal stratification with bulk water temperature warmer than the bulk air and the third case correspond to the neutral condition. The results presented in this research provided a deep insight and fundamental understanding of the waterside and airside turbulent structures across evaporating water surface which have not been reported before. However, there are many issues which still need further consideration and that would lead to an improved understanding of this important phenomenon in nature. Following are some recommendations for future work.

1) Numerically obtained airside velocity fields can be improved by incorporating the airside concentration gradients or change in the relative humidity in the CFD code.
2) The relationship between the temperature and velocity fields is not well established. The simultaneous measurements of the velocity and temperature fields in the same plane are recommended to provide improved understandings of the velocity and temperature interactions. The relationship between the velocity and temperature fields will also benefit in the development of advanced remote sensing techniques to detect subsurface objects and to remotely measure the surface heat fluxes.
3) The velocity and temperature fields in the present study are two-dimensional. The present results showed that during natural convection, the flow fields on both air and water sides are three-dimensional that undergoes different flow interactions, which result in the formation of complex flow patterns. Therefore three-dimensional analysis is recommended for future work which will improve the results of the present study.

4) Simultaneous measurements of airside and waterside velocity fields are also recommended that will help in a batter understanding of the interfacial transport phenomenon.

5) In the present study, the impact of surfactants on the turbulent structures is not considered. Some previous studies have argued that the presence of surfactant monolayer at the air-water interface can profoundly affect the flow and thermal behavior and thus, the surface heat flux. Therefore, consideration of the impact of surfactants on the flow and thermal behavior is recommended as a future work.

6) A comprehensive study is also recommended that will consider the combine effect of the temperature and velocity fields on air and water sides.

7) The use of high resolution camera is also important and will improve the results.

REFERENCES

Adrian, R. J., Ferreira, R. T. D. S. and Boberg, T. (1986) Turbulent thermal convection in wide horizontal fluid layer. *Exp. Fluids,* **4**, 121-141.

Akyuzlu, K., Nemani, M. S. and Chakravarthy, K. (2003) An experimental study of circulation patterns in a natural convection using PIV. *Proceedings of IMECE'03, Washington, D.C.,* November 15-21.

Al-Shammiri, M. (2002) Evaporation rate as a function of water salinity. *Desalination* **150**, 189-203.

Bauer, E. (1997) Statistical comparison of winds from ERS-1 scatterometer and ECMWF model in time and wavenumber domain. *ERS symposium on space at the service of our environment, Florence , ITALIE* **3**, 1195-1200.

Bejan, A. (1993) Heat Transfer, Wiley, New York.

Bejan, A. (2004) Convection Heat Transfer, Wiley, New York.

Benard, H. (1900) Les Tourbillions cellulaires dans une nappe liquide. *Revue general des Scieneces pures et appliques* **11**, 1309-1328.

Benard, H. (1901) Les Tourbillions cellulaires dans une nappe liquide. *Ann. Chim. Phys.* **23**, 1261-1271.

Bodenschatz, E., Pesch, W., and Ahlers, G. (2000) Recent developments in Rayleigh-Benard convection. *Annual Review of Fluid Mechanics*, **32**, 709-778.

Bukhari, S. J. K. and Siddiqui, M. H. K. (2006) Turbulent structure beneath air-water interface during natural convection. *Phys. Fluids,* **18**, 035106.

Bukhari, S. J. K. and Siddiqui, M. H. K. (2007) Characteristics of air and water velocity fields during natural convection. *Heat Mass Transfer,* **43**, 5, 415-425.

Bukhari, S. J. K. and Siddiqui, M. H. K. (2007) The Impact of Air Saturation on the Flow Structure beneath Air-Water Interface during Natural Convection. *International Journal of Heat and Mass Transfer* (in press).

Bukhari, S. J. K. and Siddiqui, M. H. K. (2007) An Experimental Study of the Thermal Field underneath an evaporative water surface using Laser Induced Fluorescence (LIF) (submitted to *International Journal of Heat and Mass Transfer*).

Bukhari, S. J. K. and Siddiqui, M. H. K. (2007) An Experimental Study of the Airside Flow Structure during Natural Convection (submitted to *Journal of Fluid Mechanics).*

Busse, F. H. (1978) None linear properties of thermal convection. *Report on Progress in Physics,* **41**, 1929-1967.

Chernous'ko, Y. L. (1971). Laboratory investigation of micro-convection. *Atmosp. Oceanic Phys.*, **7**, 1096-1098.

Cho, J. Y. N., Newell, R. E. and Barrick, J. D. (1999) Horizontal wavenumber spectra of winds, temperature and trace gases during the Pacific Exploratory Missions: 2. Gravity waves, quasi two-dimensional turbulence and vortical modes. *J. Geophys. Res.,* **104,** 16297-16308.

Chu, T. Y. and Goldstein, R. J. (1973) Turbulent convection in a horizontal layer of water. *J. Fluid Mech.,* **60**, 141-159.

Collen, M. C. J. Kieft, R. N. Rindt, C. C. M. and van Steenhoven, A. A. (1999) Application of 2-D LIF temperature measurements in water using a ND:YAG laser. *Exp. Fluids*. **27**, 420-426.

Csanady, G. T. (2001) Air-Sea Interaction: Laws and Mechanics. Cambridge University Press.

Clayson, C. A., Curry, J. A. and Fairall, C. W. (1996) Evaluation of turbulent fluxes at the ocean surface using surface renewal theory. *J. Geophys. Res.,* **101**, 28503-28513.

Cowen, E. A. and Monismith S. G. (1997) A hybrid digital particle tracking velocimetry technique. *Exp. Fluids,* **22**, 199-211.

Deardorff, J. W. (1970) Convective velocity and temperature scales for the unstable planetary boundary layer and for Rayleigh convection. *J. Atmos. Sci.,* **27**, 1211-1212.

Deardorff, J. W. and Willis, G. E. (1967). Investigation of turbulent thermal convection between horizontal plates. *J. Fluid Mech.,* **28**, 675-704.

Fincham, A. M. and Spedding G. R. (1997) Low cost, high resolution DPIV for measurement of turbulent fluid flow. *Exp. Fluids,* **23**, 449-462.

Fincham, A. M., Maxworthy, T. and Spedding G. R. (1996) Energy dissipation and vortex structure in freely decaying, stratified grid turbulence. *Dyn. Atmos. Oceans*, **23**, 155-169.

Fitzjarrald, D. E. (1976) An experimental study of turbulent convection in air. *J. Fluid Mech.,* **73**, 693-719.

Flack, K. A., Saylor, J. R. and Smith, G. B. (2001) Near-surface turbulence for evaporative convection at an air/water interface. *Phys. Fluids,* **13**, 3338-3345.

Fluent 6.1 User's guide, (2003).

Freilich,M. H. and Chelton,D. B. (1986) Wavenumber spectra of pacific winds measured by the seasat scatterometer. *Journal of Physical Oceanography* **16,** 741-757.

Garon, A. M. and Goldstein, R. J. (1973) Velocity and heat transfer measurements in the thermal convection. *Phys. Fluids,* **16,** 1818-1825.

Gebhart, B. and Pera, L. (1971) The nature of vertical natural convection flows resulting from the combined buoyancy effects of thermal and mass diffusion. *Int. J. Heat Mass Transfer,* **14**, 2025-2050.

Gill, A. E. (1982) Atmosphere-Ocean Dynamics. Academic Press.

Goldstein, R. J. and Volino, R. J. (1995) Onset and development of natural convection above a suddenly heated horizontal surface. *ASME J Heat Transfer*, **117**, 808-821.

Goldstein, R. J. and Chu, T. Y. (1969) Thermal convection in a horizontal layer of air. *Prog. Heat Mass Transfer,* **2**, 55-75.

Heon, J. L. (2003) Application of a ratio metric laser induced fluorescence (LIF) thermometry for micro-scale temperarature measurement for natural convection flows. Masters thesis, Dept. of Mech. Eng. University of Texas A & M, Texas.

Hinze, O. (1975) Turbulence. McGraw Hill.

Hinchley, J. W. Himus, G. W. (1924) Evaporation in currents of air. *Journal of the Society of Chemical Industry,* **7**, 57-63.

Howard, L. N. (1963) Heat transport by turbulent convection. *J. Fluid Mech.,* **17**, 405-432.

Howard, L. N. (1966) Convection at high Rayleigh number." Proceeding of the 11th international congress of applied mechanics, Munich (Germany) edited by H. Gortler. 1109-1115.

Incropera, F. P. Dewitt, D. P. Bergman, T. L. and Lavine, A. S. (2006) Fundamentals of Heat and Mass Transfer 6th edition. John Wiely and Sons.

Incropera, F. P. Dewitt, D. P. (2001) Introduction to Heat Transfer 4th edition, John Wiely and Sons.

Kantha, L. H. and Clayson, C. J. (2000) Small scale processes in geophysical fluid flows. Academic Press.

Katsaros, K. B. Liu, W. T. Businger, J. A. and Tillman, J. E. (1977) Heat transport and thermal structure in the interfacial boundary layer measured in an open tank of water in turbulent free convection. *J. Fluid Mech.*, **83**, 311-335.

Keane, R. D. and Adrian, R. J. (1992) Theory of cross-correlation analysis of PIV images." *Appl. Sci. Res.*, **49,** 191-215.

Kim, H. J., Kihm, K. D., and Allen, J. S. (2003) Examination of ratio metric laser induced fluorescence thermometry for micro scale spatial measurement resolution. *Int. J. Heat Mass Transfer,* **46,** 3967-3974.

Koshyk, J. N. Hamilton,K. and Mahlman, J. D. (1999b) Simulation of the k-5/3 mesoscale spectral regime in the GFDL SKYHI general circulation model. *Geophys. Res. Lett.*, **26,** 843-846.

Koshyk, J. N. and Hamilton, K. (2001) The horizontal kinetic energy spectrum and spectral budget simulated by a high-resolution Troposphere-Stratosphere-Mesosphere GCM. *J. Atmos. Sci.*, **58**, 4, 329-348.

Kraichnan, R. H. (1962) Turbulent thermal convection at arbitrary Prandtl number. *Phys. Fluids,* **5**, 11, 1374-1389.

Kraichnan, R. H. (1967) Inertial ranges in two-dimensional turbulence." *Phys. Fluids,* **10,** 1417-1423.

Liss, P. S. (1973) Processes of gas exchange across an air-water interface. *Deep Sea Res.*, **20**, 221-239.

Lovejoy, S., Schertzer, D., Lilley, M., Strawbridge, K. and Radkevitch, A. (2006) Scaling turbulent atmospheric stratification, Part I: turbulence and waves Quart. *J. Roy. Meteor. Soc.*, (submitted).

Marxen, M. (1998) Particle Image Velocimetry in Strömungen mit starken Geschwindigkeitsgradienten. (Diplom Thesis, Fakultät für Physik und Astronomie, Ruprecht-Karls-Universität Heidelberg).

Nastrom, G. D. Gage, K. S. and Jasperson, W. H. (1984) Kinetic energy spectrum of large and mesoscale atmospheric processes. *Nature,* **310,** 36-38.

Nastrom, G. D. and Gage, K. S. (1985) A climatology of atmospheric wavenumber spectra of wind and temperature observed by commercial aircraft. *J. Atmos. Sci.*, **42,** 950-960.

Pickard, G. L. and Emery, W. J. 1990 Descriptive physical oceanography : an introduction. 5th edition Oxford; New York: Pergamon Press.

Prasad, A. K. and Gonuguntla, P. V. (1996) Turbulence measurements in non-penetrative thermal convection. *Phys. Fluids*, **8**, 2460-2470.

Prasad, A. K., Adrian, R. J., Landreth, C. C. & Offutt, P. W. (1992) Effect of resolution on the speed and accuracy of particle image velocimetry interrogation. *Exp. Fluids,* **13**, 105-116.

Priestley C. H. B. (1959) Turbulent transfer in the lower atmosphere. Chicago: University of Chicago press.

Priestley C. H. B. (1954) Convection from a larger horizontal surface. *Aust. J. Phys.*, **7**, 176-201.

Rayleigh, L. (1916) On convection currents in a horizontal layer of fluid when the higher temperature is on the under side. *Phil Mag.*, **32,** 529-546.

Sakakibara, J. and Adrian, R. J. (1999) Whole field measurement of temperature in water using two-color laser induced fluorescence. *Exp. Fluids.*, **26**, 7-15.

Saylor, J. R. Flak, K. A. Schultz, M. P. and Smith, G. B. (2002) The correlation between surface temperature and subsurface velocity during evaporative convection. *Exp. Fluids,* **32**, 570-579.

Saylor, J. R. Smith, G. B. and Flak, K. A. (2001) An experimental investigation of the surface temperature field during evaporative convection. *Phys. Fluids,* **13**, 2, 428-439.

Saylor, J. R. Smith, G. B. and Flak, K. A. (2000) Infrared imaging of the surface temperature field of water during film spreading. *Phys. Fluids,* **12**, 3, 597-602.

Saylor, J. R. and Handler, R. A. (1997) Gas transport across an air/water interface populated with capillary waves. *Phys. Fluids,* **9**, 9, 2529-2541.

Schatz, M. F. and Neitzel, G. P., (2001) Experiments on thermocapillary instabilities. *Annual Review of Fluid Mechanics*, **33**, 1, 93-127.

Siddiqui, M. H. K. Loewen, M. R. Richardson, C. Asher, W. E. and Jessup, A. T. (2001) Simultaneous particle image velocimetry and infrared imagery of microscale breaking waves, *Phys. Fluids,* **13**, 1891 -1903.

Siddiqui, M. H. K. (2002) Laboratory measurements of the flow beneath microscale breaking waves. Ph.D. thesis, University of Toronto.

Siegel, D. A. and Plueddemann, A. J. (1991) The motion of a solid sphere in an oscillating flow: An evaluation of remotely sensed doppler velocity estimates in the sea. *J. Atmos. Oceanic Technol.*, **8**, 296-304.

Snyder, W. H. and Lumley, J. L. (1971) Some measurements of particle velocity autocorrelation functions in a turbulent flow. *J. Fluid Mech.*, **48**, 41-71.

Spangenberg, W. G. and Rowland, W. R. (1961) Convective Circulation in Water Induced by Evaporative Cooling. *Phys. Fluids,* **4**, 743-750.

Sparrow, E. M. and Husar, R. B. and Goldstein, R. J. (1970) Observations and other characteristics of thermals. *J. Fluid Mech.*, **41**, 793-800.

Sparrow, E. M. and Nunez, G. A. (1988) Experiments on isothermal and non-isothermal evaporation from partially filled, open-topped vertical tubes. *Int. J. Heat Mass Transfer,* **31**, 7, 1345-1355.

Sorbjan, Z. (1990) Similarity Scales and Universal Profiles of Statistical Moments in the Convective Boundary Layer. *J. Appl. Meteor.*, **29**, 762-775.

Somerscales, E. F. C. and Gazda, I. W. (1969) Thermal convection in high Prandtl number liquids at high Rayleigh numbers. *Int. J. Heat Mass Transfer,* **12,** 1491-1511.

Tennekes, H. and Lumley, J. L. (1972) A First Course in Turbulence. MIT press.

Thomas, D. B., and Townsend, A. A. (1957) Turbulent convection over a heated horizontal surface. *J. Fluid Mech.*, **2**, 473-492.

Thomson, J. (1982) On a changing tessellated structure in certain liquids. *Proc Philosophical Society of Glasgow,* **13**, 464-468.

Tournadre, J. & Blanquet, S. 1994 Wind speed and wave mesoscale variability from in situ and altimeter data. *The Global Atmosphere and Ocean System,* **2**, 221-245.

Townsend, A. A. (1976) The structure of turbulent shear flow. Cambridge University Press, Second edition.

Townsend, A. A. (1959) Temperature fluctuations over a heated horizontal surface. *J. Fluid Mech.*, **5**, 209-241.

Turner, J. S. (1973) Buoyancy effects in fluids. Cambridge University Press.

Veron, F. and Melville, W. K. (1999) Pulse-to-pulse coherent Doppler measurements of waves and turbulence. *J. Atmos. Oceanic. Technol.* **16**, 1580-1597.

Volino, R. J. and Smith, G. B. (1999) Use of simultaneous IR temperature measurements and DPIV to investigate thermal plumes in a thick layer cooled from above. *Exp. Fluids,* **27,** 70-78.

Zappa, C. J. (1999) Microscale wave breaking and its effect on air-water gas transfer using infrared imagery. Ph.D. thesis, Applied Physics Laboratory, University of Washington Seattle.

Appendix A

Error Estimate for the DPIV measurements

The total error in the DPIV measurements is the sum of the errors due to gradients, particle density, particle diameter, out-of-plane motion, dynamic range, peak locking and AGW interpolation (Cowen and Monismith 1997). The non-dimensional particle diameter in the present study was 0.3 pixels/pixel. Particles smaller than one pixel always occupy one pixel area in a DPIV image. As a result, they are not able to resolve the true position of the particle within a pixel. Furthermore, the particle diameters less than one pixel also increases the peak locking errors. The duration of the light pulse should be as small as possible to avoid imaging streaky particles. For the present PIV system, the light pulse duration is fixed at 9 ns. Thus, imaging streaky particles is not an issue.

Peak locking refers to the bias that occurs when the estimated location of the correlation peak is shifted towards the nearest integer value. According to Fincham and Spedding (1997) peak locking occurs in any type of Image Velocimetry technique where sub-pixel determination of the correlation peak is attempted. However, it can be minimized by using a suitable peak-fitting scheme. Cowen and Monismith (1997) tested several different sub-pixel peak fitting schemes including the three-point Gaussian, parabolic and center-of-mass estimators and found that the three-point Gaussian estimator performed the best. The present PIV algorithm used three point Gaussian estimator for sub-pixel determination of the correlation peak (Marxen 1998).

We used the results of Cowen and Monismith (1997) and Prasad *et al.* (1992) to estimate the errors in the DPIV data. The errors were estimated using the raw displacement data. A detailed step-by-step procedure to estimate errors in the DPIV data of the waterside experiments under unsaturated conditions for the bulk water temperature of 36 °C, is given below.

1. The PIV provides four velocity gradients, $\frac{\partial u}{\partial x}, \frac{\partial u}{\partial z}, \frac{\partial y}{\partial x}$ and $\frac{\partial w}{\partial z}$. The mean values of all four gradients were computed from the raw DPIV data. The largest mean velocity gradient was $\frac{\partial w}{\partial z}$ with the value of 0.215 %. Thus, this gradient was used to estimate the errors in the vertical velocity.
2. The errors due to velocity gradient were estimated using figure 5(e) in Cowen and Monismith (1997). This figure gives the approximate errors due to velocity gradients and is based on a particle size of 2.0 pixels. The total error due to velocity gradients is the sum of the mean and RMS errors. The errors due to velocity gradient were estimated to be,

$$\varepsilon_w = 0.06 \text{ pixels (based on 0.215 \% gradient)} \qquad \text{(A.1)}$$

where ε_w is the errors associated with the vertical velocity.

3. As mentioned earlier, the particle diameter in the present study was 0.3 pixels, therefore, the errors due to smaller particle diameter should be accounted for. We used figure 5 (a) in Cowen and Monismith (1997), which is the plot of the errors as a function of the particle size. The errors due to a particle diameter of 1.0 pixel were estimated, since this was the smallest particle diameter that Cowen and Monismith

(1997) considered. The errors for a particle diameter of 1.0 pixel and the same velocity gradients were,

$$\varepsilon_w = 0.2 \text{ pixels} \tag{A.2}$$

4. The errors corresponding to a particle diameter of 0.3 pixels were estimated using figure 13 in Prasad *et al.* (1992), which shows the variation in the bias (peak locking error) and RMS errors as a function of particle diameter. Using this figure, we estimated that the errors associated with a particle diameter of 0.3 pixels would be 38 % larger than the errors associated with a particle diameter of 1.0 pixel. The estimates of Prasad *et al.* (1992) were based on a center of mass peak-fitting scheme, which is the scheme most susceptible to peak-locking errors (Fincham and Spedding 1997). The errors in the present case would be smaller since we used a three-point Gaussian estimator, which is much less susceptible to peak locking than the center of mass scheme (Cowen and Monismith 1997). Therefore, a more realistic estimate of the increase in the errors is 19 % due to the small particle size. Hence, the final error estimate based on a 19 % increase in errors was,

$$\varepsilon_w = 0.0714 \text{ pixels} \tag{A.3}$$

5. The in-plane vertical displacement based on the mean and standard deviation of the vertical displacement was estimated to be,

$$W = \overline{w} + \sigma_w = 3.8845 \text{ pixels} \approx 203 \text{ μm} \tag{A.4}$$

The out-of-plane motion was expected to be less than or equal to the vertical displacement. Since the thickness of the laser light sheet was approximately 300 μm, the out-of-plane motion in the present case was assumed to be negligible.

6. The error due to AGW interpolation was estimated from figure 5(f) in Cowen and Monismith (1997) and it was 0.08 pixels.

Thus the total error in the vertical velocity was estimated to be,

$$\varepsilon_w = 0.0714 + 0.08 = 0.1514 \text{ pixels} \tag{A.5}$$

This RMS error expressed in velocity units is,

$$\varepsilon_w = 0.012 \text{ cm s}^{-1} \tag{A.6}$$

The mean velocity gradients for the streamwise velocity components were much smaller than that for the vertical velocity. Thus, the errors in the streamwise velocity are expected to be less than the vertical velocity. However, for the conservative estimate, we assumed that the errors in the streamwise velocity (u) to be the same as the errors in the vertical velocity (w) . Therefore, the error in the resultant velocity V, where $V = \sqrt{u^2 + w^2}$ is,

$$\varepsilon_V = 0.0168 \text{ cm s}^{-1} \tag{A.7}$$

Hence, the average RMS error in the velocity estimates is ± 0.0168 cm s^{-1}. The uncertainty in the velocity measurements was calculated by dividing the RMS error with the resultant (V) of the mean velocity components u and w in the measurement region and found to be 6 %. The same procedure was adopted for the close lid (saturated conditions) and airside velocity data and the RMS errors in the velocity estimates was found to be ± 0.0084 cm s^{-1} and ± 0.4205 cm s^{-1} respectively. The uncertainty in the velocity in the close lid data was found to be 9 %, however for airside data it was 8.8 %.

Appendix B

Particle Response Time

The water was seeded with silver-coated glass spheres, with a mean diameter of 15 μm and a specific gravity of 1.6 (Potters Industries, Paoli, Pennsylvania). These seed particles are not neutrally buoyant and therefore, it was necessary to determine how accurately these particles follow the fluid motion. The characteristic response time of the seed particles was computed by,

$$T_P = \frac{u_T}{g} \tag{B.1}$$

where T_P is the particle response time, u_T is the particle terminal velocity and g is the acceleration due to gravity (Snyder and Lumley 1971). The terminal velocity was computed by,

$$u_T = \frac{(s.g.-1)D^2 g}{18\nu} \tag{B.2}$$

where s.g. is specific gravity, D is the diameter of the seed particle and ν is the kinematic viscosity of water (Siegel and Plueddemann 1991). For the present case the terminal velocity was found to be 0.094 mm/sec and the response time was estimated to be 0.01 ms. The Kolmogorov time scale was computed from the energy dissipation using the following equation.

$$\tau = \left(\frac{\nu}{\varepsilon}\right)^{1/2} \tag{B.3}$$

where τ is the Kolmogorov time scale, ε is the rate of energy dissipation and ν is the kinematic viscosity of water (Tennekes and Lumley 1972). The energy dissipation was

estimated from the turbulent velocity gradients for the high heat flux conditions where the Kolmogorov time scale is smallest. The estimated Kolmogorov time scale for high heat flux case under present experimental conditions was approximately 1.2 sec. The particle response time was found to be more than 5 orders of magnitude smaller than the Kolmogorov time scale confirming that the seed particles accurately followed the fluid motion (Snyder and Lumley 1971, Veron and Melville 1999). Same procedure was adopted for the airside analysis. Only high heat flux case was considered in calculating the Kolmogorov time scale which is smallest in magnitude compared to low heat flux and neutral conditions. As mentioned in the text that airside was seeded with oil mist of 0.025 μm diameter. The terminal velocity and response time for oil mist was found to be 1.6712 $\times 10^{-3}$ mm/sec and 1.7 $\times 10^{-4}$ ms respectively. However the estimated Kolmogorov time scale for airside data was approximately 75 ms which is more than two orders of magnitude higher than the particle response time which shows that the seeding particles accurately follow the flow field.

Appendix C

Time Difference between an Image Pair

The air and waterside two-dimensional velocity fields were measured using digital particle image velocimetry (DPIV). The DPIV technique computes the velocity vectors by cross-correlating the interrogation region in the first image with the corresponding search region in the second image of an image pair. ΔT is the time difference between the image pair. A four-channel digital delay generator (555-4C, Berkeley Nucleonics Corporation, San Rafael CA) was used to control the timing of the laser light pulses. Due to the difference in velocity magnitudes, a constant time separation between the two images of an image pair will give different particle shifts for different cases. That is, smaller particle shift for small velocity magnitude. Very small particle shift increases uncertainty in the velocity measurements. Thus, the time separation between the two images of an image pair was varied in each case, in order to obtain reasonable particle shifts. The time difference between an image pair under different experimental conditions for airside and waterside experiments is given in the following table.

Water Temperature (°C)	Waterside (unsaturated conditions)	Waterside (saturated conditions)	Airside
36	66.667 m sec	133.333 m sec	3 m sec
30	66.667 m sec	133.333 m sec	3 m sec
23	133.333 m sec		5 m sec

Table : Time difference between an image pair.